

The spectral and temporal variability of the isolated X-ray pulsar RX J0720.4-3125

Untersuchung der spektralen und zeitlichen Variabilität des isolierten Röntgenpulsars RX J0720.4-3125

A thesis submitted for the degree of
doctor rerum naturalium (Dr. rer. nat.)
2010 September 29th

presented to the council of the Physikalisch-Astronomische Fakultät der
Friedrich-Schiller-Universität Jena

Dipl. Phys. Markus Matthias Hohle

born on November 12th 1982 in Pößneck, Thuringia, Germany

Max-Planck-Institut für extraterrestrische Physik, Garching, Germany
Astrophysikalisches Institut und Universitätssternwarte der
Friedrich-Schiller-Universität, Jena, Germany

1. Reviewer: Prof. Dr. Ralph Neuhäuser
2. Reviewer: Prof. Dr. Joachim Trümper (Co-referent)
3. Reviewer: Prof. Dr. (USA) Fred Walter

Day of the defense: January, 27th 2011

Signature from head of PhD committee:

Abstract

The radio-quiet thermally emitting X-ray pulsar RX J0720.4–3125 belongs to a group of seven isolated neutron stars (often referred to as the “Magnificent Seven”). They share similar properties such as pure thermal radiation (black body emission with broad absorption features in some cases), long pulse periods (3 – 12 s) and high magnetic field strengths ($B \approx 10^{13}$ Gauss) on their surfaces. These neutron stars are nearby (≤ 500 pc) and up to a few million years old (i.e. relatively young and still hot), thus, most of them have been identified with dim (25 – 28 mag) blue optical counterparts.

RX J0720.4–3125 is unique among the “Magnificent Seven” as it shows long term variations in its spectral properties (temperature, size of the emitting area and equivalent width of the broad absorption feature) and irregularities in the pulse period on time scales of years.

The main two theories put forward to explain the behaviour of RX J0720.4–3125 are either free precession or a glitch – a sudden event like a star quake or an impact of a massive object, that released much energy in a short time.

In this work, most recent data from new observations with XMM-Newton and Chandra as well as already existing archival data are analysed (altogether now covering a time span of almost twenty years). While the spectral changes clearly do not follow a sinusoidal variation if the new observations are included, the phase residuals seem to follow a periodic behaviour. An updated phase coherent timing solution was performed and it was shown that for such investigations a restriction to the hard energy band at 400 – 1000 eV is most suitable to achieve best agreement between the phase residuals derived from different X-ray instruments. Based on the new data, different theories to explain the behaviour of RX J0720.4–3125 are modeled, reviewed and discussed, as well as physical consequences of the conclusions are presented.

The model of free precession explains well the timing behaviour of RX J0720.4–3125, but does not sufficiently reproduce the spectral variations. However, since precession explains the variable phase shift between hard (400 – 1000 eV) and soft (120 – 400 eV) photons, it is still favoured; but, now

with a long term period of ≈ 14 yrs (not 7 yrs as previously suspected). The long term precession period would correspond to an ellipticity of $\epsilon \approx 2 \times 10^{-8}$ for the neutron star.

After co-adding all XMM-Newton RGS and Chandra HRC-S/LETG data, three narrow absorption features (among them, two were unknown before) are detected in the spectra of RX J0720.4–3125. These absorption features likely originate from highly ionised and neutral oxygen.

Der radioleise, thermisch strahlende Röntgenpulsar RX J0720.4–3125 gehört zu einer Gruppe von sieben isolierten Neutronensternen (oft als die “Glorreichen Sieben” bezeichnet), welche sehr ähnliche Eigenschaften aufweisen. Dies sind reine thermische Strahlung (Schwarzkörperstrahlung, in einigen Fällen mit Absorptionslinien), lange Pulsperioden (3 – 12 s) und hohe Magnetfelddichten ($B \approx 10^{13}$ Gauss) auf ihren Oberflächen. Diese Neutronensterne sind sehr nah (≤ 500 pc) und höchstens wenige Jahrmillionen alt (also relativ jung und deshalb noch heiß). Daher wurden einige auch als leuchtschwache (25 – 28 mag) blaue optische Quellen identifiziert.

Unter den “Glorreichen Sieben” ist RX J0720.4–3125 einzigartig, da seine spektralen Eigenschaften (Temperatur, Größe der emittierenden Fläche und Tiefe der breiten Absorptionslinie) sowie die Pulsperiode in Zeiträumen von Jahren variieren.

Die beiden hauptsächlich diskutierten Theorien, welche das Verhalten von RX J0720.4–3125 erklären könnten, sind freie Präzession oder ein sogenannter Glitch – ein plötzliches Ereignis, wie z.B. ein Sternbeben oder der Einschlag eines massereichen Objektes, welcher in kurzer Zeit viel Energie freisetzt.

In dieser Arbeit werden jüngste Daten von neuesten Beobachtungen mit XMM-Newton und Chandra zusammen mit schon existierenden Archivdaten (insgesamt eine Zeitspanne von fast zwanzig Jahren) ausgewertet und untersucht. Während die spektralen Veränderungen deutlich keiner sinusförmigen Veränderung mehr folgen, wenn man die neuen Beobachtungen hinzuzieht, scheinen die Phasenresiduen einem periodischen Verhalten zu unterliegen. Eine aktualisierte phasenkohärente Zeitlösung wurde erhalten und zeigte, daß eine Begrenzung auf das harte Energieband (400 – 1000 eV) am geeignetsten ist, um die von verschiedenen Röntgendetektoren erhaltenen Phasenresiduen in Übereinstimmung zu bringen. Von den neuen Daten ausgehend, werden verschiedene Theorien, welche das Verhalten von RX J0720.4–3125 erklären, modelliert und diskutiert, sowie deren Gültigkeit neu bewertet und die daraus fol-

genden physikalischen Konsequenzen erörtert.

Das Modell der freien Präzession kann zwanglos das zeitliche Verhalten von RX J0720.4–3125 erklären, reproduziert jedoch die spektralen Veränderungen nicht zufriedenstellend. Da allerdings freie Präzession die variable Phasenverschiebung zwischen hartem (400 – 1000 eV) und weichem (120 – 400 eV) Band erklären kann, ist sie immer noch favorisiert, aber nun mit einer Langzeitperiode von etwa 14 Jahren (statt sieben Jahren, wie zuvor vermutet). Die Langzeitpräzessionsperiode würde einer Elliptizität des Neutronensterns von $\epsilon \approx 2 \times 10^{-8}$ entsprechen.

Durch das Aufaddieren aller XMM-Newton RGS und der Chandra HRC-S/LETG Daten konnten drei schmale Absorptionslinien (darunter zwei bisher unbekannte) in den Spektren von RX J0720.4–3125 detektiert werden. Diese Absorptionslinien stammen sehr wahrscheinlich von hochionisiertem und neutralem Sauerstoff.

Thesis

- The long term spectral changes (temperature, size of the emitting area and equivalent width of the absorption feature) of the young isolated X-ray pulsar RX J0720.4–3125 do not follow a sinusoidal trend.
- In the X-ray spectra of RX J0720.4–3125, in particular in the Chandra HRC-S/LETG spectra, absorption features were detected. Most likely, the absorption lines are caused by highly ionised oxygen (OVII/OVI or redshifted OVIII at 0.57 keV, redshifted OVII/OVI at 0.48 keV) and neutral oxygen at 0.53 keV (likely caused by the interstellar medium). The presumably redshifted lines yield a gravitational redshift of $g_r = 1.17$.
- The phase residuals derived from the observations performed with different instruments are only comparable if the analysis is restricted to a particular energy band. The best agreement is achieved for the hard energy band of 0.4 – 1.0 keV. This restriction to the hard energy band accounts best for the different sensitivities of the various instruments.
- The updated timing solution for the hard (0.4 – 1.0 keV) and the soft energy (0.12 – 0.4 keV) band lead to large values for the phase residuals if the simple model with constant spin-down is applied.
- The phase residuals are reduced if a glitch event is added to the simple timing solution. However, the glitch solution from previous authors has to be modified.
- The phase residuals also reduce if it is assumed that RX J0720.4–3125 is a free precessing neutron star with a long term period of 14 years. Free precession also explains the variable phase difference between the hard and the soft energy band.

Für meine liebe kleine Leonie.

Acknowledgements

This work has benefited from the support and involvement of many people in various regards, thus I am deeply indebted to them.

Sincere thanks are given to Frank Haberl for suggesting and mentoring this thesis, as well as for the pleasant collaboration in the past three years. I have learned plenty of important things in this time. The introduction in the new subject was simplified since he provided me his software for the XMM-Newton data reduction.

I am much obliged to Ralph Neuhäuser, who significantly supported my scientific career. I like to thank him for his openness and awareness also regarding private requests. The latter also helped me to overcome a hard stroke in my family.

During my visits in Garching I always felt welcomed, thus I would like to thank the X-ray group for the pleasant time.

I like to thank Birgit Boller and Monika Müller for the support to overcome diverse administrative things and I thank Marion Lamprecht for the cheerful accommodation during my stays at the MPE. Thanks to Harald Baumgartner and Jürgen Weiprecht who cared for the computational support at the MPE in Garching and the AIU in Jena, respectively.

In the past four years, since I am at the AIU in Jena, it was a pleasure to work with many colleagues, some even became friends. I would like to thank them for the great time.

During my work on neutron stars I learned a lot from sharing knowledge and ideas with other scientists. In this regard I would like to acknowledge my co-authors Roberto Turolla for many fruitful discussions and ideas, Jacco Vink in particular for his support regarding to my first XMM-Newton proposal, Silvia Zane, Mariano Méndez and Cor de Vries. In this regard my sincere thanks are given to Sergei Popov. I like to thank Theodor Pribulla for fitting the phase residuals with orbital motion caused by a companion with his code and thanks are given to Bettina Posselt for the fruitful collaboration regarding the Spitzer and Hubble proposals.

I would like to thank Thomas Eisenbeiß for the collaboration regarding the V-band magnitude of RX J0720.4–3125 and Valeri Hambaryan for useful references for period detection algorithms.

Thanks are given to the referees for careful reading and reviewing of my thesis.

I would like to thank as well Andreas Bauswein, Roland Diehl, Walburga Frankenhuisen, Hovik Grigorian, Thomas Janka, Oleg Kargaltsev, Ewald Müller, George Pavlov, Armen Sedrakian, Marten van Kerkwijk and Fred Walter.

I also like to thank the Max-Planck society, in particular Günther Hasinger, for the financial support of my work, and the Deutsche Forschungsgesellschaft (DFG) through the Sonderforschungsbereich für Gravitationswellenastronomie SFB/TR-7.

Thanks are given to David Blaschke who invited me to various summer and winter schools, where I got acquainted with many important things and places and who brought me in contact with important people. These schools are financially supported through the Helmholtz society and CompStar via the European Science Foundation (ESF).

I deeply thank my parents Angela and Matthias, my sister Isabel and my great love Nina for their love and support I experienced, in particular during the hardest times I had. Without you, I would not have achieved a lot of things.

Diese Arbeit hat in mehrfacher Hinsicht von der Unterstützung und Mitwirkung vieler Menschen profitiert, denen ich zu Dank verpflichtet bin.

Mein herzlicher Dank gilt Frank Haberl für die Bereitstellung des Themas und die Betreuung meiner Doktorarbeit sowie für die vertrauensvolle Zusammenarbeit in den zurückliegenden drei Jahren. Vieles habe ich in dieser Zeit gelernt. Der Einstieg in das neue Thema wurde mir durch die Bereitstellung seiner Quelltexte zur Verarbeitung der XMM-Newton Daten enorm erleichtert.

Ich möchte mich aufrichtig bei Ralph Neuhäuser bedanken, der meine wissenschaftliche Laufbahn von Beginn an in vielfältiger Weise unterstützt hat. Dazu zähle ich auch seine Offenheit und Sensibilität gegenüber persönlichen Belangen. Letzteres half auch einen schweren familiären Schicksalsschlag zu überstehen.

Bei meinen Besuchen in Garching habe ich mich stets sehr willkommen gefühlt. Daher möchte ich mich für die angenehme Arbeitsatmosphäre bei der Röntgengruppe des MPE in Garching bedanken.

Ich bedanke mich bei Birgit Boller und Monika Müller für die Hilfe bei der Bewältigung mannigfaltiger organisatorischer Dinge und bei Marion Lamprecht für die herzliche Umsorgung während meiner Besuche am MPE. Dank gilt auch Harald Baumgartner und Jürgen Weiprecht für die Betreuung der Rechentechnik am MPE in Garching bzw. am AIU in Jena.

Während meiner vier Jahre am AIU in Jena sind mir viele Kollegen ans Herz gewachsen und einige zu Freunden geworden. Ihnen sei für die schöne Zeit und gute Zusammenarbeit gedankt.

Im Laufe meiner Arbeit über Neutronensterne konnte ich viel von der Bereitschaft Wissen und Ideen zu teilen und auszutauschen lernen. Dabei sei meinen Co-Autoren Roberto Turolla für viele anregende Diskussionen und Ideen, Jacco Vink insbesondere für die Hilfe bei meinem ersten XMM-Newton Antrag, Silvia Zane, Mariano Méndez und Cor de Vries gedankt. In diesem Zusammenhang möchte ich mich auch ganz besonders bei Sergei Popov bedanken. Ich bedanke mich bei Theodor Pribulla für das Fitten der Phasenresiduen mit der Orbitbewegung verursacht durch einen Begleiter mit seinem Programm und Dank gebührt auch Bettina Posselt für die fruchtbare Zusammenarbeit hinsichtlich der Spitzer- und Hubbleanträge. Ich möchte mich bei Thomas Eisenbeiß für die Zusammenarbeit über die V-Band-Magnitude von RX J0720.4–3125 und bei Valeri Hambaryan für wichtige Hinweise bezüglich Algorithmen zur Periodendetektion bedanken.

Allen Gutachtern sei für das sorgfältige Lesen und bewerten meiner Arbeit gedankt.

Des Weiteren möchte ich meine Dankbarkeit gegenüber Andreas Bauswein, Roland Diehl, Walburga Frankenhuisen, Hovik Grigorian, Thomas Janka, Oleg Kargaltsev, Ewald Müller, George Pavlov, Armen Sedrakian, Marten van Kerkwijk und Fred Walter zum Ausdruck bringen.

Mein Dank gilt der Max-Planck-Gesellschaft, hierbei insbesondere Günther Hasinger, für die Finanzierung meiner Arbeit, und der Deutschen Forschungsgesellschaft (DFG) durch den Sonderforschungsbereich für Gravitationswellenastronomie SFB/TR-7.

Ich bedanke mich bei David Blaschke für die Einladungen zu verschiedenen Sommer- und Winterschulen, auf denen ich viel gelernt, gesehen und wichtige Kontakte geknüpft habe. Diese Schulen wurden von der Helmholtz-Gesellschaft und CompStar über die European Science Foundation (ESF) ermöglicht.

Ich bedanke mich von ganzem Herzen bei meinen Eltern Angela und Matthias, meiner Schwester Isabel und meiner großen Liebe Nina für ihre Liebe und Unterstützung, die ich vor allem auch in den schwersten Zeiten erfahren durfte. Ohne euch hätte ich vieles nicht erreichen können.

Contents

List of Figures	xv
List of Tables	xvii
List of Units	xix
1 Introduction	1
1.1 The diversity of neutron stars	1
1.2 Observable properties of neutron stars	3
1.2.1 Ages and magnetic fields	3
1.2.2 Radii and temperatures	4
1.2.3 Composition, structure and their constraints from observations	5
1.3 A brief overview on the “Magnificent Seven”	7
1.4 RX J0720.4–3125	10
1.4.1 Spectral and temporal variations	10
1.4.2 Interpreting the spectral and temporal variations	12
2 Data and data reduction	17
2.1 ROSAT	17
2.2 XMM-Newton	18
2.2.1 EPIC-pn	20
2.2.2 EPIC-MOS1 and EPIC-MOS2	21
2.2.3 RGS1 and RGS2	21
2.2.4 Reduction of XMM-Newton data	22
2.3 Chandra	25
2.3.1 HRC-S/LETG	25
2.3.2 ACIS-CC	26
2.3.3 Reduction of Chandra data	27

3 Pulsar timing	29
3.1 Phase coherent timing	30
3.2 Algorithms for period detections	30
3.2.1 Z_n^2 test	31
3.2.2 Cash statistics and maximum likelihood	31
3.2.3 String length	32
3.3 Why the hard band?	33
4 Results	37
4.1 Spectral properties	37
4.1.1 EPIC-pn	37
4.1.2 EPIC-MOS and RGS	39
4.1.3 Chandra HRC-S/LETG	42
4.2 Timing	46
4.2.1 Individual periods, light curves and phase determination	46
4.2.2 Timing solutions	49
5 Discussion	57
5.1 Updated interpretation of the spectral and temporal variations of RX J0720.4–3125	57
5.1.1 Precession	57
5.1.2 The glitch hypothesis	59
5.1.3 Tkachenko waves	61
5.1.4 Circumstellar and/or fallback disk	63
5.1.5 Orbital motion	65
5.2 Phase resolved spectroscopy	67
6 Modelling a free precessing neutron star	71
6.1 The model	72
6.1.1 The geometry of the problem	72
6.1.2 Physical input	72
6.1.2.1 Light bending and light emission	72
6.1.2.2 Temperature distributions	74
6.1.2.3 Free precession	74
6.1.3 Test of the code and evaluation of different emission geometries	76
6.2 Procedure and fit results	77
6.2.1 Fitting the phase residuals	83
6.2.2 Fitting the temperature variations	85

7 Summary	87
8 Conclusions and outlook	89
References	91
A Time of arrivals (TOAs) of the final timing solution and individual Periods	97
B Publications during PhD	103
B.1 Scientific papers	103
B.2 Accepted proposals for observations listed in the ADS	105
B.3 Conference contributions and proceedings listed in the ADS	105
C Talks	107
C.1 Scientific talks	107
C.2 Public talks	108
D Teaching and supervising	109
E Curriculum vitae	111

List of Figures

1.1	The $P - \dot{P}$ diagram.	2
1.2	Set of different Equations of State in the radius-mass diagram.	8
1.3	The phase shift between the total flux and the hardness ratio of RX J0720.4–3125.	12
1.4	Variation of black body temperature, equivalent width and radius of RX J0720.4–3125.	13
1.5	The XMM-Newton spectra of RX J0720.4–3125 with the lowest and highest measured temperatures.	14
1.6	Phase residuals of RX J0720.4–3125.	15
2.1	EPIC-pn detector	20
2.2	EPIC-MOS detector	21
2.3	The RGS2 spectrum of RX J0720.4–3125.	22
2.4	RGS1 spatial and energy dispersion plot.	23
2.5	Zeroth order of RX J0720.4–3125 from HRC-S/LETG	23
2.6	First orders of RX J0720.4–3125 from HRC-S/LETG	25
2.7	Image of RX J0720.4–3125 from ACIS-CC	26
3.1	Periodogram from the XMM-Newton observation revolution 1454	33
3.2	Stringlength periodogram from the XMM-Newton observation revolution 1454	34
3.3	Phase residuals of the hard band	35
3.4	Phase residuals of the soft band	35
4.1	Long term variations of the EPIC-pn spectra of RX J0720.4–3125.	40
4.2	All XMM-Newton EPIC-pn spectra of RX J0720.4–3125.	41
4.3	The co-added RGS1 spectrum of RX J0720.4–3125.	42
4.4	The temperature evolution of RX J0720.4–3125 including the most recent XMM-Newton and Chandra observations.	44
4.5	The Chandra HRC-S/LETG spectra of RX J0720.4–3125.	45
4.6	The co-added HRC-S/LETG spectrum of RX J0720.4–3125	46

LIST OF FIGURES

4.7	The fit residuals from the co-added HRC-S/LETG spectra.	47
4.8	Individual periods from observations with more than 10^4 photons (hard band).	50
4.9	Evolution of \dot{f} , period and phase residuals during the iterative process approaching the final timing solution.	51
4.10	Phase binned light curve of the XMM-Newton EPIC-pn observation revolution 1086.	52
4.11	Fourier coefficients from the light curves of the 16 XMM-Newton EPIC-pn observations of RX J0720.4–3125.	53
4.12	The Z_1^2 values in the $P - \dot{f}$ plane.	54
4.13	Phase residuals of RX J0720.4–3125 after applying the timing solution.	54
5.1	Phase residuals of RX J0720.4–3125 after applying the timing solution shown with sine and abs(sine) fits.	60
5.2	The string lengths derived from the phase residuals of RX J0720.4–3125.	61
5.3	The phase residuals of RX J0720.4–3125 after applying the glitch solution.	62
5.4	SED of RX J0720.4–3125.	64
5.5	Orbital fit of the phase residuals of RX J0720.4–3125	66
5.6	Phase resolved evolution of temperature and equivalent width of RX J0720.4–3125.	68
6.1	The geometry of a rotating sphere.	73
6.2	The different temperature distributions used in this work.	75
6.3	Free precession.	76
6.4	Synthetic light curves of a rotating sphere with two antipodal hot spots (I).	78
6.5	Synthetic light curves of a rotating sphere with two antipodal hot spots (II).	79
6.6	Synthetic light curves of a rotating sphere with two antipodal hot spots (III).	80
6.7	The pulsed fraction depending on the inclination and θ	81
6.8	Relative number of possible geometric configurations of RX J0720.4–3125.	82
6.9	Fitted phase residuals.	83
6.10	Fitted temperature variation	84
6.11	Fitted temperature variation and phase residuals	86

List of Tables

1.1	The inner structure of a neutron star.	7
1.2	Properties of the “Magnificent Seven”	11
2.1	ROSAT observations of RX J0720.4–3125.	18
2.2	XMM-Newton observations of RX J0720.4–3125.	19
2.3	Chandra observations of RX J0720.4–3125.	27
4.1	Fit model for RX J0720.4–3125.	39
4.2	Spectral changes of the phase averaged EPIC-pn spectra of RX J0720.4–3125.	39
4.3	The three narrow absorption features of RX J0720.4–3125 detected with Chandra HRC-S/LETG	46
4.4	Period and \dot{f} derived from different methods in this work, compared to previous results.	50
5.1	Fit results from fitting the phase residuals with a sine or abs(sine).	59
5.2	Orbital elements after fitting the phase residuals of RX J0720.4–3125.	65
A.1	All observations of RX J0720.4–3125 with TOAs and individual periods listed in chronological order.	98

List of Units

Since it is more practical in astrophysics to use SI units scaled to astronomical values and it is more common to use cgs units, a list of the scaled and cgs units that are used in this work, expressed in the kgs system is given here (values given with their 1σ errors).

- 1 AU (astronomical unit; scaled to the average distance between Sun and Earth)
 $1 \text{ AU} = 1.49597870700(3) \times 10^{11} \text{ m}$
- 1 pc (parsec; the distance that is required for an object to have a parallax angle of one arc second with respect to 1 AU)
 $1 \text{ pc} = 3.085678 \times 10^{16} \text{ m} \approx 2.062648 \times 10^5 \text{ AU}$
- $1 M_{\odot}$ (Solar rest mass)
 $1 M_{\odot} = 1.98892(25) \times 10^{30} \text{ kg}$
- $1 M_{\text{J}}$ (Jovian rest mass)
 $1 M_{\text{J}} = 1.8986(25) \times 10^{27} \text{ kg} \approx 1/1047 M_{\odot}$
- 1 eV (electronvolt; amount of kinetic energy gained by a free electron in an electric field having 1 volt)
 $1 \text{ eV} = 1.60217653(14) \times 10^{-19} \text{ J}$
- $1 \text{ erg} = 1 \text{ g cm}^2/\text{s}^2 = 10^{-7} \text{ J} = 10^{-7} \text{ kg m}^2/\text{s}^2$
- $1 \text{ Gauss} = 1 \text{ V s}/\text{cm}^2 = 10^{-4} \text{ T} = 10^{-4} \text{ V s}/\text{m}^2$
- MJD (modified Julian date) counts the days from November 17th 1858, 0:00 a.m.

Note, the gravitational redshift g_r in this work follows the definition

$$g_r = \frac{1}{\sqrt{1 - \left(\frac{2GM}{c^2 r}\right)}}. \quad (1)$$

Often the gravitational redshift is given as

$$g_r = \frac{1}{\sqrt{1 - \left(\frac{2GM}{c^2 r}\right)}} - 1 \quad (2)$$

in the literature as well.

1

Introduction

1.1 The diversity of neutron stars

Since the report of the first neutron star discovered by Jocelyn Bell [46] in 1968, almost 2000 more neutron stars were found up to now. A further mile stone was the discovery of the first binary pulsar [53] due to pulsar timing by Joseph Hooton Taylor Jr. and Russell Hulse in 1974. This extremely rare configuration (nowadays only nine binary pulsars are known, see [118]) enables us to probe general relativity and was a first indirect proof for the existence of gravitational waves. The accordance between the predicted and the observed behaviour of the orbital elements is a stunning confirmation of Einstein's theory (see [119] for a review). Moreover, for the first time neutron star masses could be measured directly. Most masses of the known binary pulsars are close to the canonical value of $1.4 M_{\odot}$ [118] and measured with an accuracy better than 1% in some cases. Later, the same technique helped to detect the first objects with planetary masses orbiting an object with stellar masses outside the Solar system by Aleksander Wolszczan and Dale Frail in 1992 – the so-called pulsar planets around PSR 1257+12 [140].

All these neutron stars are radio pulsars that build by far the largest class of neutron stars. Most radio pulsars have dipole magnetic field strengths of $B \approx 10^{12}$ Gauss and spin periods P in the order of a second. The ages range from a few thousand years up to some hundred million years (Myrs). With some simplifications a neutron star can be seen as a rotating dipole, thus radiating energy and slowly spinning down (see next section). This can be measured by the time derivative of the period, \dot{P} . If radio pulsars are represented in the $P - \dot{P}$ diagram, they roughly occupy the same region, see figure 1.1.

In the bottom left corner of the $P - \dot{P}$ diagram one can identify another population, the millisecond pulsars. Most millisecond pulsars are components of binary systems. They gained momentum due to mass accretion from their stellar companion and thus spun up in the past. With time, neutron stars cool down and/or the radio signal gets weaker, hence,

1. INTRODUCTION

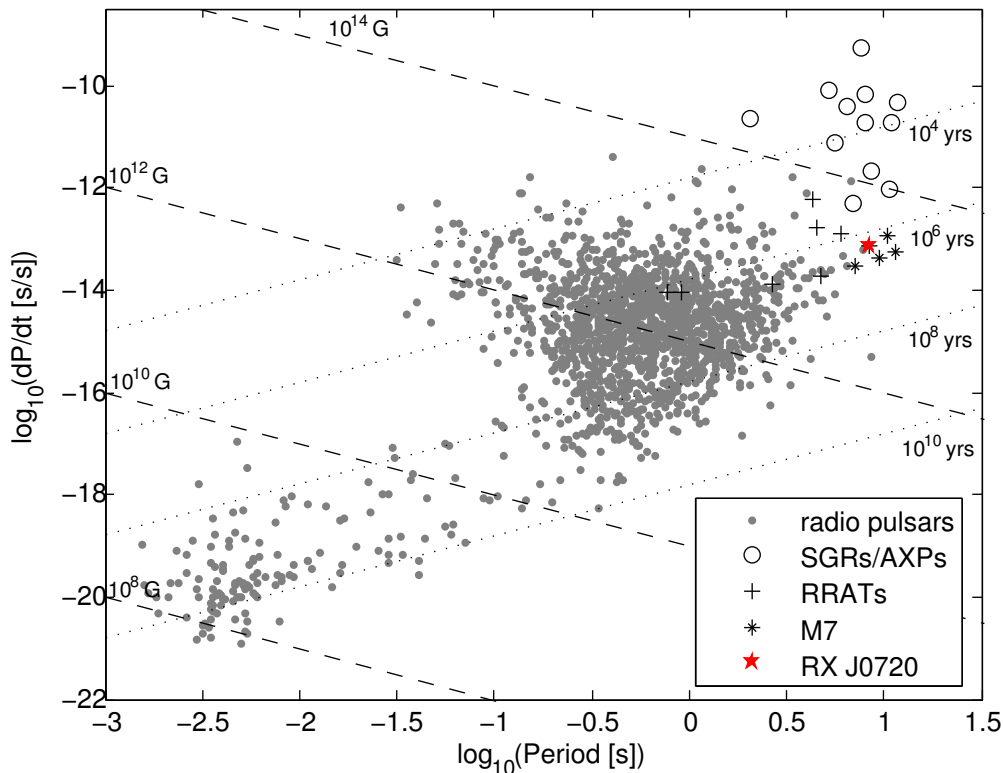


Figure 1.1: The $P-\dot{P}$ diagram of all neutron stars for which these quantities are known with lines of constant characteristic age (dotted, derived from equation 1.6) and constant dipole magnetic field strength (dashed, derived from equation 1.4). The data for the “Magnificent Seven” (M7) are taken from [38; 65; 66; 67; 127], all other data are taken from the ATNF database [85]¹. RX J0720.4–3125 (RX J0720) is marked as a red star.

they become invisible but later can be observed due to their accretion. These objects are called “recycled pulsars”. Although the accreting millisecond pulsars also emit in other wavelengths than radio, they will also be named radio pulsars in this work.

The launch of X-ray and γ -ray telescopes in the last decades opened a new window to neutron star science and allowed to discover new classes (see [102] and references therein for a review).

One of these new classes are the soft gamma repeaters (SGR). They have spin periods of a few seconds and are considered to be young objects (some of them are associated with supernova remnants) and burst in γ -rays. Some SGRs show quasi periodic oscillations during giant (luminosity $\geq 10^{43}$ erg/s) flares with frequencies of about tens of Hertz (Hz). Very similar to the SGRs are the anomalous X-ray pulsars (AXPs) since SGRs in quiescence have the same properties. AXPs have spin periods of a few seconds and several show a hard tail (10 – 150 keV) in their spectra. Probably, SGRs and AXPs are different stages or manifestations of the same class of objects. Both have magnetic fields of $\approx 10^{14}$ Gauss and the X-ray luminosity is several orders of magnitudes larger than the energy loss from the

¹<http://www.atnf.csiro.au/research/pulsar/psrcat/>; from May 1st, 2010

spin-down, and likely originates from the magnetic field decay whence the term magnetars. Rotating radio transients (RRATs) are neutron stars that emit short bursts in the radio band. That makes it challenging to measure their P and \dot{P} . Since the RRATs roughly occupy the same region as the radio quiet “Magnificent Seven” (hereafter M7) in the $P - \dot{P}$ diagram, a connection of both is discussed within the community. The M7 will be widely discussed in section 1.3. Note that AXPs/SGRs, RRATs and the M7 are much different to the *ordinary* radio pulsars since they are highly magnetised and most of them are known to emit in optical, X-ray and γ -rays.

1.2 Observable properties of neutron stars

1.2.1 Ages and magnetic fields

Assuming that the main energy loss of a pulsar is caused by the radiation from a rotating dipole field, as proposed by [95], the loss of rotational energy

$$\frac{dE_{rot}}{dt} = I\omega\dot{\omega} \quad (1.1)$$

equals that of a rotating dipole

$$\frac{dE_B}{dt} = -\frac{B_{dip}^2 R^6 \omega^4 \sin^2 \alpha}{6c^2}, \quad (1.2)$$

where ω is the spin frequency, B_{dip} the magnetic field strength at the magnetic pole, R the radius of the neutron star, I its moment of inertia, α the angle between rotation axis and magnetic pole axis and c is the speed of light in vacuum.

Setting equation 1.1 equal to equation 1.2 leads to an equation with the general form

$$\dot{\omega} = const \times \omega^n \quad (1.3)$$

where n is the braking index with $n = 3$ in the case of a dipole.

From equation 1.1 and equation 1.2 an expression for B_{dip} can be derived using typical values of $R = 10$ km and $M = 1.4 M_{\odot}$,

$$B_{dip} \approx 3.2 \times 10^{19} \sqrt{P\dot{P}} \text{ Gauss.} \quad (1.4)$$

Charged particles may give rise to spectral features related to cyclotron absorption. Gravitational redshifted cyclotron lines could be measured at the energy

$$E_p = \frac{\hbar e B}{m_p c} \frac{1}{\sqrt{1 - r_s/R}} \quad (1.5)$$

1. INTRODUCTION

where m_p is the mass of the particle, e is the particle charge (equals the elementary charge for protons, electrons and positrons), \hbar is the reduced Planck's constant and r_s is the Schwarzschild radius. Equation 1.5 delivers an alternative estimate to equation 1.4 for the magnetic field strength.

Since the neutron star spins down and assuming that the initial spin frequency is much larger than the present one, the characteristic age is given by

$$\tau = \frac{1}{n-1} \frac{P}{\dot{P}} \quad (1.6)$$

derived from integrating equation 1.3. Equation 1.6 and equation 1.4 are used for the lines of constant ages and constant magnetic fields in figure 1.1.

However, if the neutron star is not spherical, but has a non-axisymmetric shape with the ellipticity ϵ^1 , the loss of momentum due to gravitational radiation from the gravitational quadrupole term (assuming a homogeneous density) is

$$\frac{dE_{GW}}{dt} = \frac{32G}{5c^5} I^2 \epsilon^2 \omega^6 \quad (1.7)$$

where G is the gravitational constant, and ϵ might have values of 10^{-9} to 10^{-6} [97]. With the contribution from equation 1.7, the braking index could be up to $n = 7$ [139]. In reality the braking index is influenced by a combination of dipole and gravitational radiation. The measured values of the braking index from five different pulsars show that n varies at least within a factor of two [81], but lies below $n = 3$, indicating the absence of gravitational radiation. Braking indices below $n = 3$ are e.g. explained by pulsar winds [141; 143]. Glitches change P and \dot{P} and mimic a different age, the magnetic field is not a perfect dipole and possible motion of the poles with respect to the surface of the neutron star influences n significantly [82]. Since the magnetic field is supposed to be much stronger at birth of the neutron star (at least for magnetars), thermal properties of the crust and the structure of the magnetic field are changing and influence each other. This leads to a significant evolution of the braking index n from $n = 2$ to $n = 4$ for neutron stars younger than 0.1 Myrs, up to $n = 10$ for a 1 Myr old neutron star, see [100], figure 10 therein. In addition there might be some other mechanisms influencing n and τ . Therefore τ gives an upper limit while tracing back young and hot neutron stars to their assumed birth sites gives kinematic ages below τ [121; 122] that might be more reliable.

1.2.2 Radii and temperatures

Measured neutron star masses from binary pulsars vary from $M = 1.1 M_\odot$ to $M = 1.4 M_\odot$ [118], while theoretical predictions give a maximum mass of $M = 2.7 M_\odot$ [117] for extreme

¹ $\epsilon = (I_1 - I_2)/I_3$

Equations of State (hereafter EoSs). The expected radii are in the range from $R = 8$ km to $R = 12$ km [75]. In any case, neutron stars are relativistic objects and the radii seen from a distant observer (R_∞) differ from the intrinsic neutron star radii following

$$R_\infty = \frac{R}{\sqrt{1 - r_s/R}}, \quad (1.8)$$

hence neutron stars appear larger. Due to the gravitational redshift neutron stars also appear cooler at infinity, i.e. the temperature seen by a distant observer is

$$T_\infty = T \times \sqrt{1 - r_s/R}. \quad (1.9)$$

Thus, for a black body the measured luminosity is given by

$$L_\infty = L \times (1 - r_s/R) = 4\pi\sigma R_\infty^2 T_\infty^4, \quad (1.10)$$

where σ is the Stefan-Boltzmann constant.

1.2.3 Composition, structure and their constraints from observations

As the name suggests, a first approximation to describe neutron stars is a composition of pure neutrons. The EoS of a fully degenerated pure ideal neutron gas was used in [94] and simple assumptions already deliver the right magnitudes for masses and radii. However, with increasing density the interactions between the particles have to be taken into account and the neutrons become superfluid. For even higher densities neutrons and protons may turn into a pion condensate or other stages of matter, such as deconfined quarks. Thus, neutron stars have to be treated as highly non-homogeneous objects having a shell structure – each shell with its own special properties. Since this is an own part of micro/particle physics, only a brief overview of the issues important for observations is given here.

The general picture [117] is that a neutron star is covered with a few centimeter thin but optically thick hydrogen atmosphere on the surface (density $\rho \leq 10^6$ g/cm³). The atmosphere is left over from the supernova event and/or gathered from accretion and may also contain ionised oxygen and iron [87]. This atmosphere should be identified due to dominant absorption lines in the spectra, even for highly magnetised neutron stars [87]. The physical properties of the surface are affected by the temperature and the magnetic field.

The outer crust ($\rho \leq 4.3 \times 10^{11}$ g/cm³) below the atmosphere consists of heavy nuclei with a large neutron fraction and a relativistic degenerated electron gas, like for white dwarfs. In the inner crust the neutrons turn into a superfluid gas ($\rho \leq 2 \times 10^{14}$ g/cm³) that becomes a

1. INTRODUCTION

superfluid neutron liquid mixed with superfluid protons above $\rho = 2.5 \times 10^{14} \text{ g/cm}^3$. When a neutron star is formed, it cools down via neutrino emission and becomes isothermal after $\approx 10^2 \text{ yrs}$ before emerging the following neutrino cooling stage ($\approx 10^2 \text{ yrs}$ to 10^5 yrs) and starts to cool via photon emission after a few 10^5 yrs . Since superfluidity has a significant influence on the heat capacity and neutrino emission (that themselves influence cooling), the critical temperature (that is only roughly known) to switch to superfluidity, depending on the density, could be constrained from observations by measuring the current neutron star temperature and determining its age if the neutron star is young (i.e. hot) enough and thermally emitting [37].

Up to nuclear density ($\rho_{nuc} \approx 2.8 \times 10^{14} \text{ g/cm}^3$) the physics of nucleon-nucleon interaction is well understood and nucleon-nucleon scattering is constrained. However, beyond densities around $\rho \approx 10^{15} \text{ g/cm}^3$ it is not clear what happens: the neutrons may form strange matter (hyperons, kaons or free quarks), or pion condensates or even pure quark matter. If the entire star consists of quark matter, it is called a bare quark star (sometimes “quark star” and “strange star” are used synonymously, although hyperons and kaons bear strangeness, too). If only the core consists of quarks but the crust of ordinary matter (neutrons mixed with protons), it is called a hybrid star. Quark stars are currently hypothetical, but in principle they could be distinguished from neutron stars [7; 8].

Finally, the EoS gives a configuration of the compactness, i.e the ratio of radius and mass (R/M), for which the neutron star is stable. Often the function of compactness R/M itself is called EoS in the literature, since this is the basic observable. Selfbound quark stars have fundamental different trajectories of the EoS (i.e. R/M) compared to *ordinary* neutron stars because they do not need gravitational pressure to stay stable.

Generally, if the change of pressure strongly influences the density, the EoS is called soft, if the change of pressure does not affect the density much, the EoS is called stiff, i.e. stiff EoSs lead to stars with larger radii and maximum masses. A possible structure of a neutron star for a stiff and a soft EoS is listed in table 1.1.

A small set of EoSs is shown in figure 1.2, note the difference between neutron stars and quark stars. In principle, the number of valid EoSs could be constrained by measuring the radius (e.g. from cooling neutron stars using equation 1.10) and mass (from the redshift of spectral lines) for a single neutron star independently. However, only rough estimates for limits (dashed lines and the light green region in figure 1.2 and discussion in [76]) are available and for binary pulsars only masses (no radii) are measured.

1.3 A brief overview on the “Magnificent Seven”

Table 1.1: The inner structure of a neutron star [117] for a soft and a stiff EoS. The boundaries of the different layers are measured with respect to the surface and the densities on the boundaries are given. Both neutron stars have a mass of $M = 1.4 M_{\odot}$. The composition and structure for the soft and stiff EoS is derived from the “Reid” and “TNI” EoS, respectively. For details of the EoSs, see [117], section 9.3. therein.

soft EoS	stiff EoS
atmosphere (?)	atmosphere (?)
outer crust 0 – 0.8 km $\rho \leq 2 \times 10^{14} \text{ g/cm}^3$ heavy nuclei, electrons	outer crust 0 – 0.3 km $\rho \leq 4.3 \times 10^{11} \text{ g/cm}^3$ heavy nuclei, electrons
inner crust 0.8 – 1.8 km $\rho = 2 \times 10^{14} - 5.6 \times 10^{14} \text{ g/cm}^3$ superfluid neutrons & protons, electrons	inner crust 0.3 – 0.9 km $\rho = 4.3 \times 10^{11} - 2 \times 10^{14} \text{ g/cm}^3$ heavy nuclei, electrons, superfluid neutrons
	outer core 0.9– ~ 10 km $\rho \geq 2 \times 10^{14} \text{ g/cm}^3$ superfluid neutrons & protons, electrons
core 1.8 – 9.8 km $\rho = 5.6 \times 10^{14} - 1.93 \times 10^{15} \text{ g/cm}^3$ pion condensate?, solid?, quark matter?	core ~ 10– ~ 12 km $\rho = 1.28 \times 10^{15} \text{ g/cm}^3$ pion condensate?, solid?, quark matter?

1.3 A brief overview on the “Magnificent Seven”

The first identified and brightest member of the M7, RX J1856.4–3754, was discovered by [135] in ROSAT data. After the identification of an optical counterpart [134] and the direct measurement of the trigonometrical parallax [133], it was quite clear that RX J1856.4–3754 is a neutron star. Since then, six further such objects were discovered in ROSAT data soon, but the number of these objects remained constant since 2001 [147]. Only two further candidates [99; 113]¹ were published by now. However, several dozens of such objects should be still hidden in ROSAT data, as predicted by population synthesis studies [104]. Often the M7 are called XDINS, i.e. **X**-ray **d**im **i**solated **n**eutron **s**tars although they are actually bright in X-ray because of their proximity. Some of the M7 spectra show one or two broad absorption features. These features are supposed to be cyclotron resonances from charged particles (protons, electrons), thus it is possible to infer the magnetic field strength both, from equation 1.5 and equation 1.4 since P and \dot{P} is known for most M7. Indeed, magnetic field strengths with values $\approx 10^{13}$ Gauss from the different methods are in good agreement (regarding the simplicity of the assumptions as discussed in the previous section) for the individual sources, if the absorption features are caused by proton cyclotron

¹Recently, the object called “Calvera” [113] was confirmed to be an isolated neutron star, but it is most likely a recycled pulsar with a period of 0.059 s [152].

1. INTRODUCTION

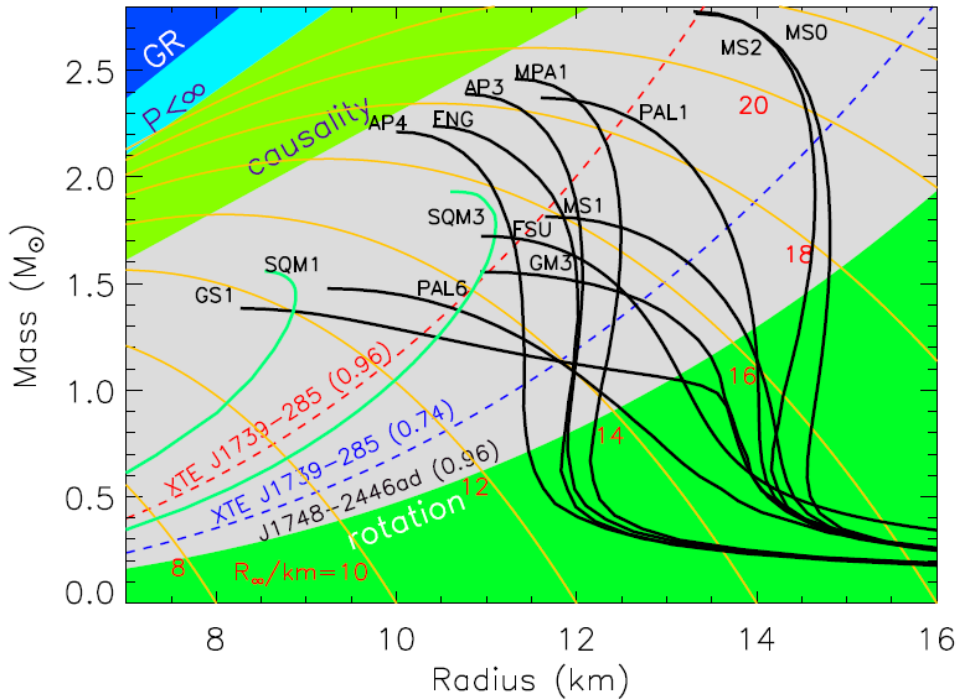


Figure 1.2: Stable mass-radius trajectories from different EoSs (black lines, green lines for selfbound quark stars). The figure is obtained from [76], figure 2 therein. For the notation and details of the EoSs see [76]. The orange lines give R_∞ according to equation 1.8. The upper left regions are not permitted from the radius being smaller than r_s (GR), central pressure is always finite ($P \leq \infty$) and by causality.

resonances. However, the origin of these features is actually unclear.

The M7 are either radio quiet or radio emission detections are ambiguous or could not be confirmed [56; 71; 83; 84]. However, the M7 exhibit X-ray pulsations between 3 s and 12 s. Such long spin periods lead to narrow radio beams, decreasing the probability to observe a radio pulse. All M7 are isolated, i.e. they are not associated with a supernova remnant, do not belong to a binary system and no companions are found so far [105]. From the characteristic age (equation 1.6), the kinematic age [122] and from cooling curves [36; 37] ages of a few Myrs or even less are derived. In most cases, the M7 were identified with faint blue optical counterparts. Intriguingly, all of them (if measured) exhibit an optical excess, their optical flux exceeds by a factor of ten to thirty (RX J2143.0+0654) the extrapolation at low energies of the best-fitting X-ray black body, suggesting that the optical emission originates from a larger, cooler area, while the X-rays originate from a smaller, hotter part of the surface. For RX J1856.4–3754 and RX J0720.4–3125 a trigonometric parallax could be measured, for the other M7 distance estimates are derived from brightness and/or absorption due to the interstellar medium (ISM) [107]. All M7 are closeby, i.e. located within 500 pc (according to [89], the maximum distance of RX J1308.6+2127 could be up to 700 pc, however a more recent and more reliable estimate [122] yields a distance within

500 pc).

The X-ray spectra fit best with pure thermal (i.e. black body) radiation. If a neutron star accretes matter from the ISM, it can be re-heated. Accretion requires relatively dense phases of the ISM [11] (that can be excluded from the low absorption values N_H , see section 4.1, derived from the X-ray spectra), low spatial velocities (that are too high for those M7, RX J1856.4–3754 and RX J0720.4–3125, with measured proper motions and parallaxes [68; 69; 70; 91; 122; 133]) and/or long rotation periods (that are still too short for accretion [136] even in the case of the M7 although their spin periods are large compared to those from other neutron stars, see figure 1.1). Thus, the M7 are likely cooling neutron stars rather than re-heated due to accretion from the ISM.

The basic observable properties of all M7 are listed in table 1.2.

If the M7 are indeed thermally emitting, i.e. are cooling neutron stars, they offer us the opportunity to study matter at extreme conditions (density at nuclear density, $B \approx 10^{13}$ Gauss and temperatures around 10^6 K) directly. Since we can look onto their surface, spectral lines would enable us to measure the gravitational redshift to determine the compactness of the object. From known distance, luminosity and measured temperature the radius can be obtained using equation 1.10, if the emission is that of a black body. Never before, radius and mass (i.e. compactness) of a single neutron star could be measured at once.¹ An estimate for the compactness would give constraints for the various number of EoSs. Having age and temperature, constraints for cooling models could be derived, such as inputs from micro physics and quantum mechanics (cooling due to neutrino emission, cross-sections, neutron and proton superfluidity effects, composition etc.).

How important the astrophysical input from the investigations of the M7 is can be seen from the history of its brightest member, RX J1856.4–3754. After its discovery, the first measured distance of RX J1856.4–3754 was published to be 61_{-8}^{+9} pc [131], inferring a radius of $R_\infty = 3.3$ km. This radius is too small and incompatible with any known EoS, even for those using exotic quark matter. Later, having new observations, the distance measurement was revised to be twice this value [133], but still the X-ray spectra fit with $R_\infty = 5.2$ km normalised to a 140 ± 40 pc distance [16]. This, and the absence of pulsations [26; 111] led to the assumption that RX J1856.4–3754 is a self bound quark star, rather than a neutron star [26; 126; 142]. However, it is argued that the X-ray spectra systematically underestimate the radius [133] and the real value would be $R_\infty = 11$ km. A few years later, the distance of RX J1856.4–3754 was revised again to be 178_{-17}^{+22} pc [89]. Then, following the argumentation in [133], the radius would be too large even to fit the stiffest hadronic (ordinary neutrons and protons) EoS. Nowadays, the distance is again estimated to be 123_{-15}^{+11} pc [132]. In this case, the X-ray flux may originate from a hot polar

¹For the low-mass X-ray binary EXO 0748–676 the gravitational redshift $g_r = 1.35$ was measured from iron and oxygen lines [18], but could not be confirmed.

1. INTRODUCTION

cap, i.e. a limited part of the surface with $R_\infty = 4.4$ km (note, the emitting area is not necessarily of a circular shape) and the optical excess is caused by the cooler surface parts with $R_\infty = 17$ km [15]. This is supported by the detection of weak pulsations (pulsed fraction $\approx 1\%$) in the X-rays [127]. The M7 are one of the rare classes of neutron stars that are currently useful to put constraints on the EoS as discussed here.

Surprisingly, the X-ray spectra of RX J1856.4–3754 are free of any spectral features [15; 16], although it was expected to find strong absorption lines above 0.5 keV due to highly ionised iron or oxygen (see the detailed discussion in [16]). Moreover, also the other M7 do not exhibit formally expected absorption features (except the cyclotron lines) from their hypothetical atmosphere. Thus, the modeling and understanding of the M7 spectra is still challenging [87].

1.4 RX J0720.4–3125

1.4.1 Spectral and temporal variations

The neutron star RX J0720.4–3125 was discovered by [39] as X-ray source, having a 8.391 s pulse period and was identified with a faint blue optical star in [28; 70; 74; 88]. The distance was determined to be 360_{-90}^{+170} pc [69] from direct parallax measurements using Hubble observations.

Among the M7, RX J0720.4–3125 has a unique place inasmuch it shows significant variations in its surface temperature, in the equivalent width of an absorption feature seen in the X-ray spectrum and in the size of the emitting area [22; 38; 51] over time scales of years. Such variations are unknown for the other M7.

RX J0720.4–3125 exhibits a hardness ratio variation and a phase shift between the flux and the hardness ratio (both folded with the 8.391 s pulse period) discovered by [20] in XMM-Newton data, see figure 1.3. Later on, it was shown [22] that the energy-dependent change in the pulse profile is accompanied by a long term change of the X-ray spectrum. The dependence of the pulse profiles on the energy was confirmed by [43] and a phase lag between soft (0.12 – 0.4 keV) and hard (0.4 – 1.0 keV) photons was also reported. A long term period of $P_{pre} \approx 7.5$ yrs [41] was found in the spectral variations (see figure 1.4 and figure 1.5).

The constant spin-down \dot{P} of RX J0720.4–3125 was first estimated to be $\approx 10^{-14}$ s/s by [151] and a more recent timing solution using further observations was presented in [19]. The phase coherent timing solutions in [63] and [129] have been computed including either data from ROSAT, Chandra and XMM-Newton (the so called “all data” solution), or also Chandra data only and all data except ROSAT, see [129]. Applying a timing solution with

Table 1.2: Properties of the “Magnificent Seven”. B_{cyc} is calculated using equation 1.5 and B_{dip} from equation 1.4. The characteristic age τ is calculated using equation 1.6. Note that τ is larger than the kinematic age t_{kin} , when available.

Object	kT [eV]	P [s]	\dot{P} [10^{-13} s/s]	distance [pc]	B_{cyc} [10^{13} G]	B_{dip} [10^{13} G]	τ [Myrs]	t_{kin} [Myrs]	optical [mag]	proper motion [mas/yr]
RX J0420.0–5022	44	3.45	≤ 92	325 – 345	6.6	≤ 18	≥ 2.2	-	$B = 27.5$	-
RX J0720.4–3125	85 – 95	8.39	0.698	360^{+170}_{-90}	5.6	2.4	1.9	0.4 – 0.5	$V = 26.8$	105
RX J0806.4–4123	92	11.37	0.55	240^{+10}_{-5}	8.6/6.1	2.5	3.3	-	$B \geq 24.0$	-
RX J1308.6+2127 ^a	102	10.31	1.120	76 – 700	6.0/4.6	3.4	1.5	0.5 – 1.0	$m_{50ccd} = 26.8$	223
RX J1605.3+3249	93	6.88?	-	325 – 390	≈ 9	-	-	0.5	$B = 27.2$	155
RX J1856.4–3754	63	7.06	0.3	123^{+11}_{-15}	-	1.5	3.7	0.3	$B = 25.2$	333
RX J2143.0+0654 ^b	102	9.43	0.41	390 – 430	15	2.0	3.7	-	$B = 27.4$	-

ref. for RX J0420.0–5022: [40; 86; 107]

ref. for RX J0720.4–3125: [28; 39; 41; 43; 51; 63; 69; 122; 129]

ref. for RX J0806.4–4123: [40; 42; 65; 107]

ref. for RX J1308.6+2127: [61; 64; 89; 115; 116; 122]

ref. for RX J1605.3+3249: [62; 90; 107; 122; 128; 150]

ref. for RX J1856.4–3754: [15; 68; 122; 127; 132; 133; 134]

ref. for RX J2143.0+0654: [67; 107; 147; 149; 153]

^aRBS 1223

^bRBS 1774

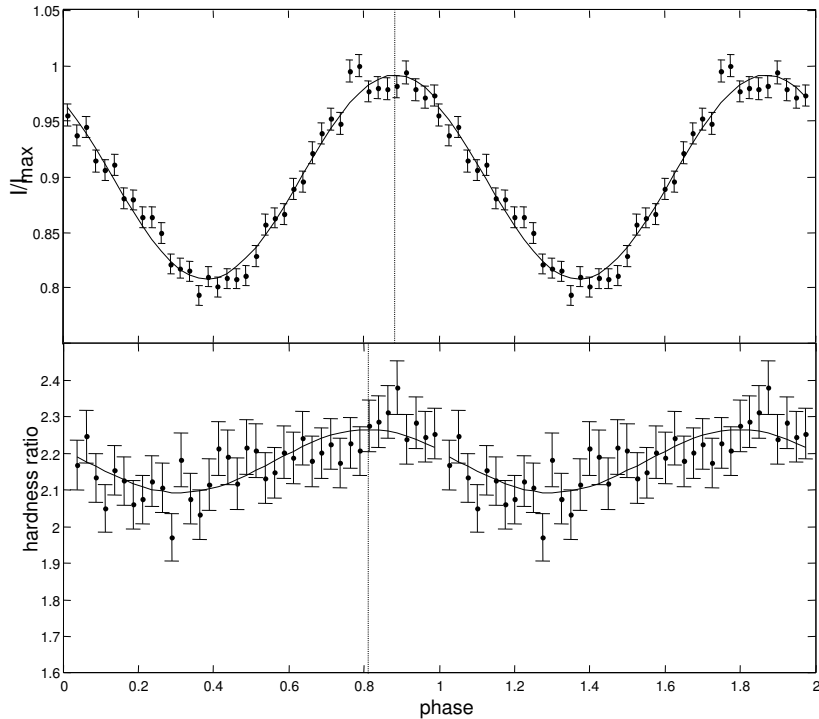


Figure 1.3: The phase shift between the total flux (0.12 – 1.2 keV, upper panel) and the hardness ratio ($HR = \text{Counts}_{0.12-0.4 \text{ keV}} / \text{Counts}_{0.4-0.8 \text{ keV}}$) reported in [20] (see figure 1 therein) using the XMM-Newton observation 0078. The phase of the maximum is shown by the vertical line in both panels, indicating the phase shift. All errors are Poissonian.

constant spin-down does not only lead to variable phase lags between soft and hard photons in the XMM-Newton EPIC-pn data, also the phase residuals including all observations of RX J0720.4–3125 available at this time (until MJD=53700 days, i.e. November 12th, 2005) show a long term variation, probably following a sine, like in the spectral changes (figure 1.4) with a similar longterm period $P_{pre} = 7.88 \pm 0.01$ yrs, shown in figure 1.6, and [38].

1.4.2 Interpreting the spectral and temporal variations

The significant variations of RX J0720.4–3125 merits more investigations and two main possible explanations were proposed: RX J0720.4–3125 is a free precessing neutron star [22; 38; 41; 43], or the behaviour of RX J0720.4–3125 could be explained by a glitch event [129].

Supposing that the X-rays originate from hot polar caps on RX J0720.4–3125 that cover only a fraction of the much cooler (thus invisible in X-rays) entire surface, precession would cause an advanced (the neutron star precesses towards the observer) and a retarded (the neutron star precesses backwards with respect to the observer) signal, whereas the residuals would follow a sine [92]. The residuals are just the additional time needed for a spot to

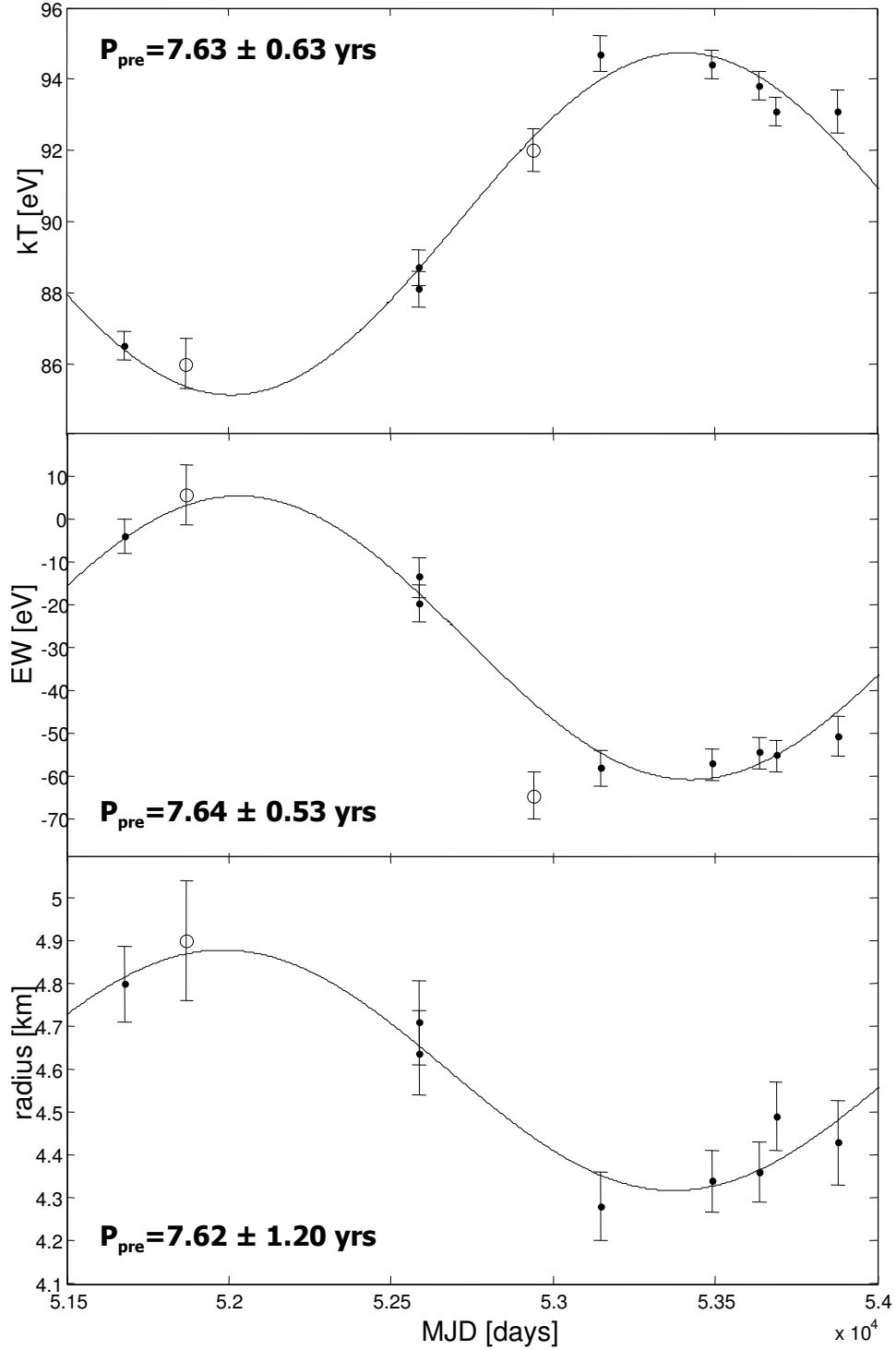


Figure 1.4: Variation of black body temperature (kT), equivalent width (EW) and corresponding radius of the size of the emitting area of RX J0720.4–3125 as reported in [43]. The data obtained from XMM-Newton EPIC-pn observations in full frame mode and thin filter (see explanation in section 2.2) are marked as dots and are used for the error weighted sine fit. Open circles refer to XMM-Newton EPIC-pn observations in different modes, see [41; 43]. The errors of the data mark the 90% confidence intervals, while the errors of the long term period P_{pre} derived from the sine fit denote 1σ .

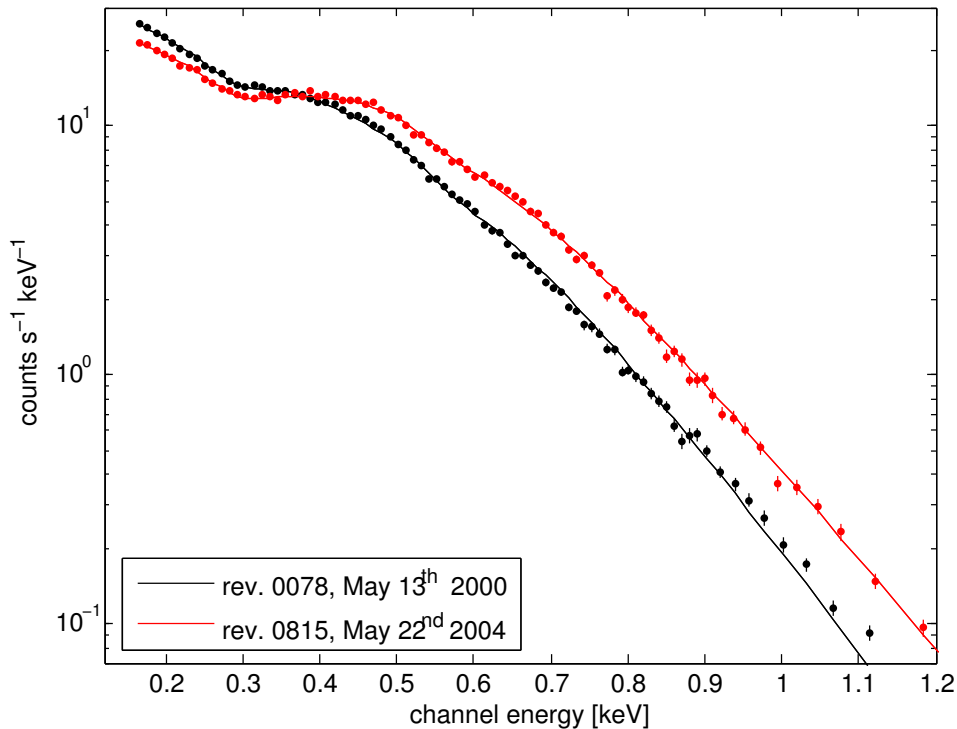


Figure 1.5: The XMM-Newton spectra of RX J0720.4–3125 with the lowest and highest measured temperatures ($T = 86.5 \pm 0.4$ eV and $T = 94.7 \pm 0.5$ eV for revolution 0078 and 0815, respectively) so far. The dots represent the measured data with Poissonian errors, the lines correspond to the best fitting model (black body with a broad absorption feature around 0.3 keV), see [22; 38; 41] for details.

appear in the line of sight (and vice versa for the other spot).

During precession the observer would see different parts of the surface that would cause changes in the spectral properties (if the hot spots are different in temperature and size), if two, roughly antipodal, hot spots would both contribute to the X-ray emission. The phase residuals caused from both hot spots would be shifted by $P_{pre}/2$: if one hot spot precesses towards the observer and appears (or larger parts of the spot become visible), the second hot spot moves backwards with respect to the observer and disappears (or smaller parts are visible). Since the timing analysis is not sensitive to which of the hot spots is causing the residuals, the phase residuals qualitatively may have the shape of an $\text{abs}(\text{sine})$, having twice the period of the corresponding sine (two peaks from two different hot spots). Moreover, this model also would explain the variable phase shift between hard (mainly emitted from the hotter spot) and soft photons (mainly emitted from the cooler spot) seen in the XMM-Newton EPIC-pn data. During the first observations around $\text{MJD} \approx 52000$ days, the hard photons lag the soft photons, then, around $\text{MJD} = 52800$ days, the soft photons lag the hard photons. Unfortunately, only with XMM-Newton EPIC-pn data it is possible to divide the photons into a hard and a soft band with sufficient statistics (see section 2.2),

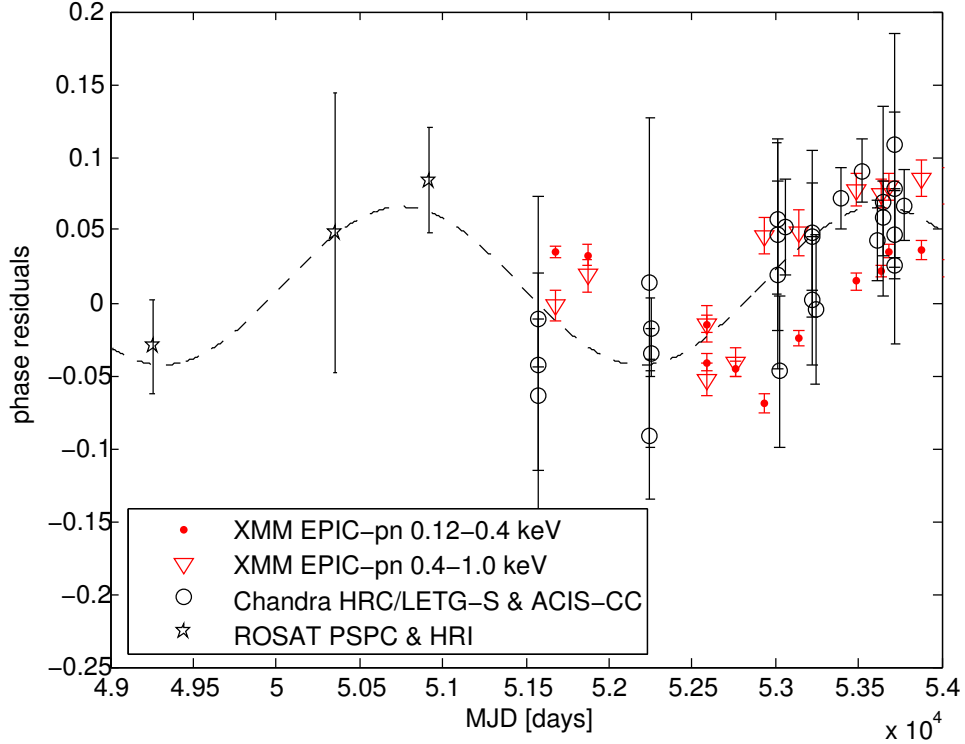


Figure 1.6: Phase residuals of RX J0720.4–3125 derived from different telescopes and detectors as presented in [38] using the phase coherent timing solution (constant spin-down) from [63]. The long term period $P_{pre} = 7.88 \pm 0.01$ yrs derived from the error weighted sine fit is similar to that found from the spectral variations (see figure 1.4). All errors denote 1σ . Note the systematic phase shift between the soft and the hard band in the XMM-Newton EPIC-pn data.

thus more data and an ongoing monitoring of RX J0720.4–3125 is needed to follow this behaviour further.

Alternatively, [129] proposed a glitch event that occurred around MJD=52800 days causing the behaviour of RX J0720.4–3125. A glitch could be caused by an accretion event, an impact of a massive object, or a star quake in the cooling neutron star crust. A glitch leads to a jump in the period, the spin frequency suddenly increases and the neutron star continues spinning down. Such glitches are known from many young radio pulsars and can occur up to a few times per year [55; 137; 146], i.e. are not unusual for young pulsars. The phase coherent timing solution including a glitch in [129] well explains the timing behaviour in the observations available at that time. It is argued that a glitch would release energy and the changes in the temperature are actually a jump, that will be followed by a slow, maybe exponential, cooling in the future and just looks sinusoidal in the data available at winter 2005 (MJD=53700 days). From the jump in the spin frequency the gain of momentum can be estimated that refers to a hypothetical impact mass of $10^{20} - 10^{21}$ g, the mass of an asteroid [129].

1. INTRODUCTION

While the glitch hypothesis does not explain the variable phase lag between hard and soft photons (see figure 1.6) and why the total luminosity of RX J0720.4–3125 remains constant, free precession¹ may contradict theoretical predictions, since it is expected that neutron stars consist of superfluid matter under their crust [78].

Precessing neutron stars would emit gravitational waves according to equation 1.7. Although the gravitational waves with a period of a few years like in the case of RX J0720.4–3125 cannot be measured yet and in the near future, proving precession would show that such classes of gravitational wave emitters that may contribute to the gravitational wave background (maybe with more capable precession periods) exist in principle. Then, assumptions about the physics of superfluids in neutron stars have to be reconsidered [34].

¹Precession powered by a companion is almost certainly excluded, see section 5.1.1

2

Data and data reduction

This work has made use of different X-ray telescopes. The main scientific results are obtained with XMM-Newton and Chandra (both, timing and spectroscopy), and the ROSAT data are used for some considerations regarding the timing analysis. RX J0720.4–3125 has also been observed with other X-ray telescopes (e.g. BeppoSax or Einstein); however, they did not contribute additional information to this work, thus are not discussed here.

In order to understand the selection criteria applied to the data from the different telescopes in later stages of the work, here a brief overview of the X-ray telescopes, their instruments and properties is given.

2.1 ROSAT

The German **R**öntgen **S**atellit (X-ray satellite ROSAT, [124]) was launched on June 1st 1990 and the mission was lead by the Max-Planck-Institut für extraterrestrische Physik (MPE). ROSAT worked until February 1999. The first six months after launch were devoted to the All Sky Survey. The ROSAT mission delivered fundamental insights into the physics of compact objects. During the mission, all M7 known today [38] were discovered. X-ray emission from some radio pulsars was already detected with the Einstein satellite but ROSAT gave a clearer picture of the faint X-ray emission produced by the cooling surface of nearby isolated neutron stars.

The two main instruments on board were the **P**osition **S**ensitive **P**roportional **C**ounter (PSPC) with a field of view of two degrees and an effective area of $\approx 240 \text{ cm}^2$ at 1 keV; and the **H**igh **R**esolution **I**mager (HRI, [21]), having a field of view of 38' with an effective area of $\approx 80 \text{ cm}^2$ at 1 keV. The spatial resolution of the HRI denotes 2". Both, PSPC and HRI, operate from 0.1 – 2.5 keV. A further instrument is the **W**ide **F**ield **C**amera (0.062 – 0.206 keV) that is not important for this work, thus is not introduced here.

Due to low statistics and low energy resolution, the ROSAT data could not be divided into

2. DATA AND DATA REDUCTION

Table 2.1: ROSAT observations of RX J0720.4–3125 in chronological order. For details on ROSAT observations see [19].

Obs. Id.	Instrument	total counts	<i>MJD</i> [days]	Start Date	Effective exposure [ks]
all sky survey	PSPC	725	48176	1990 Oct 11	–
rp300338n00	PSPC	5374	49258	1993 Sep 27	3.22
rh300508n00	HRI	1259	50199	1996 Apr 25	3.13
rh180100n00	HRI	1197	50211	1996 May 7	3.57
rh300508n01	HRI	493	50354	1996 Sep 27	1.41
rh400884n00	HRI	13381	50391	1996 Nov 3	33.57
h400944n00	HRI	3054	50924	1998 Apr 20	3.57

two energy bands, as done for XMM-Newton and Chandra data (see next sections). The photons from the PSPC were taken from channels ten to 90 (100 – 900 eV) and for the HRI from channels one to eight. The low countrate in the ROSAT data causes problems for timing, as will be seen later. The reduced and barycentric corrected ROSAT data were adopted from [19]. Details of the data reduction can be found therein. The photon arrival times in the ROSAT event files are counted from the individual observation day (minus half a day to start at noon), while the XMM-Newton and Chandra photon arrival times are counted from $MJD = 50814$ days (January, 1st 1998, 0:00), thus the ROSAT photon arrival times were modified to fit with the photon arrival times from the other telescopes. All ROSAT observations of RX J0720.4–3125 are listed in table 2.1.

2.2 XMM-Newton

The XMM-Newton satellite carries three X-ray telescopes [54] and was launched on December 10th 1999. It is the second cornerstone mission of the “Horizon 2000 Science Program” of the ESA and is still active. Three main instruments are onboard: the **E**uropean **P**hoton **I**maging **C**amera (EPIC), the **R**eflecting **G**rating **S**pectrometer (RGS) and the **O**ptical **M**onitor (OM). The OM is not relevant for the thesis and thus will not be introduced here. The EPIC consists of 3 CCD cameras: the EPIC-pn [120] and two EPIC-MOS [125] cameras, each one behind a multi-mirror telescope. Each X-ray telescope has a total geometric mirror area of 1550 cm², i.e. 4650 cm² in total. However, since only a part of the incoming light falls onto the MOS detectors, the effective areas are actually lower than that of the pn detector. The observations of XMM-Newton are assigned with the satellite revolution (“rev.”) number.

Table 2.2: XMM-Newton observations of RX J0720.4–3125 in chronological order. The counts of both RGS are given for 0.35 – 0.9 keV.

rev.	Instrument	setup	Counts (120 – 400 eV)	Counts (400 – 1000 eV)	<i>MJD</i> [days]	Start Date	Effective exposure [ks]
0078	EPIC-pn	FF thin	241783	115287	51677	2000 May 13	58.60
	EPIC-MOS1	FF thin	69623	43977			61.98
	EPIC-MOS2	SW thin	68010	40818			61.99
	RGS1			15900			48.89
	RGS2			15481			49.00
0175	EPIC-pn	FF medium	103491	55743	51870	2000 Nov 21	25.65
	EPIC-MOS1	LW medium	15765	11662			18.00
	RGS1			8711			30.25
	RGS2			7901			29.13
0533	EPIC-pn	FF thin	137951	72150	52585	2002 Nov 6	28.38
	EPIC-MOS1	FF thin	27987	21892			29.99
	EPIC-MOS2	FF thin	29169	22192			29.99
	RGS1			8541			29.61
0534	EPIC-pn	FF thin	145057	76095	52587	2002 Nov 8	30.18
	EPIC-MOS1	FF thin	28168	22112			31.80
	EPIC-MOS2	FF thin	28954	22768			31.79
	RGS1			8764			31.22
	RGS2			8225			30.22
0622	EPIC-pn	SW thick	123199	94655	52762	2003 May 2	72.79
	EPIC-MOS1	FF medium	21204	18741			29.98
	EPIC-MOS1	FF thin	28433	23754			33.59
	EPIC-MOS2	FF medium	21988	19650			29.99
	EPIC-MOS2	FF thin	30901	24413			33.59
	RGS1			22414			74.78
	RGS2			21433			74.72
0711	EPIC-pn	SW medium	83151	60557	52940	2003 Oct 27	24.90
	EPIC-MOS1	FF thin	10841	11937			13.90
	EPIC-MOS1	LW thin	10547	11769			15.71
	EPIC-MOS2	FF thin	11649	12392			13.91
	EPIC-MOS2	LW thin	11943	12382			15.71
	RGS1			14726			44.77
	RGS2			13477			44.77
0815	EPIC-pn	FF thin	130683	93280	53147	2004 May 22	41.30
	EPIC-MOS1	FF thin	35853	41178			45.21
	EPIC-MOS2	FF thin	35915	42318			45.22
	RGS1			17351			44.91
	RGS2			16270			44.91
0986	EPIC-pn	FF thin	181754	131146	53488	2005 Apr 28	51.43
	EPIC-MOS1	SW thin	32400	36475			53.05
	EPIC-MOS2	SW thin	34456	38266			53.06
	RGS1			18884			53.10
	RGS2			18398			53.08
1060	EPIC-pn	FF thin	175481	120913	53636	2005 Sep 23	51.14
	EPIC-MOS1	SW thin	33710	37070			52.76
	EPIC-MOS2	SW thin	33977	37706			52.77
	RGS1			18656			52.86
	RGS2			17519			52.83
1086	EPIC-pn	FF thin	167725	117828	53687	2005 Nov 12	37.84
	EPIC-MOS1	SW thin	25265	27091			39.46
	EPIC-MOS2	SW thin	25045	27580			39.47
	RGS1			12083			39.57
	RGS2			10812			39.55
1181	EPIC-pn	FF thin	89015	59524	53877	2006 May 22	20.04
	EPIC-MOS1	SW thin	13652	14219			21.66
	EPIC-MOS2	SW thin	15045	15048			21.66
	RGS1			6715			21.82
	RGS2			6125			21.79
1265	EPIC-pn	FF thin	89852	60883	54044	2006 Nov 5	20.04
	EPIC-MOS1	FF thin	12414	12296			21.61
	EPIC-MOS2	FF thin	15291	14653			21.62
	RGS1			6255			21.82
	RGS2			5789			21.81
1356	EPIC-pn	FF thin	89411	57483	54226	2007 May 5	20.04
	EPIC-MOS1	FF thin	16690	16685			21.61
	EPIC-MOS2	FF thin	17147	16818			21.62
	RGS1			6588			21.79
	RGS2			5797			21.78
1454	EPIC-pn	FF thin	102917	64833	54421	2007 Nov 17	23.06
	EPIC-MOS1	FF thin	18674	18197			24.62
	EPIC-MOS2	FF thin	19029	18416			24.62
	RGS1			6953			24.81
	RGS2			6054			24.81
1700	EPIC-pn	FF thin	37085	30806	54913	2009 Mar 21	10.84
	EPIC-MOS1	FF thin	11481	11876			17.69
	EPIC-MOS2	FF thin	11936	11556			17.69
	RGS1			6545			21.79
	RGS2			6719			21.79
1792	EPIC-pn	FF thin	65407	48105	55096	2009 Sep 22	17.90
	EPIC-MOS1	SW thin	12524	11919			19.22
	EPIC-MOS2	SW thin	12724	11993			19.24
	RGS1			5368			19.21
	RGS2			5437			19.21

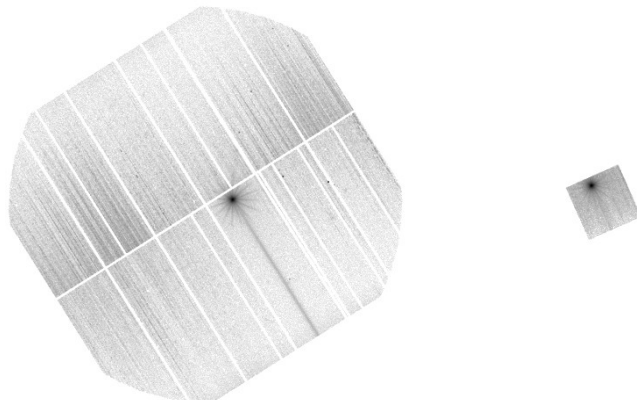


Figure 2.1: View on the EPIC-pn detector (120 – 1200 eV) in full frame mode (revolution 0078, left) and small window mode (revolution 0622, right). The bright object in the centre is RX J0720.4–3125 and the bright streak is caused by the readout of the detector. Note, that no other bright object influences the data in the selected energy band.

2.2.1 EPIC-pn

The EPIC-pn detector is a back-illuminated CCD chip having twelve (4×3) single chip panels, each of it has 64 columns (with 200 pixel, 188 of them are used) with its own readout node. Generally, this leads to better time resolution than for the MOS1 and MOS2 detectors. The CCD array has a total size of 376×384 pixel (188×64 for each of the twelve panels), each pixel corresponds to $4.1''$. The readout for the entire chip (full frame mode, hereafter FF mode) has a time resolution of 73.4 ms, while a spatially restricted readout mode increases the time resolution. Further readout modes are the large window mode (LW) with 48 ms (198×384 pixel) and the small window mode (SW, 63×64 pixel) with 6 ms readout time. The observations performed with EPIC-pn are done in the FF and SW mode, see figure 2.1. Since RX J0720.4–3125 has a period of 8.39 s, the time resolution of the instrument is fully sufficient. Other readout modes are the timing mode and the burst mode with a time resolution of 0.03 ms and 7 μ s, respectively. The effective area of the pn detector amounts $\approx 1400 \text{ cm}^2$ at 1.5 keV.

If a photon impacts on the CCD it causes a charge cloud that is a measure of energy, i.e. the EPIC-pn detector can be used for spectroscopy. RX J0720.4–3125 is a relatively bright X-ray source and an impact of two low-energy photons within the CCD frame time can mimic a high-energy event. This phenomenon is called photon pile-up. The pile-up depends on the readout mode, i.e. decreases for faster readout modes. Even for the full frame mode, the pile-up is negligible for RX J0720.4–3125.

To reduce the incidence of optical light all RX J0720.4–3125 observations performed with

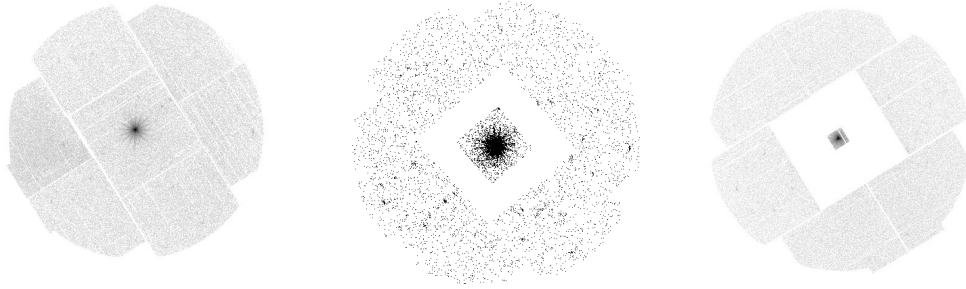


Figure 2.2: View on the MOS detector (120 – 1200 eV, both MOS are equal, only rotated) in full frame (revolution 0078, MOS1, left), large window (revolution 0175, MOS1, middle) and small window (revolution 0078, MOS2, right) mode.

XMM-Newton are done with a filter, where the thin filter is fully sufficient in this case. RX J0720.4–3125 was considered to be a constant source like RX J1856.4–3754 and was used for calibration issues. Therefore, at the beginning of the mission, observations in medium and thick filter were done. Thicker filters mainly block softer photons below ≈ 0.4 keV compared to the thin filter.

The band pass of the EPIC-pn detector is 0.10 – 15 keV, according to previous publications [38; 41; 43] photons from 0.12 – 1.2 keV where used in this work. The spectral resolution is ≈ 100 eV for single-pixel events at 1.0 keV but gets worse for lower energies.

2.2.2 EPIC-MOS1 and EPIC-MOS2

The MOS detectors are both front-illuminated and consist of an array of seven quadratic CCD arrays (one pixel corresponds to 1.1"). Band pass and spectral resolution for the MOS detectors are comparable to the pn detector. The same set of filters as for EPIC-pn is available. In FF mode (600×600 pixel) the time resolution is 2.6 s, i.e. 30% of the pulse period of RX J0720.4–3125. For the LW (300×300 pixel) and the SW (100×100 pixel) mode the time resolutions are 0.9 s and 0.3 s, respectively. A further readout mode is the MOS timing mode (1.75 ms). All data for RX J0720.4–3125 are obtained from observations done in the FF, LW and SW mode, see figure 2.2.

2.2.3 RGS1 and RGS2

In contrast to the pn and MOS imaging detectors, the RGS [23] are grating spectrometers, i.e. the dispersion angle of the incident light depends on the photon energy. For both RGS the first and second orders are relevant, while the count rate in the third order is about eight times less than for the second order. Actually, following the design of the detector, the 1st and 2nd orders are the -1^{st} and -2^{nd} orders, respectively. The band passes for both RGS are 0.35 – 2.5 keV (1st order) and 0.62 – 2.5 keV (2nd order).

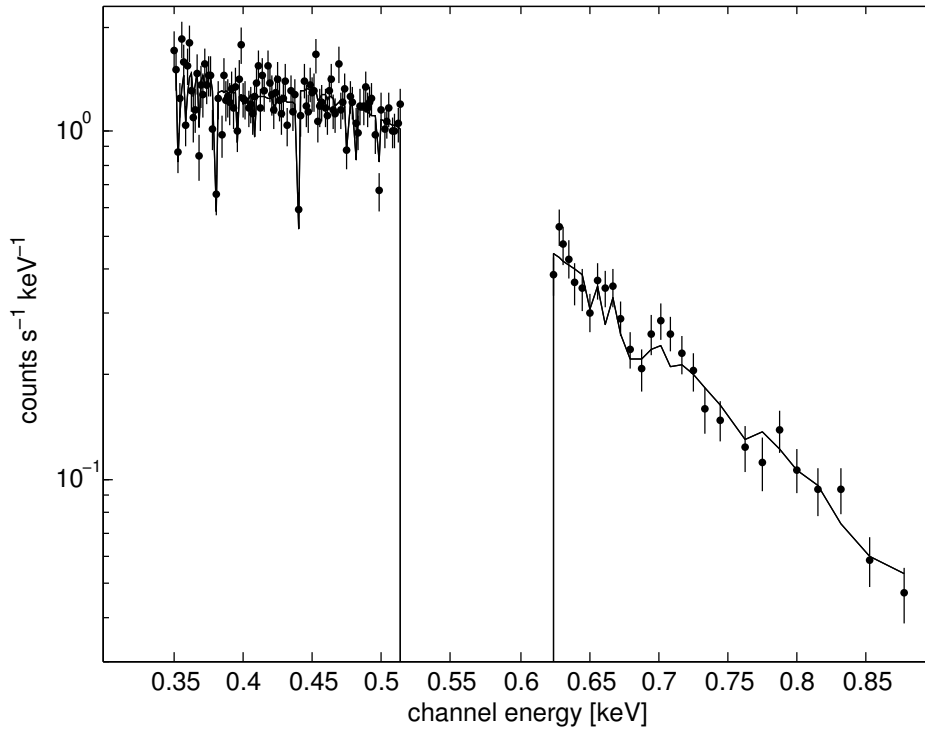


Figure 2.3: The RGS2 spectrum of RX J0720.4–3125 from the XMM-Newton observation revolution 0078. The failure of chip four is responsible for the data gap and the solid line represents the best fit model of a black body with a Gaussian absorption line, see table 4.1 in section 4.1. The errors are Poissonian, see also figure 1.5 for comparison.

The RGS are suitable for high resolution spectroscopy of bright sources with a resolution of 3.2 eV and 2.0 eV at 1 keV for the 1st and the 2nd order, respectively.

During the operation of XMM-Newton, chip seven of RGS1 (0.90 – 1.18 keV) and chip four of RGS2 (0.52 – 0.62 keV) failed. While RX J0720.4–3125 has a low count rate around 1.0 keV (see figure 1.5) and the failure of chip seven in RGS1 is negligible, the failure of chip four in RGS2 causes a significant gap in the spectrum of RX J0720.4–3125 (figure 2.3).

2.2.4 Reduction of XMM-Newton data

At the beginning of the work in December 2007, 13 XMM-Newton observations of RX J0720.4–3125 were performed and available in the archive. From these 13 observations, the first 11 have been reduced and analysed before. In November 2007, the observation during revolution 1454 had been executed. These 14 observations have been analysed and reprocessed with the standard XMM-Newton **Science Analysis System** (SAS) version 7.1.0. In March 2009 another XMM-Newton observation was performed [130] (revolution 1700) and finally in September 2009 the most recent observation of RX J0720.4–3125 (revolution

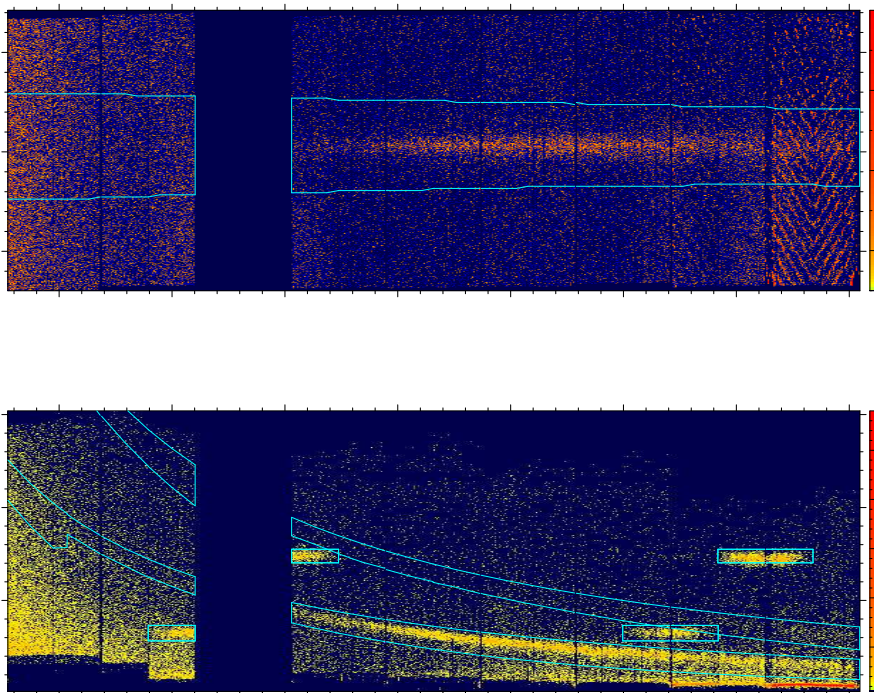


Figure 2.4: The spatial dispersion plot (upper panel) and energy dispersion (lower panel) plot of RGS1. The blue lines indicate the default extraction regions for the source photons (banana like curves in the lower panel) and the calibration sources (short horizontal regions in the lower panel). Chip seven is defect and excluded.

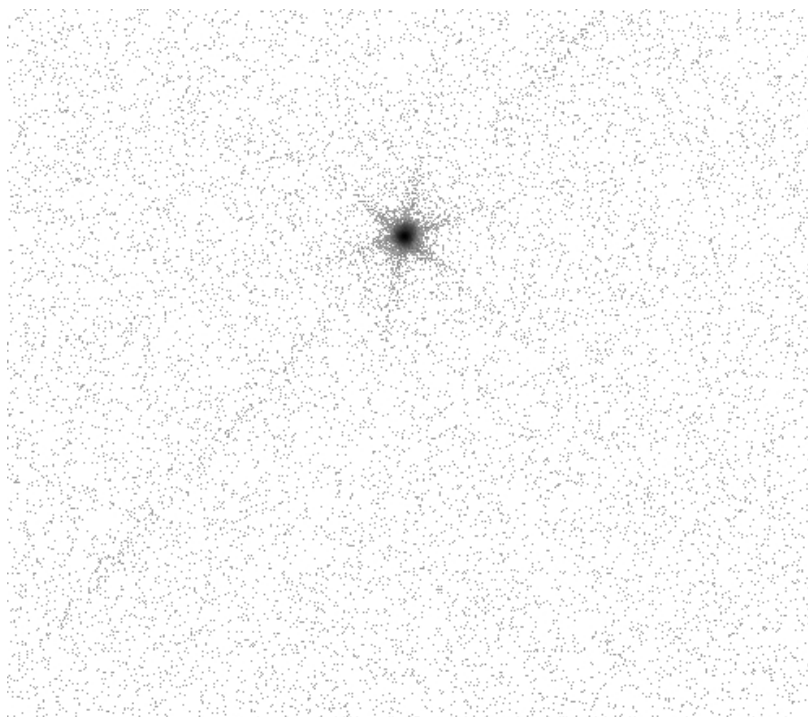


Figure 2.5: The zeroth order image of RX J0720.4–3125 obtained from the Chandra observation 5582 using HRC-S/LETG.

2. DATA AND DATA REDUCTION

1792) could be added [49]. The last two data sets were analysed with the SAS version 9.0.0, but following the same procedure as for the previous observations. Our team plans to continue the monitoring of RX J0720.4–3125 and the last XMM-Newton proposal [50] was accepted, but not executed so far (priority C). All observations are listed in table 2.2. The software for data reduction and data preparation for spectroscopy were adopted from Frank Haberl (see [41; 43]) and the codes were only slightly modified for MOS and RGS data reduction.

The pn data was analysed using the *epchain* command, the MOS data using *emchain*. To reduce the contamination of the data by increased fluxes of soft protons in the solar wind, all data sets passed the filtering by the **Good Time Intervall** (GTI) files that were generated during the standard data reduction process. However, for the observation revolution 1700 both MOS have 30% background flaring time, while almost 40% flaring time for the pn detector was reported in the observation protocol. The MOS exposures were interrupted and re-started (1.5 ks scheduled observations, afterwards 12 ks as unscheduled) during flaring so that 5 ks were filtered out by the GTI files, producing sufficiently clean data. In the case of pn the observation was not interrupted and the first half of the observation was highly contaminated. The GTI files still left contaminated time intervals, thus for this observation only the second half of the observation was used after passing the GTI filters.

Finally, for timing purposes, the barycentric correction (regarding all leap seconds added during the years) was applied and the photons were divided into a soft (120 – 400 eV) and a hard (400 – 1000 eV) energy band (see section 3.3).

Most photons are recorded in a single CCD pixel, but some events are splitted between different CCD-pixels (if two “doubles”, if three “triples” and if four “quadruples”) and are flagged by different pattern numbers. Such events have to be recognised to reconstruct a single energy value. Note, that higher patterns are identified with pile-up, silicon fluorescence or cosmic rays (see [120] for a more detailed explanation). For all XMM-Newton CCD detectors single events were used for spectroscopy and were collected within a circular region of 30” (pn) and 8” (MOS) radius (i.e. the source plus background photons). The background photons, needed for background correction of the spectra, were obtained from a circular region of the same size, located on the same chip as the source photons. This was not possible for MOS SW observations, thus the background photons were taken from a neighbouring chip.

The data reduction of the RGS data was performed with the SAS versions mentioned above, using the *rgsproc* command. After the application of the standard GTI files the photons for the spectra were obtained from the default RGS extraction regions shown in figure 2.4.

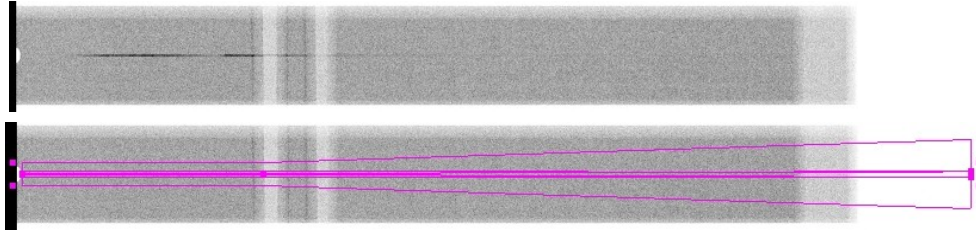


Figure 2.6: The first orders of RX J0720.4–3125 obtained from the Chandra observation 5582 using HRC-S/LETG. Both orders are superimposed (the zeroth order is cut out and would be located on the left site), the two vertical white shaded stripes in both panels are caused by gaps between the detector chips.

Upper panel: the source photons are indicated by the black horizontal stripe (higher count rate).

Lower panel: The overlaid default extraction regions. The central region is used for source plus background photons, the two bow-tie shaped areas are used for the background photons.

2.3 Chandra

The Chandra space craft was launched on July 23rd 1999 by NASA and is still active. Chandra hosts two imaging and readout devices: the **A**dvanced **C**CD **I**maging **S**pectrometer (ACIS, [31]) and the **H**igh-**R**esolution **C**amera (HRC, [73]); and two gratings: the **H**igh **E**nergy **T**ransmission **G**rating (HETG, [24; 25]) for a range of 0.4 – 10 keV and the **L**ow **E**nergy **T**ransmission **G**rating (LETG, [30; 58; 59]) working at 0.07 – 10 keV. Generally, Chandra facilities have a higher spatial resolution than those of XMM-Newton but a much smaller effective area (total 800 cm² and 400 cm² at 0.25 keV and 5.0 keV, respectively), i.e. suffer from a lower number of photons compared to XMM-Newton observations with the same exposure time. While on XMM-Newton all instruments observe simultaneously, on Chandra only one instrument can be used at the time.

The Chandra telescope does not steady fix the target while observing, but performs a dithering. This avoids unexposed areas in the observed sky field due to detector structures (CCD gaps, dead pixels etc.). The data reduction software takes the dithering into account (aspect correction).

2.3.1 HRC-S/LETG

The HRC device consists of two detectors, one optimised for imaging (HRC-I) and one for spectroscopy if used with grating (HRC-S). For RX J0720.4–3125 the HRC-S detector was used in combination with the LETG (i.e. HRC-S/LETG) having an energy resolution of $\Delta E/E \geq 1000$ between 0.08 keV and 2.0 keV for the dispersed photons (+1st and –1st orders). The zeroth order is an image of the source.

Both HRC detectors have a spatial resolution of 0.5", whereas the field of view for HRC-S

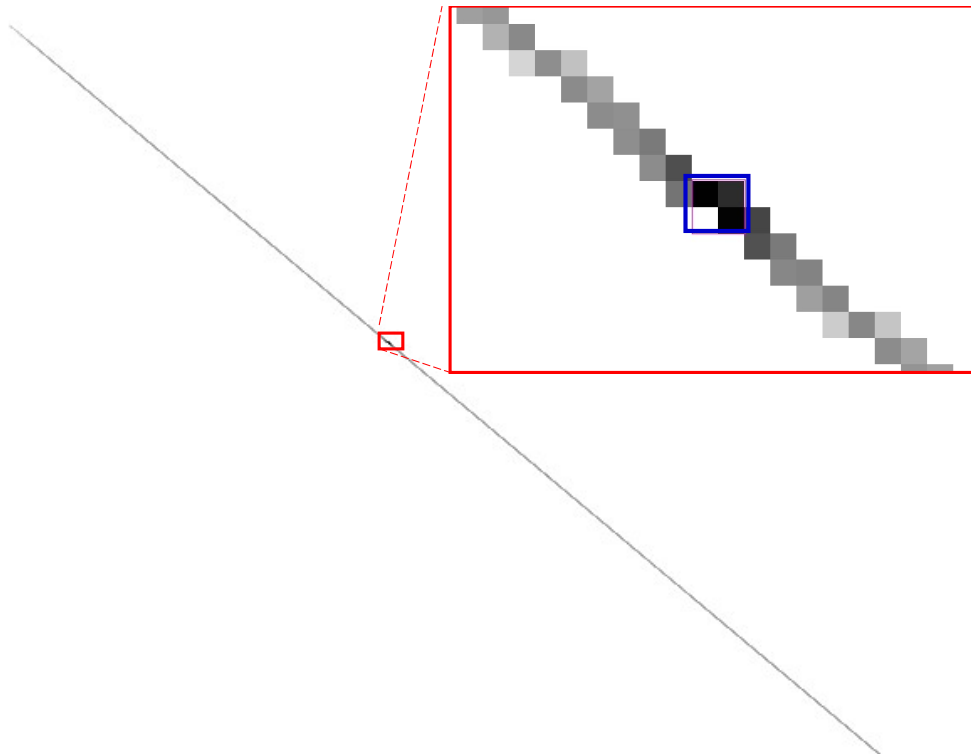


Figure 2.7: The image of RX J0720.4–3125 in ACIS-CC mode from the Chandra observation 2774. The extraction region (blue rectangle) is zoomed (red rectangle). In the two brightest pixels already ≈ 10 to 15 times more counts are detected than in the brightest neighbouring pixels.

is $7' \times 97'$ having an effective area of $\approx 30 \text{ cm}^2$ at 1 keV (50 times less than XMM-Newton EPIC-pn and two times less as for the -1^{st} orders of both RGS in total). Important for timing is the high temporal resolution of $16 \mu\text{s}$, i.e. 5000 times higher than for EPIC-pn FF mode. However, due to a wiring error in the HRC detector, the arrival time of an event is associated with the arrival time of the following event¹ and decreases the time resolution to the mean time between the events. Since the arrival time of a photon is always assigned to the next photon and the pulse period of RX J0720.4–3125 is relatively large, the determination of the period is not influenced and the effects on timing are negligible.

2.3.2 ACIS-CC

The ACIS detector has two CCD arrays with a total of ten chips. Each chip has a size of 1024×1024 pixel, where one pixel corresponds to $0.5''$. Eight chips are front illuminated, two are back illuminated with both configurations having an effective area of $\approx 340 \text{ cm}^2$ at 1 keV. In all cases, RX J0720.4–3125 was observed in the **C**ontinuous **C**lock (CC) mode,

¹<http://cxc.harvard.edu/ciao4.2/caveats/hrc-timing.html>

Table 2.3: Chandra observations of RX J0720.4–3125 in chronological order. The identifier mark the merged data sets: observations with the same tag are merged into one data set. The counts from Chandra HRC data are not divided into hard and soft band, therefore the total numbers of counts are listed.

Obs. Id.	Instrument	Counts (120 – 400 eV)	Counts (400 – 1000 eV)	<i>MJD</i> [days]	Start Date	Effective exposure [ks]
368 ¹	HRC-S/LETG		2722	51575	2000 Feb 1	5.40
745 ¹	HRC-S/LETG		9392	51576	2000 Feb 2	26.26
369 ¹	HRC-S/LETG		2660	51579	2000 Feb 4	6.12
2774 ²	ACIS-CC	13455	15648	52248	2001 Dec 4	15.01
2773 ²	ACIS-CC	9452	11646	52248	2001 Dec 5	10.61
2771 ²	ACIS-CC	876	1553	52250	2001 Dec 6	1.86
2772 ²	ACIS-CC	3537	4487	52250	2001 Dec 6	4.05
4666 ³	ACIS-CC	5606	13094	53010	2004 Jan 6	10.12
4667 ³	ACIS-CC	2678	5835	53011	2004 Jan 7	4.79
4668 ³	ACIS-CC	2121	4918	53016	2004 Jan 11	5.16
4669 ³	ACIS-CC	1890	4277	53023	2004 Jan 19	5.22
5305 ⁴	HRC-S/LETG		13275	53062	2004 Feb 27	35.70
4670 ⁵	ACIS-CC	5723	12329	53221	2004 Aug 3	10.13
4671 ⁵	ACIS-CC	2778	6318	53223	2004 Aug 5	5.15
4672 ⁵	ACIS-CC	2483	5789	53227	2004 Aug 9	5.12
4673 ⁵	ACIS-CC	2527	6034	53244	2004 Aug 23	5.13
5581 ⁶	HRC-S/LETG		30998	53393	2005 Jan 23	68.20
5582 ⁷	HRC-S/LETG		35777	53523	2005 Jun 1	70.17
6364 ⁸	HRC-S/LETG		22210	53610	2005 Aug 27	38.87
6369 ⁹	HRC-S/LETG		7696	53652	2005 Oct 8	26.26
7177 ⁹	HRC-S/LETG		2532	53653	2005 Oct 9	8.04
7243 ¹⁰	HRC-S/LETG		5931	53718	2005 Dec 14	17.18
7244 ¹⁰	HRC-S/LETG		4927	53718	2005 Dec 15	16.29
7245 ¹⁰	HRC-S/LETG		5249	53718	2005 Dec 16	17.19
5584 ¹⁰	HRC-S/LETG		5321	53718	2005 Dec 17	14.19
7251 ¹¹	HRC-S/LETG		4787	53775	2006 Sep 9	10.65
10861 ¹²	HRC-S/LETG		4240	54851	2009 Jan 20	11.91
10700 ¹²	HRC-S/LETG		14053	54876	2009 Feb 14	21.82
10701 ¹³	HRC-S/LETG		15647	55086	2009 Sep 11	33.17

i.e. ACIS-CC. In this mode, the spatial information of the photons is lost and the data are read into a 1×1024 pixel image. Due to this readout mode, the integration time, i.e. temporal resolution, improves to 2.85 ms.

2.3.3 Reduction of Chandra data

At the beginning of the work, 26 Chandra observations performed in HRC-S/LETG and ACIS-CC mode were available (last observation in September 2006). Since the MPE contributed to the development of the HRC gratings, **Guaranteed Time Observation (GTO)** could be used to add three more observations. The monitoring of RX J0720.4–3125 using HRC GTO is still continuing. For timing purposes, most Chandra observations are executed as short exposures of a few ks, repeated several times within a few days. These observations

2. DATA AND DATA REDUCTION

were merged assuming that no significant changes in the properties of RX J0720.4–3125 occurred within such a short time scale (in comparison to the long term changes over years). Due to merging, the 29 observations were reduced to 13 data sets, see table 2.3.

The Chandra data were analysed with CIAO 4.1. For HRC-S/LETG the photons of the zeroth order were collected from a circular region of 2" radius, see figure 2.5. The photons from both first orders were cut out within the standard LETG spectral extraction windows (see figure 2.6), but limited to 10 – 60 Å (1240 – 207 eV) and the two brightest horizontal pixel stripes only, to minimise the contribution of background noise. To prepare the HRC-S/LETG data for spectroscopic fitting in *Xspec* (see section 4.1), the background was generated with the command *tg–bkg*.

Before proceeding with the ACIS-CC data it was checked that the observations were processed with the **Standard Data Processing (SDP)** version DS 7.6.3. or later to guarantee best corrections of the readout times and dithering. The coordinate accuracy for all ACIS-CC observations is better than 0.5", i.e. one pixel. The **Charge Transfer Inefficiency (CTI)** correction was applied and the source photons from a rectangular region covering the brightest pixels (located on chip seven for all ACIS-CC observations) were extracted, see figure 2.7.

As mentioned previously, an important issue for the timing of RX J0720.4–3125 is the phase shift between hard and soft band. For HRC, the energy information in the zeroth order is lost. This regards 40% of the total amount of photons. The hard photons extracted from the two first orders would only equate 20% of the total amount of photons. However, for timing purposes, the light curves have to be binned in ten phase bins or more and a low number of photons would lead to a large scatter in the light curves, thus the HRC photons were not divided in the two bands. Note that the total number of photons from Chandra observations (even if not divided in bands) is much lower than for XMM-Newton observations (see table 2.2 and table 2.3).

In all cases the implementation of the correct bad pixel file was checked with the command *plist ardlib* and it was set with *pset ardlib*, if necessary. The barycentric correction for the HRC and ACIS-CC data was applied using *axbary*. Note that the orbit ephemerids, needed for the barycentric correction, are provided as "level=0" data files directly after an observation is performed. However, these ephemerids are extrapolations and are not sufficient for pulsar timing, thus "level=1" ephemerids were used only (these are available a week after the observation is performed).

3

Pulsar timing

The goal of pulsar timing is to determine P and \dot{P} and higher orders of the period derivatives yielding age, magnetic field strength and braking index according to equation 1.6 and equation 1.4. In contrast to radio pulsar timing, the observations of X-ray pulsars deliver a table of arrival times for each single photon, an event list. To account for the special requirements of X-ray pulsar timing special algorithms (for period detections and phase coherent timing) are discussed here. These algorithms were implemented and tested for this thesis and were written in *Matlab*¹.

In general, the phase ϕ of the signal evolves as

$$\frac{d\phi(t)}{dt} = \frac{2\pi}{P(t)}. \quad (3.1)$$

If the simple model with a constant spin-down is used, the period evolves with respect to a reference time t_0 ,

$$P(t) = P(t_0) + \dot{P} \cdot (t - t_0). \quad (3.2)$$

Using equation 3.2 to integrate equation 3.1 leads to an expression for the phase difference

$$\phi(t) - \phi(t_0) = \frac{2\pi}{\dot{P}} \ln \left[1 + \frac{\dot{P}}{P(t_0)} (t - t_0) \right]. \quad (3.3)$$

An arbitrary continuous (i.e. without a glitch) phase evolution can be represented by a series

$$\phi(t) = \phi(t_0) + f(t - t_0) - \frac{\dot{f}}{2}(t - t_0)^2 + \frac{\ddot{f}}{6}(t - t_0)^3 \dots \quad (3.4)$$

with f being the frequency. In this work, equation 3.4 was used for the phase coherent

¹version 7.6.0.324 (R2008a)

timing (according to equation 3.2 [63; 129], without a glitch) only up to the second order (constant spin-down).

In principle, one could measure P for different observations and fit a slope to derive \dot{P} . However, this is not possible for RX J0720.4–3125 since the individual periods from the single observations are not accurate enough, as will be seen later. Therefore, more advanced methods are required.

3.1 Phase coherent timing

Determining the period P_0 from the first observation yields the error ΔP_0 depending mainly on the observed time span, e.g. following the error estimation in [72]. From the given error, one can determine the time span until extrapolations for the phase (e.g. the phase of the maximum light) are reliable. This time span is less than $P_0/\Delta P_0$ cycles corresponding to the loss of one period cycle. If the next observation lies within this time span, its light curve can be folded into P_0 . The phase difference of the maximum light from the second observation with respect to the reference observation results from ΔP_0 , i.e. a new period P_1 can be found to minimise the phase residual. The new error ΔP_1 depends on the time span between the two observations, i.e. is much smaller than ΔP_0 .

This procedure is repeated iteratively including the next observations closest in time, evaluating the period and its error by minimising the phase residuals. If the modulus of the phase residuals increases while evaluating the period, the phase difference contributed by \dot{P} becomes important, i.e. according to equation 3.4 a second term has to be included.

To accomplish phase coherent timing, the reference observations have to be performed as short exposures repeated two to three times a few days after the first observation. This was done with the ACIS-CC observations 4666 to 4669 followed by the HRC-S/LETG observation 5305 corresponding to a base line of 52 days, see table 2.3.

3.2 Algorithms for period detections

Since arrival times of each single photon are measured and the event list contains entries for some 10^3 to 10^5 photons (depending on exposure, detector and telescope) over a time span of one to 100 ks including time gaps, special algorithms have to be implemented for period detection and some pre-work is necessary.

The emission/detection of a photon (event) follows a Poissonian distribution, i.e. the probability \mathfrak{P} for a particular sequence of signals is

$$\mathfrak{P} = \prod_{i=1}^N \frac{s_i^{n_i} e^{-s_i}}{n_i!} \quad (3.5)$$

if s_i is the expected number of counts per bin and n_i is the measured number of counts per bin at the end of the experiment. The total number of bins is N with respect to a finite area, energy range and time resolution of the detector, i.e. $s_i = W(x_i; y_i; \nu_i; t_i) \delta x \delta y \delta \nu \delta t$. The function W has to be assumed, e.g. for RX J0720.4–3125, W seems to be a sinusoid according to figure 1.3, upper panel. In this case, W has four parameters (offset, amplitude, frequency/period and phase¹), or five parameters, if the frequency/period is changing according to equation 3.4 (again, truncating after the second order). Generally, W has p parameters and may have an arbitrary character.

3.2.1 Z_n^2 test

If photons from a particular detector area in a fixed energy band are extracted and since the sampling duration tends to zero for RX J0720.4–3125, $n_i = 1$ and N is the total number of counts. Following [13] the Z_n^2 test (here n is the number of orders, following the common terminology) was applied with

$$Z_n^2 = \frac{2}{N} \sum_k^n \left[\sum_i^N \cos k \phi_i \right]^2 + \left[\sum_i^N \sin k \phi_i \right]^2 \quad (3.6)$$

where ϕ_i is the phase according to equation 3.4. For a single observation the phase shift from \dot{P} is negligible. The probability density function of Z_n^2 is equal to that of χ^2 with $2n$ degrees of freedom [13]. This makes it feasible to infer the errors directly [110].

The Z_n^2 code was tested checking the results in [63] and [129].

3.2.2 Cash statistics and maximum likelihood

Starting from equation 3.5 the Cash [17] value (or C value; although misleading often called "Cash statistics" or " C statistics") from the maximum likelihood is

$$C = -2 \ln \mathfrak{P} = 2 \left(E - \sum_{i=1}^N n_i \ln W_i \right). \quad (3.7)$$

As before, $n_i = 1$ and E is the total number of counts expected from the model distribution. Following [17], a minimum of C from equation 3.7 has to be found by varying all parameters p over a search grid of q parameters (for example $q = 2$ if P and \dot{P} are varied). This

¹Amplitude and offset can be scaled together and the actual number of parameters is actually one less, as will be seen later.

3. PULSAR TIMING

minimum value of C has to be subtracted from the minimum C value found at any particular point at the search grid, i.e. $\Delta C = C_{min}^{best} - C_{min}^{part}$. ΔC is distributed as χ^2 with q degrees of freedom leading immediately to confidence intervals.

According to [19] and from equation 3.3 the model prescription

$$W(t) = a_0 \left\{ 1 + A \cos \left[\frac{2\pi}{\dot{P}} \ln \frac{P(t)}{P_0} + \theta_0 \right] \right\} \quad (3.8)$$

was used. Substituting equation 3.8 into equation 3.7 and calculating ΔC eliminates all scaling factors of the model, such as a_0 , i.e. $p = 4$ (not $p = 5$) and $q = 2$ if P and \dot{P} are varied and $p = 3$ and $q = 1$ if only P is varied, respectively. The amplitude A and the phase θ_0 of the model signal are derived following the instructions in [151] using the Rayleigh power for a sinusoid, similar to the expression in equation 3.6.

The Cash statistics code was tested checking the results and figures in [151] (the appendix therein) and the results in [19]. The individual periods derived from the Z_n^2 test and from Cash statistics are consistent for each observation and only deviate within their 1σ errors for the ROSAT observations. In most cases even the error derived from the estimation in [110] equals that derived from the confidence intervals using Cash statistics. For example both methods (and both error estimations) yield a period of $P = 8.391085(85)$ s (numbers in parenthesis indicate the 1σ error on the last two digits) with the same error value for the XMM-Newton observation revolution 1454 (hard band), see figure 3.1. Estimating the error with the formal Rayleigh resolving power $\Delta P = P^2/2/\Delta T_{observed}$ leads to a much larger error of $\Delta P = 0.0015$ s, while the error estimation in [72] yields an error of $\Delta P \approx 2.5 \times 10^{-5}$ s (depending on the number of phase bins of the phase folded light curve), that is smaller but comparable to $\Delta P \approx 8.5 \times 10^{-5}$ s using the estimation in [110] or the confidence intervals derived from Cash statistics.

3.2.3 String length

The two methods introduced for period detection need a model prescription as input. Although the assumption of a sinusoid (e.g. equation 3.8 and equation 3.6) leads to sufficient results (see figure 3.1) in the case of RX J0720.4–3125, the function $W(t)$ may have any shape.

For each trial period, the signal can be folded into phase. If the trial period hits the true value, the phase folded light curve has a minimum length [14], i.e. the expression

$$S = \sum_{i=1}^{n-1} \left[(y_i - y_{i-1})^2 + (x_i - x_{i-1})^2 \right]^{1/2} + \left[(y_1 - y_n)^2 + (x_1 - x_n)^2 \right]^{1/2}, \quad (3.9)$$

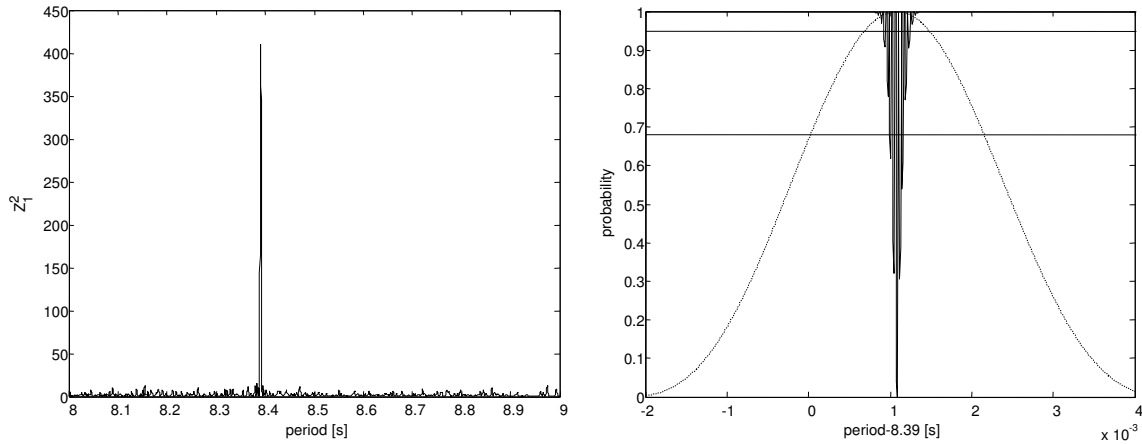


Figure 3.1: **Left:** The periodogram for the XMM-Newton observation revolution 1454 of RX J0720.4–3125 (hard band) derived from the Z_n^2 test with the first order $n = 1$ only. **Right:** The same as on the left, but zoomed in and the Z_1^2 value is normalised to one to illustrate the cumulative density function derived from ΔC (black shaded area) on the same scale. The horizontal lines indicate the 1σ and 2σ confidence intervals of the period.

where x is the phase and y the quantity such as counts per phase bin i , becomes small. For the wrong period, the phase binned light curve just equals noise and S , the string length, becomes large [27]. This is valid for any signal shape. The string length method has its advantage for sparse data sets with arbitrary time spacing such as the measured phase residuals of RX J0720.4–3125, e.g. see figure 1.6. The string length method was also tested for the event files of the individual observations. However, the other methods are more appropriate for the period detection of the individual observations (see figure 3.2).

3.3 Why the hard band?

In previous works [41; 43; 51] the photons were divided into a soft (120 – 400 eV) and a hard band (400 – 1000 eV) for the EPIC-pn detector to illustrate the phase shift between these two bands. In this section the necessity of the separation of the photons into two bands if data from different instruments are used is demonstrated and it is shown at which energy the band cut-off has to be made to accomplish a proper timing solution. Such an investigation was not performed before (e.g. in [63; 129]) although the phase shift was already known [22].

Since the variable phase lag between soft and hard photons (see figure 1.6) affects the phase coherent timing solution and in order to minimise systematic errors between EPIC-pn, MOS1, MOS2 and Chandra data (see also the discussion in [51]) a restriction to the hard energy band seems useful. As mentioned previously, HRC observations have a low number of photons and the energy information of the photons in the zeroth order is lost.

3. PULSAR TIMING

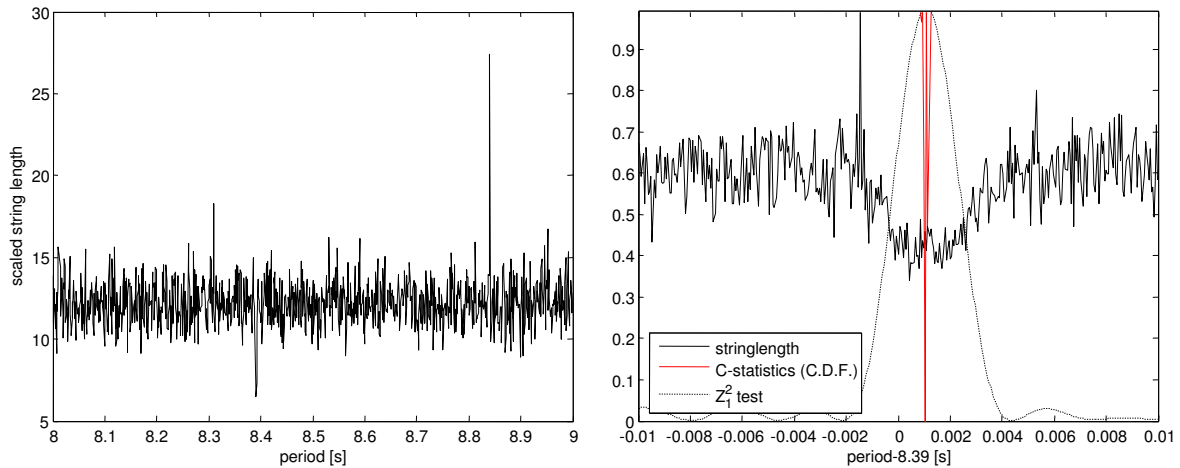


Figure 3.2: Left: The periodogram for the XMM-Newton observation revolution 1454 of RX J0720.4–3125 (hard band) derived from the string length method. The string length value is scaled according to [27].

Right: The same as the left panel, but zoomed in. Both, the Z_1^2 value and the string length, are normalised to one to illustrate the cumulative density function (C.D.F.) derived from ΔC on the same scale.

Therefore all photons from the HRC data were included.

The spectral resolution of the MOS detectors is ≈ 100 eV in the soft band [125]. Taken at the same time, the phase residuals from the XMM-Newton observations should be comparable to those of the Chandra observations. However, this works only when taking into account different energy response, spectral resolution and the phase shift between hard and soft photons (softer photons are less prominent in the MOS, HRC and ACIS data than in the pn data), influencing the residuals. This was shown in [51], figure 1 therein and [38], figure 7 therein.

This statement was checked using those Chandra observations performed close in time to XMM-Newton observations: The HRC observation 5582 (June 1st, 2005) is close to the XMM-Newton observation revolution 0986 (April 28th, 2005), the HRC observations 6369 and 7177 (October 8th/9th, 2005) are close to the XMM-Newton observation revolution 1060 (September 23rd, 2005), the HRC observations 7243–7245 (December 14th–17th, 2005) are close to the XMM-Newton observation revolution 1086 (November 11th/12th, 2005), the HRC observations 10861 and 10700 (January 20th and February 14th, 2009) are close to the XMM-Newton observation revolution 1700 (March 21st, 2009) and the HRC observation 10701 (September 11th, 2009) is close to the XMM-Newton observation revolution 1792 (September 22nd, 2009); see also table 2.2 and table 2.3.

Assuming that the timing properties of RX J0720.4–3125 do not change significantly within a time span of a month, the timing residuals (using the “all data” timing solution in [129] according to equation 3.4) of these observations were compared by changing the band cut

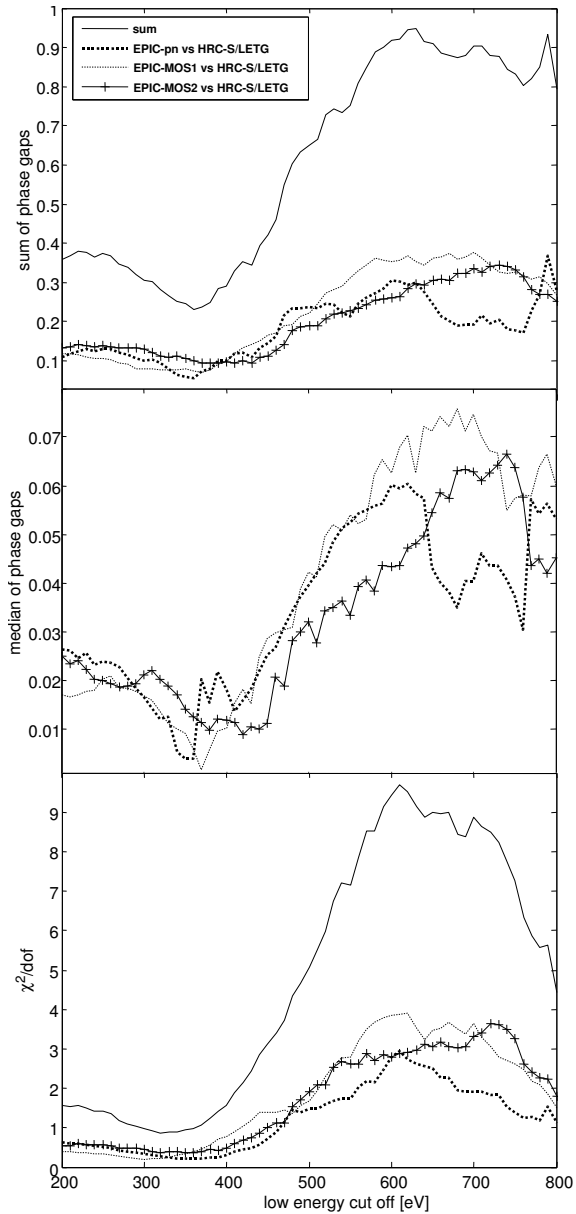


Figure 3.3: The accordance of the phase residuals of the hard band (cut off energy–1000 eV) for XMM-Newton EPIC-pn, EPIC-MOS1 & MOS2 and Chandra HRC of RX J0720.4–3125 for different values of the energy band cut. Data sets taken with different telescopes were selected in such a way that they are as close in time as possible. The upper panel shows the sum of the absolute values of the phase differences (phase gaps) derived from the different instruments with respect to each other, while the middle panel shows the median of these phase gaps and the corresponding $\chi^2/d.o.f.$ is presented in the lower panel.

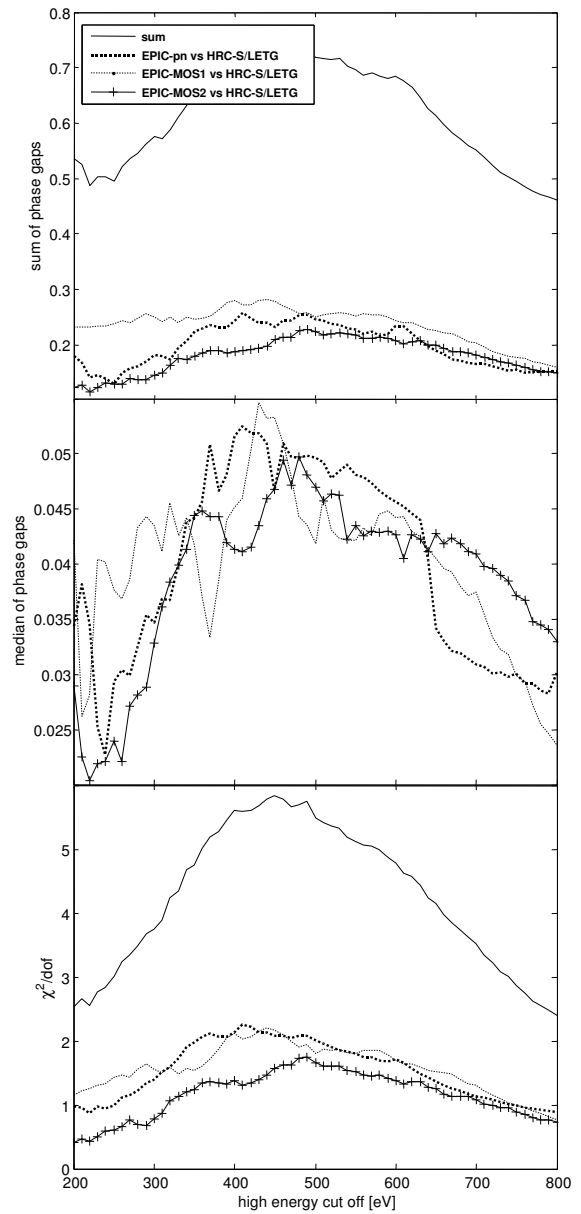


Figure 3.4: The same as in figure 3.3, but using the soft band (120 eV–cut off energy) for the analysis.

3. PULSAR TIMING

from 200 eV to 800 eV in steps of 10 eV. For example, if the band cut is at 600 eV, there are two bands of 120 – 600 eV and 600 – 1000 eV. Due to the limited energy resolution, these band cuts could not be applied for the HRC observations.

Then, the phase residuals were calculated according to equation 3.4 by fitting a sine (see [129]) to the phase folded light curves (12 phase bins) for pn, MOS1 and MOS2 and HRC for each band cut. Afterwards, the sum of the absolute values and the median of the phase gaps of the phase residuals of the harder band from the different detectors were calculated. Having the phase residuals and their errors, $\chi^2/d.o.f$ was calculated showing the degree of accordance of the results from the different detectors. In all three cases, a minimum (i.e. best agreement) was reached when choosing a band cut between 300 eV and 400 eV, i.e. having two bands of 120 – 400 eV and 400 – 1000 eV (figure 3.3) and using the harder band.¹ For band cuts of lower energies the different detector responses for the soft photons cause larger phase gaps owing to the phase shift between hard and soft photons and the rough energy resolution of the EPIC detectors, while for band cuts at higher energies the number of photons decreases and the statistics worsens.

If the same was done, but keeping the soft band photons (see figure 3.4), the best agreement of the different instruments was achieved if no band cut was applied (as done for previous timing solutions, e.g. [19; 63; 129; 151]). But even the lowest $\chi^2/d.o.f$ value was more than two times larger than in the case when photons between 400 – 1000 eV were used.

The choice of the hard band (400 – 1000 eV) reduces instrumental discrepancies of the different detectors as much as possible.

¹For consistency with previous work [41; 43; 51], the cut-off energy is set to 400 eV.

4

Results

4.1 Spectral properties

4.1.1 EPIC-pn

As can be seen from figure 1.4, the spectral properties of RX J0720.4–3125 follow a sinusoidal trend until 2005. The further development was investigated by reducing and analysing the new data obtained from XMM-Newton.

In [41; 43; 51] the EPIC-pn spectra were fitted using *Xspec* with the model $phabs \times (bbodyrad + gaussian)$, where “gaussian” represents the broad absorption feature (allowing negative normalisation) seen in the spectra and “bbodyrad” the emission of a perfect black body emitting at a certain temperature with a normalisation factor to calculate the size of the emitting area (scaled to a distance, here and in [41; 43; 51] always 300 pc). The spectrum is attenuated by absorption due to the interstellar medium (ISM), which is modeled using “phabs”. To avoid systematic errors due to cross-calibration problems, only EPIC-pn data obtained in full frame mode with thin filter were considered. The fit model is listed in detail in table 4.1. Since this model was used previously in [41; 43; 51] it is called the “standard model” in this work.

Xspec provides a number of models simulating the emission of neutron stars (e.g. “nsa”¹, “nsgrav”², “nsatmos”³), but none of them fits the data ($\chi^2/d.o.f. \geq 2.5$). Adding another component to the standard fit model did not improve the fit significantly. Therefore, the standard fit model was used only.

The 13 EPIC-pn spectra in full frame mode and thin filter were fitted in one session with the parameters N_H , E_{line} , σ_{line} left linked. In principle, these parameters could change

¹neutron star atmosphere: models a neutron star with a hydrogen atmosphere in a fixed magnetic field. The magnetic field strength can be set to 0 Gauss, $B = 10^{10}$ Gauss and $B = 10^{13}$ Gauss maximum, see [157] and [98].

²Neutron star with nonmagnetic hydrogen atmosphere and variable surface gravity, see [157].

³Neutron star with hydrogen atmosphere with electron conduction and self-irradiation, see [45].

4. RESULTS

with time, but it would not influence the main result, as shown later. The black body temperature (and normalisation) and the line normalisation are left free for each individual spectrum, since they are known to vary. Instead of the line normalisation, a more common measure of the strength of a spectral feature is the equivalent width (EW), that is used further on.¹

After including the new data (revolution 1181, 1265, 1356, 1454, 1700 and 1792, see table 2.2), the spectral properties of RX J0720.4–3125 clearly do not continue to follow a sinusoidal trend further but seem to undergo a relatively fast rise around $MJD = 52800$ days followed by a slow relaxation. To avoid cross-calibration problems as error sources, the EPIC-pn observations in other instrument setups were fitted separately, however the spectral properties follow well the trend seen in the observations performed in full frame mode with thin filter.

The values of the parameters which are common to all spectra are (errors denote 90% confidence):

- $N_H = 1.040 \pm 0.035 \times 10^{20}/\text{cm}^2$
- $E_{line} = 302.1 \pm 4.6 \text{ eV}$
- $\sigma_{line} = 76.3 \pm 3.3 \text{ eV}$

and are fully consistent with previous values [41]. Fitting these 13 EPIC-pn spectra in one session yields $\chi^2/d.o.f = 1.28$. To test the robustness of the fit results, the fits were performed in different ways: the E_{line} and the N_H value were allowed to vary with time (i.e. for each spectrum individually). If the line energy E_{line} was not fixed, it showed the same trend as the temperature: a jump around $MJD = 52800$ days (from 150 eV to 250 eV) followed by a slow decrease, while N_H followed the trend of the size of the emitting area and equivalent width and decreased from $1.1 \cdot 10^{20}/\text{cm}^2$ to $0.48 \cdot 10^{20}/\text{cm}^2$. However, the N_H value and E_{line} are strongly coupled. A change in the line energy can be compensated for by a variation of the N_H value. In addition, this approach causes larger error bars since the data are not sufficient to fit too many free parameters. In any case, the behaviour of the spectral variations in temperature, equivalent width and size of the emitting area is not significantly influenced using these different variances or the standard fitting procedure used in [41] and in this work, but a temporal change of E_{line} and/or N_H cannot be excluded. The trends of the temperature, equivalent width and size of the emitting area are illustrated in figure 4.1 and table 4.2 and the EPIC-pn (full frame mode and thin filter) spectra of RX J0720.4–3125 are shown in figure 4.2. The spectral properties obtained from the

¹If I_0 is the intensity of the continuum, the equivalent width is given with $EW(\lambda) = \int (1 - I(\lambda)/I_0) d\lambda$.

Table 4.1: The standard fit model $phabs \times (bbodyrad + gaussian)$ used for the RX J0720.4–3125 spectra in this and previous [41; 43; 51] works.

component	parameter	unit
1 phabs	column density N_H	$10^{22}/\text{cm}^2$
2 bbodyrad	temperature kT	keV
	normalisation	$(\text{km}/10 \text{ kpc})^2$
3 gaussian	line energy E_{line}	keV
	line width σ	keV
	normalisation	photons/s/cm ²

Table 4.2: Spectral changes of the phase averaged EPIC-pn spectra of RX J0720.4–3125 (see also figure 4.1). All observations are performed in full frame mode and with thin filter, unless written in *italic* (in other instrument setups, see table 2.2). The errors denote the 90% confidence interval.

orbit	MJD [days]	EW [eV]	kT [eV]	radius [km]
0078	51678	$-4.1^{+4.0}_{-3.8}$	86.5 ± 0.4	4.80 ± 0.09
<i>0175</i>	<i>51870</i>	$+5.6^{+3.5}_{-3.5}$	86.0 ± 0.7	4.90 ± 0.14
0533	52585	$-13.6^{+4.8}_{-4.6}$	88.7 ± 0.5	4.64 ± 0.10
0534	52587	$-19.7^{+4.6}_{-4.3}$	88.1 ± 0.5	4.71 ± 0.10
<i>0711</i>	<i>52940</i>	$-67.7^{+2.7}_{-2.7}$	92.0 ± 0.6	–
0815	53148	$-58.1^{+4.3}_{-3.9}$	94.7 ± 0.5	4.28 ± 0.08
0986	53489	$-57.2^{+3.9}_{-3.5}$	94.4 ± 0.4	4.34 ± 0.07
1060	53636	$-54.5^{+3.9}_{-3.5}$	93.8 ± 0.4	4.36 ± 0.07
1086	53687	$-55.3^{+3.9}_{-3.5}$	93.1 ± 0.4	4.49 ± 0.08
1181	53877	$-50.7^{+4.9}_{-4.5}$	93.1 ± 0.6	4.43 ± 0.10
1265	54045	$-53.0^{+4.8}_{-4.4}$	92.7 ± 0.6	4.52 ± 0.11
1356	54226	$-43.6^{+5.0}_{-4.7}$	92.4 ± 0.6	4.44 ± 0.10
1454	54421	$-44.1^{+4.7}_{-4.4}$	91.9 ± 0.6	4.49 ± 0.10
1700	54912	$-44.8^{+5.1}_{-4.8}$	91.9 ± 0.6	4.51 ± 0.11
1792	55096	$-38.3^{+5.6}_{-5.2}$	91.3 ± 0.7	4.51 ± 0.12

observation performed during revolution 0622 is not listed in table 4.2, since the thick filter was used, which strongly reduces the number of events at lowest energies.

4.1.2 EPIC-MOS and RGS

In addition to the pn data, the MOS1 and MOS2 and the RGS1 and RGS2 data were investigated. Since the MOS detectors are less sensitive in the soft band [125], only photons above 400 eV could be used for the spectral fitting. For this reason, the information of the broad absorption feature ($E_{line} = 302.1 \pm 4.6$ eV) is lost and no conclusions could be derived. The values for the temperatures have errors ≈ 3 eV (90% confidence), i.e. are too large to see a clear variation. Moreover, the instrument setups for the MOS

4. RESULTS

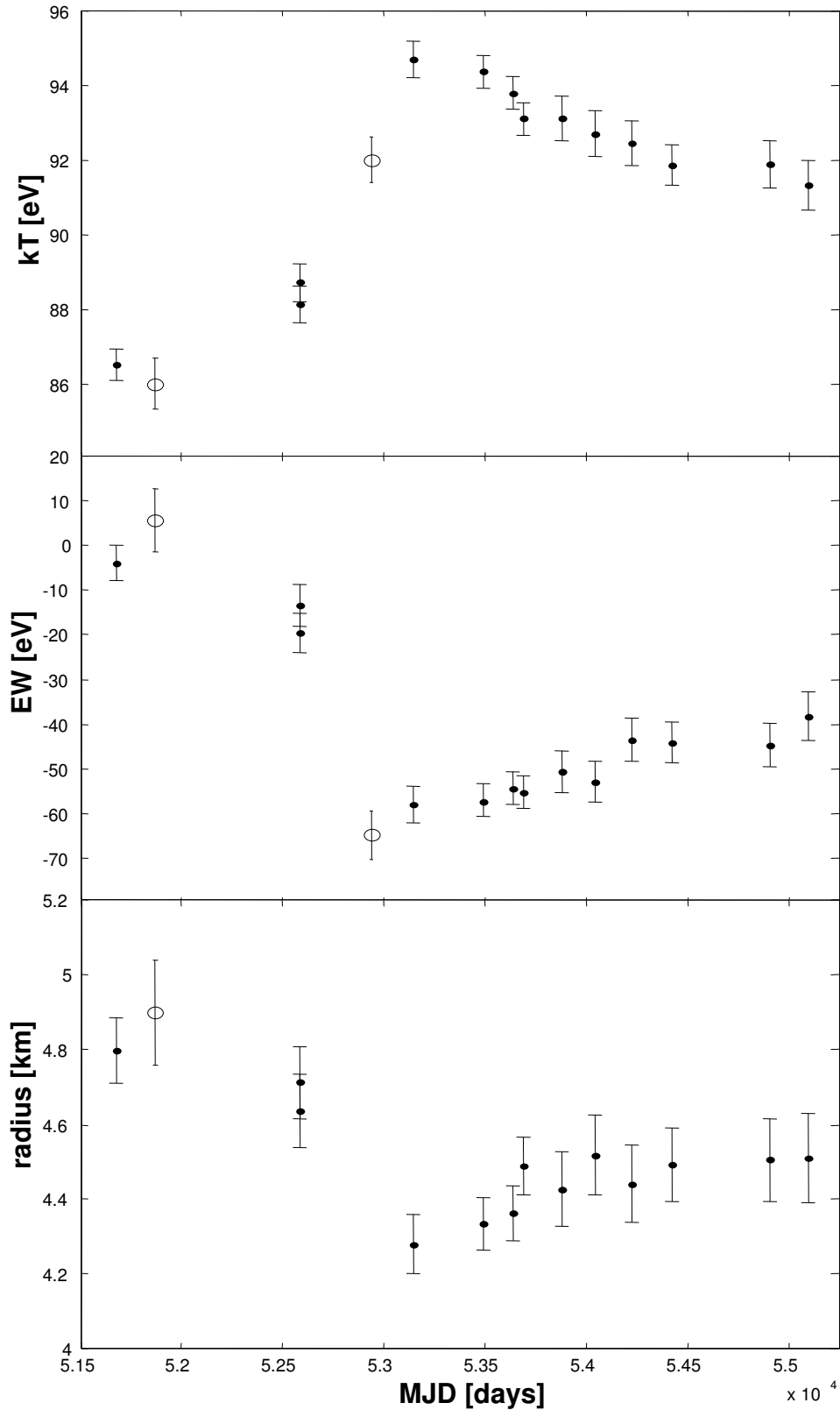


Figure 4.1: Long term variations of the pulse phase averaged spectra of RX J0720.4–3125 obtained from the 13 EPIC-pn observations in full frame mode with thin filter (dots). Open circles show data obtained from the other EPIC-pn observations (see table 2.2). Error bars denote 90% confidence level.

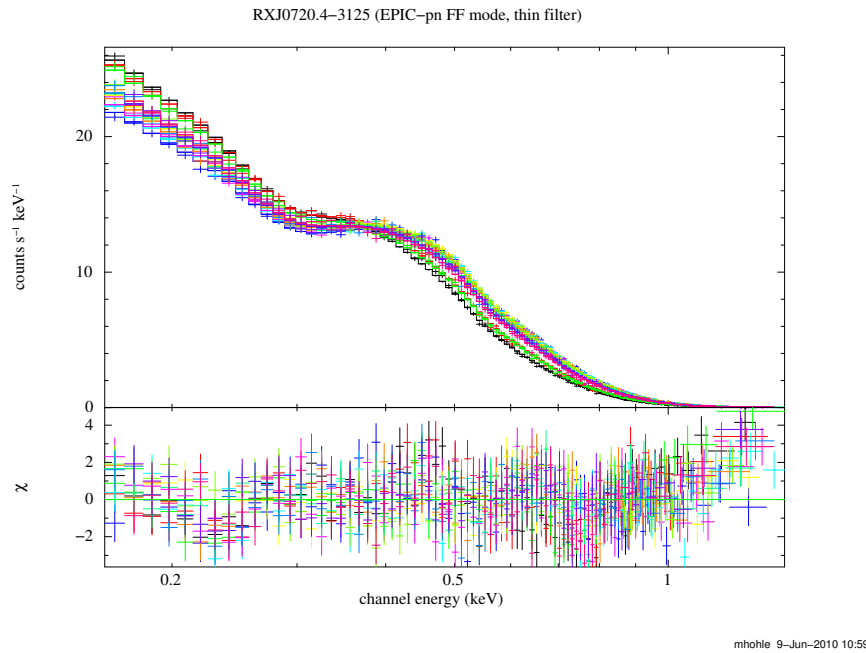


Figure 4.2: All XMM-Newton EPIC-pn spectra of RX J0720.4–3125 performed in full frame mode with thin filter. The spectra are fitted with the standard fit model [41; 43; 51], see table 4.1.

detectors vary much more than for pn (see table 2.2), i.e. prevents direct comparison of the different temperatures, so that only three or four observations (not necessarily contiguous) are directly comparable. Moreover, the MOS detector response changes with time that introduces another source for systematic uncertainties.

In the case of RGS1 and RGS2, only photons above 350 eV could be used, i.e. again it was not possible to derive the values for the equivalent width of the broad absorption feature. The spectral resolution of the two RGS is much better than for EPIC (see [23] and section 2.2). Due to the lower sensitivity, the RGS data were co-added by [44] using *rgscombine* only allowing to investigate a total average spectrum, but with high energy resolution. A narrow absorption feature ($EW = -1.35 \pm 0.30$ eV) around 0.57 keV was found in the total spectrum.

Since the work of [44], three new XMM-Newton observations were performed (see table 2.2) that improve statistics. The new RGS observations were co-added in the same way as described in [44]. Only first orders were considered, since the second orders are weak. The RGS2 detector does not provide spectral information in the required energy band (see figure 2.3), thus could not be used. In total, the exposure time sums up to 600 ks (50 ks more than in [44]).

First, the standard fit model (table 4.1) was applied to the co-added RGS spectrum, then the parameters listed in table 4.1 were kept fixed and a further Gaussian absorption feature

4. RESULTS

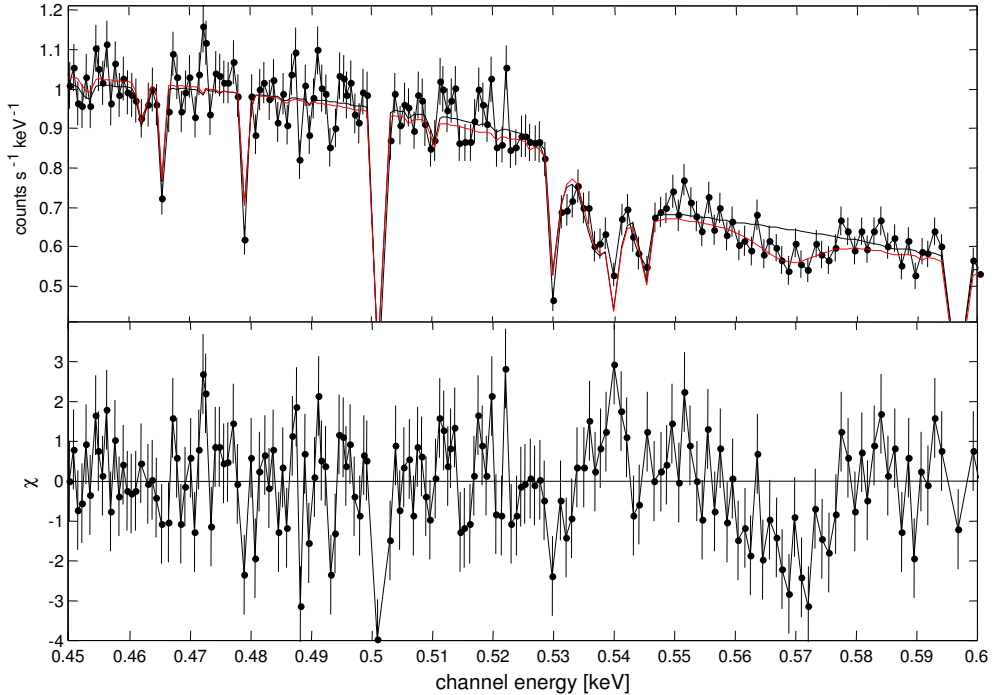


Figure 4.3: The co-added RGS1 (first order only) spectrum of RX J0720.4–3125 in the upper panel with a total exposure of 600 ks. The black line represents the fit from the standard model (see table 4.1), while the red line shows the standard fit model plus a narrow absorption feature seen at 0.5692 ± 0.0022 keV with $EW = -1.055^{+0.106}_{-0.042}$ eV (errors denote 90% confidence level), see also [44] for comparison. The fit residuals from the standard fit are shown in the lower panel.

(representing the narrow absorption line) was included. Including the recent XMM-Newton observations, the line was confirmed at 0.5692 ± 0.0022 keV with $EW = -1.055^{+0.106}_{-0.042}$ eV and $\sigma = 3.5 \pm 1.8$ eV (errors denote 90% confidence level), see figure 4.3. The influence of the line on the quality of the spectral fit is negligible: applying the standard model, the fit yields $\chi^2/d.o.f. = 1.17$, including the narrow absorption feature, $\chi^2/d.o.f.$ decreases to 1.16. Though, since there are no detector features in this energy range, the line detection seems reliable. However, an absorption line around 0.48 keV, as claimed by [44], could not be confirmed.

4.1.3 Chandra HRC-S/LETG

To verify the spectral changes of RX J0720.4–3125 detected with EPIC-pn the Chandra HRC-S/LETG spectra performed close in time to each other (see table 2.3) were merged to improve the statistics. This results in nine individual (merged) spectra. The HRC-S/LETG spectra were added using the CIAO command *add grating orders* to add the two first orders (all other orders have a negligible count number) and *add grating spectra* to add the HRC-

S/LETG spectra. The fit procedure followed that for EPIC-pn using the standard fit model in *Xspec12*.

Although the errors for the temperatures were again larger than for EPIC-pn data, the temperature could be derived from nine observations performed in the same instrument setup. The temperature variations clearly do not follow a sine for the observations performed after 2005 ($MJD = 53700$ days), see figure 4.4. The different spectra are shown in figure 4.5. Due to the lack of counts compared to the EPIC-pn data, it was not possible to obtain reliable estimates for the variable values of the equivalent width (of the broad absorption line at 0.3 keV) and sizes of the emitting area, since the resulting errors are too large. The values of the parameters which are common to all spectra are (errors denote 90% confidence):

- $N_H = 0.67 \pm 0.13 \times 10^{20}/\text{cm}^2$
- $E_{line} = 258 \pm 40$ eV
- $\sigma_{line} = 67 \pm 25$ eV

The nine spectra fitted in one session yield $\chi^2/d.o.f = 0.54$. Formally, N_H derived from the Chandra HRC-S/LETG spectra is not consistent with the value obtained from EPIC-pn. This deviation is caused by the lower value of $E_{line} = 258 \pm 40$ eV compared to the value obtained with the XMM-Newton EPIC-pn spectra ($E_{line} = 302.1 \pm 4.6$ eV), although they are consistent. As a result, N_H has a lower value as well, since N_H and E_{line} are strongly coupled, as discussed previously.

From the results of the co-added RGS spectra it was obvious to take the next step and co-add all Chandra HRC-S/LETG spectra. Altogether, the co-added HRC-S/LETG spectra have 450 ks exposure time (see table 2.3). After fitting the final average spectrum with *Xspec12* using the standard fit model, the following results were obtained (errors denote the 90% confidence interval):

- $N_H = 0.857 \pm 0.090 \times 10^{20}/\text{cm}^2$
- $E_{line} = 255 \pm 32$ eV
- $\sigma_{line} = 76 \pm 23$ eV
- $kT_{aver} = 92.0 \pm 1.4$ eV
- $R_{aver} = 4.8 \pm 1.6$ km
- $EW_{aver} = -39_{-19}^{+10}$ eV.

4. RESULTS

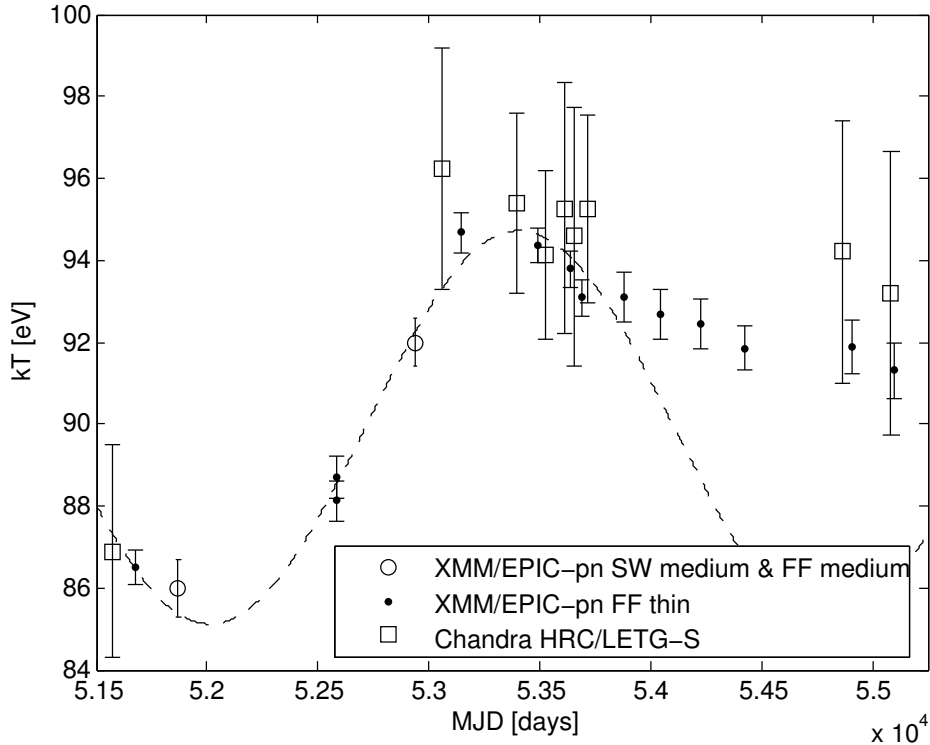


Figure 4.4: The temperature evolution of RX J0720.4–3125 including the most recent XMM-Newton and Chandra observations. The Chandra spectra were merged according to the tags in table 2.3. The dashed curve represents the sine fit in [41] and figure 1.4 that is not consistent with the new observations. All spectra are fitted with the standard model, see [41; 43; 51] and table 4.1.

with $\chi^2/d.o.f = 1.08$.

Now, N_H is in better agreement with the value derived from the EPIC-pn spectra, but still not consistent with it.

In addition to the narrow absorption feature found by [44], two other lines that seem to be even more significant with respect to the continuum, were detected. Since all three lines are rather weak, for a cross-check Chandra pipeline products were used as well as reprocessed data for the co-added spectrum together with two different *Xspec* absorption models (*phabs* and *tbabs*) for the ISM. In all cases, the lines were present, see figure 4.6. To fit the lines, the parameters from the standard model were fixed and a Gaussian absorption line (representing the narrow absorption feature) was added and fitted, then all parameters were set free and fitted again. The parameters of the three lines are listed in table 4.3. Like for the co-added RGS1 spectra, the inclusion of the new absorption lines did not significantly improve the fit, since the features are weak and the value of $\chi^2/d.o.f.$ is dominated by the rest of the spectrum. $\chi^2/d.o.f.$ from the co-added HRC-S/LETG spectra decreased from 1.08 to 1.03.

To ensure that the new detected lines are not uncalibrated instrumental features, all avail-

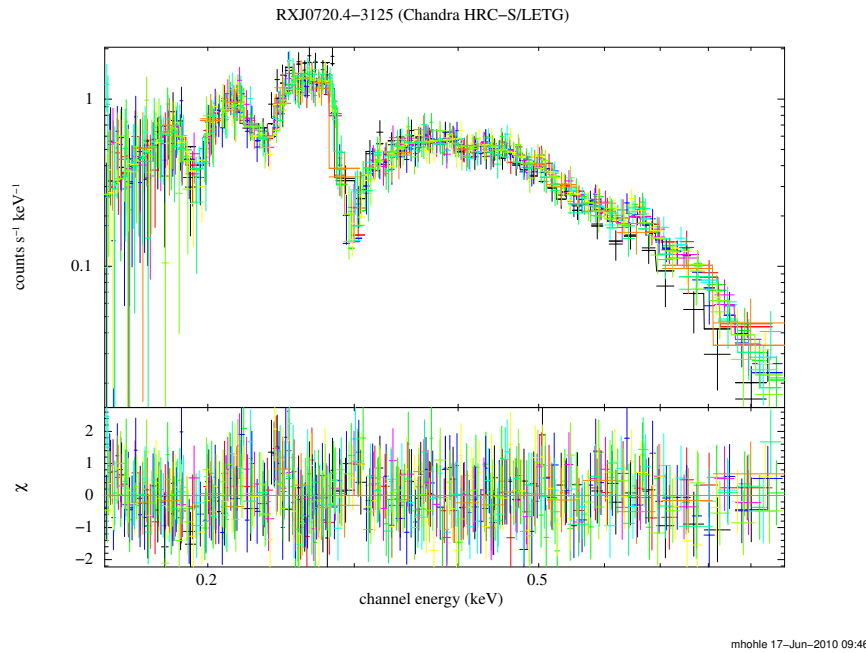


Figure 4.5: The Chandra HRC-S/LETG spectra of RX J0720.4–3125, merged according to the tags in table 2.3. All spectra are fitted with the standard model, see [41; 43; 51] and table 4.1.

able HRC-S/LETG spectra of RX J1856.4–3754 were co-added for comparison. No significant spectral features were found so far from RX J1856.4–3754 [15; 16]. The co-added HRC-S/LETG spectrum of RX J1856.4–3754 (500 ks total exposure time) was fitted in *Xspec* with a single black body absorbed by the ISM (model *phabs*). Indeed, the three absorption lines found in the spectrum of RX J0720.4–3125 are not present in the spectrum of RX J1856.4–3754 (illustrated by the fit residuals in figure 4.7) that has much better statistics.

Intriguingly, the absorption line found at 0.48 keV fits to the OVII K_{α} resonance line having a redshift of 1.17, as claimed in [44]. An absorption feature at 0.65 keV (OVIII at rest, see [44]) remains undetected, probably due to the lack of photons in this energy range. However, the absorption feature at 0.53 keV is hard to reconcile with highly ionised oxygen, either at rest or with a gravitational redshift of 1.17. More likely, this absorption feature originates from neutral oxygen in the ISM since it is close to the K-edge with strong sub-edges at 0.538 keV, see the discussion in [60], section 4.1.3. therein. Thus, this feature might be a result of inexact modeling of the edge or indicates an overabundance of oxygen in the direction of RX J0720.4–3125.

The interpretation of the three absorption features merits more investigations in the future and the presence of such lines should also be checked for the other M7 as well.

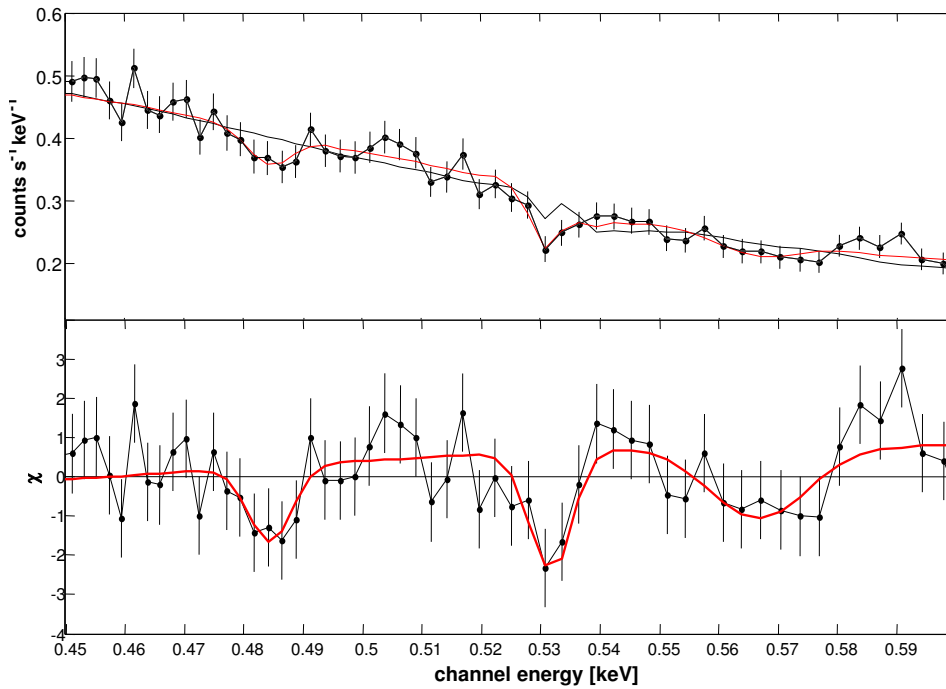


Figure 4.6: The same as in figure 4.3, but obtained from the co-added HRC-S/LETG spectrum of RX J0720.4–3125. The three narrow absorption features at 0.48, 0.53 and 0.57 keV (see also table 4.3) are much better seen in the fit residuals (lower panel) than in the spectrum itself (upper panel).

Table 4.3: The three narrow absorption features of RX J0720.4–3125 detected in the co-added Chandra HRC-S/LETG spectra. The third line corresponds to the absorption feature found by [44] in the XMM-Newton RGS data, the other two lines were undetected before. All errors denote 90% confidence level.

energy [keV]	wavelength [Å]	σ [eV]	EW [eV]
0.4842 ± 0.0017	$25.606^{+0.090}_{-0.090}$	4.5 ± 1.8	$-1.52^{+0.25}_{-0.43}$
0.5313 ± 0.0012	$23.336^{+0.053}_{-0.053}$	3.8 ± 1.3	$-2.10^{+0.11}_{-1.20}$
0.5663 ± 0.0031	$21.890^{+0.240}_{-0.120}$	8.2 ± 3.4	$-2.78^{+0.10}_{-1.48}$

4.2 Timing

4.2.1 Individual periods, light curves and phase determination

As described previously, the available XMM-Newton and Chandra ACIS-CC observations were divided into hard and soft photons and those Chandra observations close in time were merged into one data set (see table 2.3). After this merging 71 data sets were obtained: 16 from XMM-Newton EPIC-pn and 36 from EPIC-MOS1/MOS2 (the XMM-Newton observations revolution 0622 and 0711 from May and October 2003, respectively,

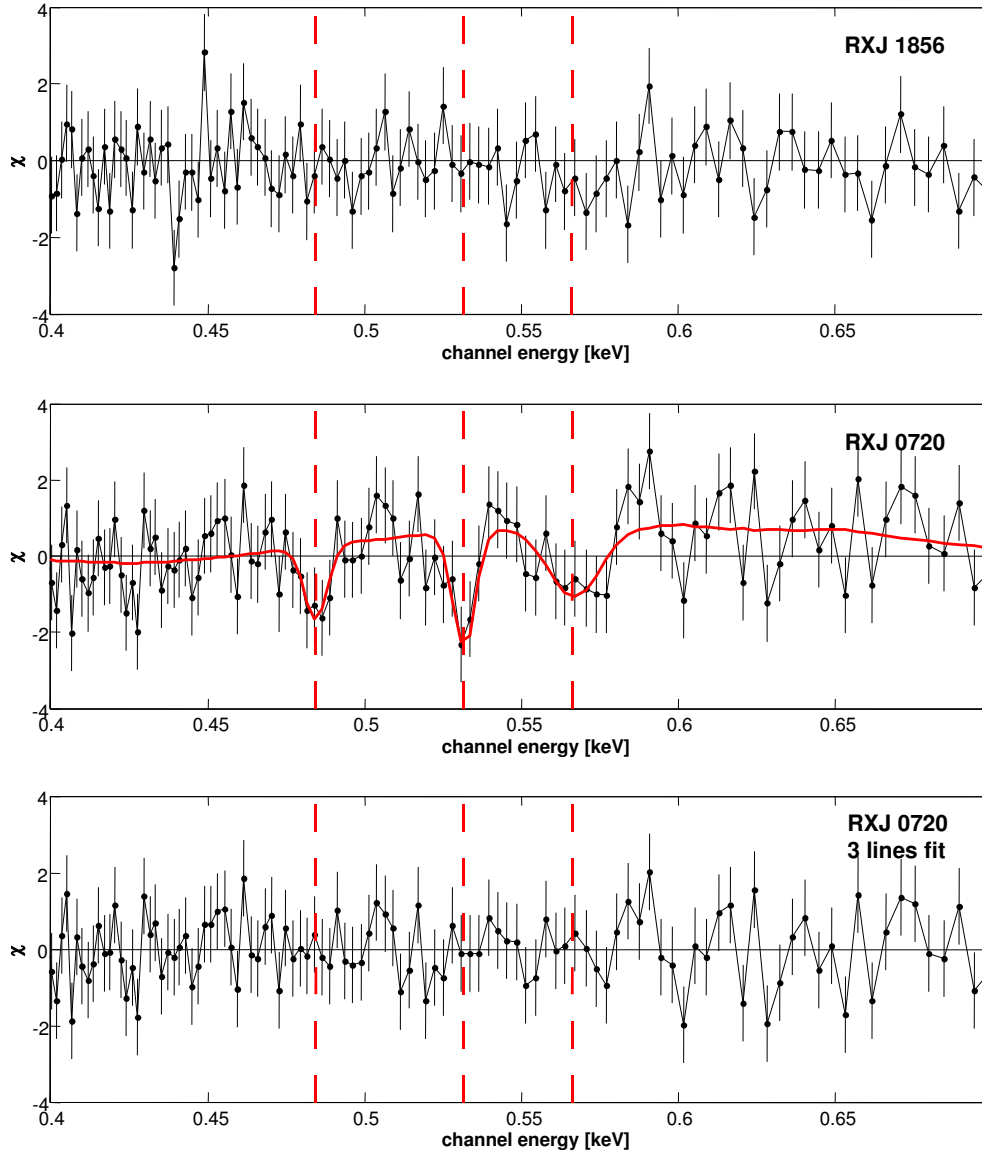


Figure 4.7: The fit residuals from the co-added HRC-S/LETG spectra of RX J1856.4–3754 (upper panel) after applying the black body model [15; 16] and from the co-added HRC-S/LETG spectra of RX J0720.4–3125 (middle panel) after applying the standard model, see [41; 43; 51] and table 4.1. The locations of the narrow absorption features (not seen in the residuals of the spectra of RX J1856.4–3754) are marked with the dashed red lines and the fitted Gaussian absorption lines are indicated with a red solid line. The fit residuals vanish after the inclusion of three absorption lines (bottom).

have four MOS data sets each), 6 ROSAT data sets (pointings only) and 13 (merged from 29) data sets from Chandra observations.

To use a data set for timing, the photon arrival times have to be folded into phase, thus the correct period has to be detected. If the periodogram is populated by equally dominant aliases, the phase folding is ambiguous and such observations have to be taken with care, thus in a first step the period was determined using the Z_1^2 test for each of the 71 data

4. RESULTS

sets individually (errors are calculated using the approach in [110]). Since the ROSAT data have a low count number, these observations yield large period errors and show aliases, hence were excluded for the first timing solution. For the observations with more than $\approx 10^4$ photons, the period determination becomes more certain (see table A.1). Most of the individual periods are consistent with the single spin-down model within 1σ errors and all of them are consistent within 2σ errors, see figure 4.8. The period of the Chandra HRC-S/LETG observation 7251 shows a large discrepancy with respect to the other observations (see table A.1), probably caused by the small number of photons giving not enough statistics for a reliable period determination. Unfortunately, this observation is not close in time to the other Chandra HRC-S/LETG observations and could not be merged. Like the ROSAT data, this observation was excluded as well, i.e. finally 64 observations were used.

In previous works [63; 129], the phase folded light curves of RX J0720.4–3125 were fitted with a sinusoid, however it is known [43] that the light curves are not best represented by a sine function and generally exhibit a more complicated shape [109] depending on emission geometry. Indeed, the Fourier coefficients of the light curves provide information about the size and the location of the emitting area – a pure sine is only a special case. To take this into account and to derive a more accurate phase determination, the light curves were fitted using a combination of three Fourier harmonics:

$$F(\phi) = \sum_{k=0}^3 A_k \sin(k\phi) + B_k \cos(k\phi) \quad (4.1)$$

where $k = 0$ corresponds to the constant offset. In the following, each term is denoted as $\sin k$ or $\cos k$, e.g. $\sin 1$ abbreviates $A_1 \sin(1\phi)$, $\cos 1$ abbreviates $B_1 \cos(1\phi)$. The contribution of $\cos 1$ is negligible (the phase is zero at the reference time, and a cosine term would imply a phase shift), the sum in equation 4.1 starts always with $\sin 1$, while the remaining two terms can be $\sin 2 + \sin 3$, $\cos 2 + \sin 3$ or $\cos 2 + \sin 2$, and so on. The light curves were fitted with the sum of three terms, not to introduce too many fit parameters, and terms with $k > 3$ were not used, i.e. only three terms in total. The combination that fits the individual light curve with the lowest value of $\chi^2/d.o.f.$ was used for the phase determination.

In [63], the reference point for the phase to be zero and the initial period was taken from the combined Chandra ACIS-CC observations 4666 to 4669 with the HRC observation 5305, covering a total time span of 52 days. This dataset produces aliases in the periodogram caused by the time gaps between the observations. Three peaks with $Z_1^2 \approx 140$ were detected: $P_1 = 8.39036664(53)$ s, $P_2 = 8.39111600(50)$ s and $P_3 = 8.39188114(53)$ s. P_2 yields formally the largest Z_1^2 value and is consistent with the reference period $P = 8.39111590(50)$ s from [63] (numbers in parentheses indicate 1σ errors using the error

estimation in [110]).

The other observations were sorted with increasing time, taking as reference time that of [63] (“all data” solution). In principle, the ACIS-CC observations 4670 to 4673 combined with the HRC observation 5581 could as well be used as starting point. However, the time gap to the observation 5581 is too large and the period determined from the ACIS-CC observations 4670 to 4673 is not accurate enough to keep the phase cycles.

Based on the reference period, the phase of the maximum in the phase binned light curve was calculated fitting the Fourier series (equation 4.1) from the reference observation and from the observation next to it in time. Then, the period is varied within its errors in order to minimise the phase difference, assuming that the period in these observations is not changing and the next observation was added. Assuming an initial guess for \dot{f} in the range between -15 and -5×10^{-16} Hz/s, the change in the period due to the secular spin-down becomes comparable to the period error after 150 days from the reference time. Then the period and \dot{f} were varied within their errors in order to minimise the sum of the squared phase residuals weighted by their errors from the light curve fit. The next observation was then added and the whole procedure was repeated, finding new values of the period and \dot{f} . The period error decreases with the growing time span to the reference point following the general approach in [72], while the error of \dot{f} is calculated from the different values of \dot{f} obtained by varying the phase residuals within their 1σ errors during this iterative procedure.

The convergence of the timing parameters is illustrated in figure 4.9. If a different initial period is chosen (e.g. P_1 or P_3), the phase residuals are small around the reference point, but grow with larger time distance and finally scatter arbitrarily between 0.5 and -0.5 .

Determining the phase residuals with the Fourier series leads to an improvement of the $\chi^2/d.o.f.$ for the light curves (see for example figure 4.10) and to a better determination of the phase shift. The phase of the maximum light delivers the time of the maximum light closest to the middle of the observation, the time of arrival (TOA), see [63; 129]. Fitting the light curves with only three Fourier harmonics is justified since in most of the cases some Fourier coefficients are negligible (see the coefficients from the phase folded light curves of the EPIC-pn observations in figure 4.11 as an example). The temporal evolution of the Fourier coefficients indicates the substantial change of the light curves (see also [52]), i.e. of the observed geometry of the emission [109], as already reported in [22; 41].

4.2.2 Timing solutions

The phase coherent timing was performed by binning the light curves into 10, 12, 16, 18 and 20 phase bins. In [63; 129] the light curves of RX J0720.4–3125 were folded into 16 phase bins, also for the MOS data. If the number of phase bins is large, the light curves

4. RESULTS

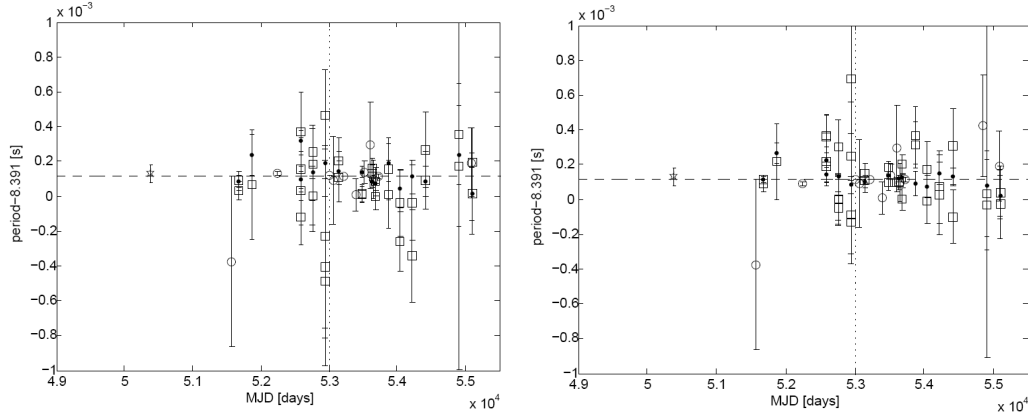


Figure 4.8: Left: Individual periods from observations with more than 10^4 photons. The error bars denote the 1σ uncertainty, see [110]. Squares mark periods derived from XMM-Newton EPIC-MOS1 and MOS2 observations (hard band), dots EPIC-pn observations (hard band), circles Chandra HRC-S/LETG and ACIS-CC data (hard band) and stars ROSAT data. The vertical dotted line shows the reference time given in [129] (“all data” solution) and the horizontal dashed line indicates the period evolution derived from the “all data” solution in [129].

Right: The same as left but using the soft band for EPIC-MOS1 and MOS2, EPIC-pn and ACIS-CC data.

Table 4.4: Period and \dot{f} derived from different methods in this work, compared to previous results. For the timing solution in this work, the Chandra HRC observation 7251 was always excluded. All errors correspond to 1σ confidence (for the Z_1^2 solution see [110] with errors scaled to $\sqrt{\chi^2/d.o.f.}$).

solution	$period - 8.391115$ $\times 10^{-7}$ [s]	\dot{f} $\times 10^{-16}$ [Hz/s]	rms [s]	$d.o.f$	$\chi^2/d.o.f$
this work, hard band					
“all data”	3.336(22)	-9.961(67)	0.62	70 - 3	45
without ROSAT	3.362(39)	-9.946(74)	0.60	64 - 3	47
without Chandra	3.310(22)	-9.940(71)	0.61	58 - 3	47
Z_1^2 “all data”	3.09(14)	-9.992(61)	0.73	70 - 3	64
Z_1^2 without ROSAT	2.96(13)	-10.047(34)	0.58	64 - 3	46
Z_1^2 without Chandra	3.09(13)	-9.980(36)	0.72	58 - 3	51
this work, soft band					
“all data”	3.429(22)	-9.956(72)	0.50	70 - 3	40
Z_1^2 “all data”	3.31(62)	-9.959(17)	0.50	70 - 3	39
previous work (applied to the hard band)					
[129] (“all data”)	2.670(84)	-9.88(13)	0.97	70 - 3	81
[129] (without ROSAT)	2.846(77)	-9.74(04)	1.30	64 - 3	207
[63] (“all data”)	3.20(13)	-9.918(15)	0.64	70 - 3	56
[63] (Chandra)	3.05(16)	-9.97(06)	0.64	12 - 3	57

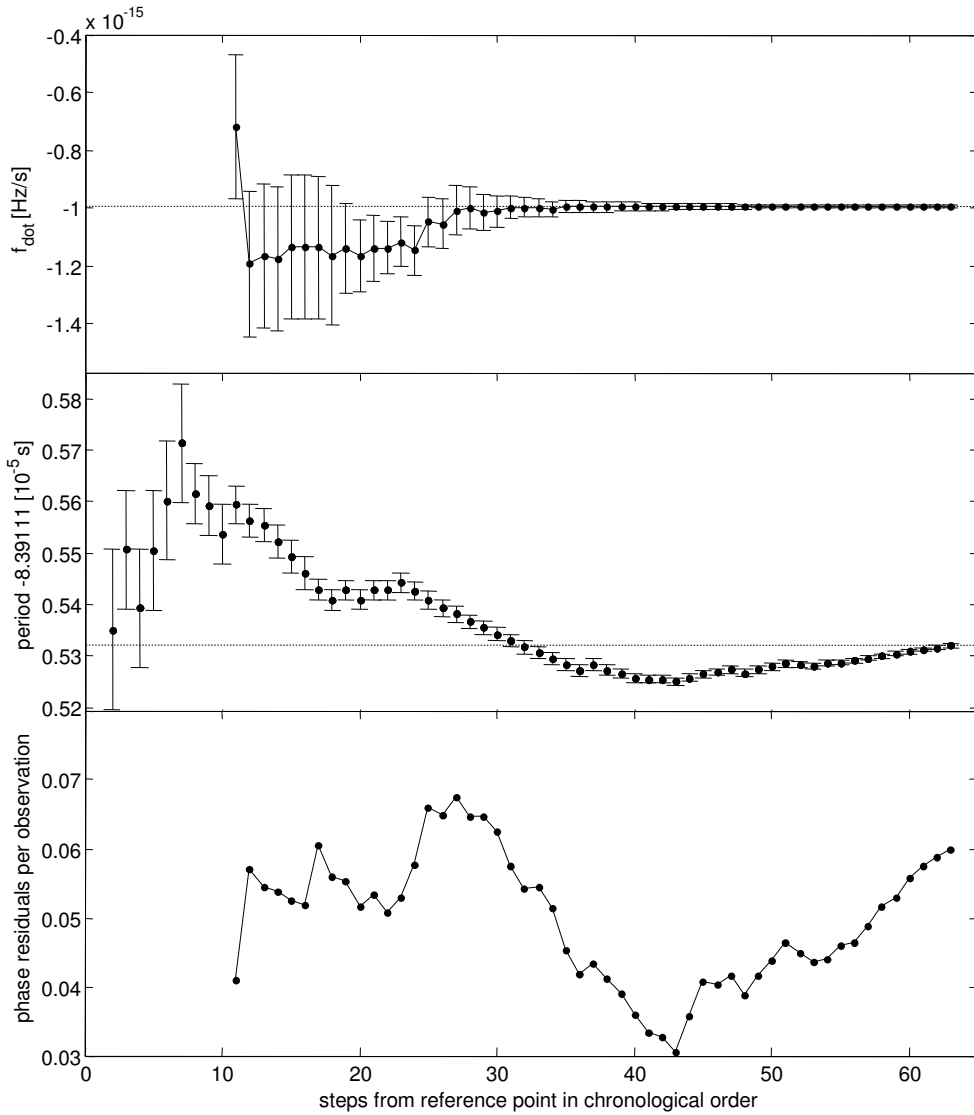


Figure 4.9: Evolution of \dot{f} (upper panel), period (middle) and phase residuals (lower panel) during the iterative process approaching the final timing solution (marked with dotted lines). The data is obtained from the timing solution without ROSAT data for the hard band. All errors denote 1σ .

in the Chandra data scatter due to the small count rate compared to XMM-Newton while too few bins result in an insufficient time resolution. The time resolution for the MOS detectors is 0.3 s (small window), 0.9 s (large window) and 2.6 s (full frame), i.e. less than one phase bin. This is compensated for by the large number of photons. The best timing solution regarding the lowest mean of the phase residuals for all observations (excluding ROSAT data and the HRC observation 7251) was derived for 12 phase bins.

Fitting the phase folded light curves with a pure sinusoid, the final values of the timing solution for the hard band are $P = 8.3911153307(22)$ s and $\dot{f} = -9.933(52) \times 10^{-16}$ Hz/s for the phase coherent timing solution. This corresponds to $\chi^2/d.o.f. = 12.7$ for the timing

4. RESULTS

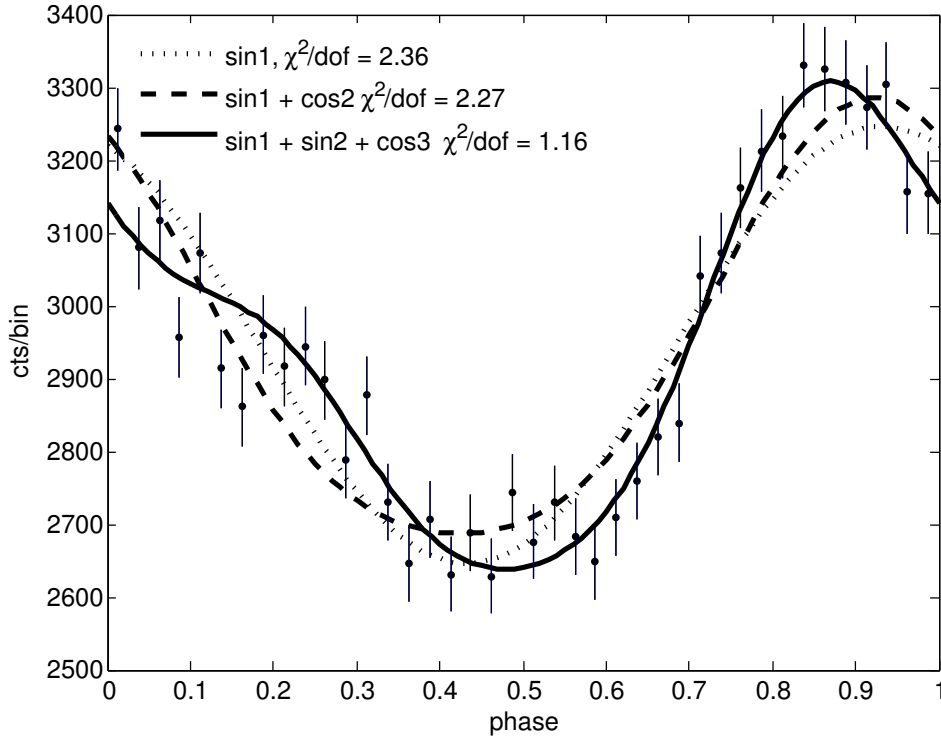


Figure 4.10: Phase binned (40 bins) light curve (400 – 1000 eV) of the XMM-Newton EPIC-pn observation revolution 1086 (November 2005) folded during the timing procedure. The solid line represents the combination of three Fourier harmonics chosen for the phase determination. The phase shift differs slightly from that of the sine fit (dotted line). The dashed line shows that fitting only with the second harmonic (cosine) is not always sufficient. The error bars denote Poissonian errors.

solution and for the individual light curve fits $\chi^2/d.o.f. = 2.29$ on average.

Fitting the light curves with a variable combination of the three Fourier harmonics, did not change the result significantly: $P = 8.3911153362(39)$ s and $\dot{f} = -9.946(74) \times 10^{-16}$ Hz/s; however the phase residuals have smaller errors (see e.g. figure 4.10) and therefore the timing solution automatically yields a larger value of $\chi^2/d.o.f. = 47$. The light curves fit with $\chi^2/d.o.f. = 1.23$ on average.

The periods determined from the ROSAT data [19; 151] differ significantly from the reference period P_2 (see table A.1) but inclusion of the ROSAT data (table 2.1) extends the time span of observations from ≈ 9.6 yrs to ≈ 16.5 yrs and enlarges the data set from 64 to 70 observations. The phase coherent timing solution (fitting the light curves with a variable combination of the three Fourier harmonics) including ROSAT data results in $P = 8.3911153336(22)$ s and $\dot{f} = -9.961(67) \times 10^{-16}$ Hz/s for 12 phase bins. This corresponds to $\chi^2/d.o.f. = 45$ for the timing solution and the light curves fit with $\chi^2/d.o.f. = 1.17$ on average.

When the Chandra data were excluded, but the ROSAT data were still used (58 data

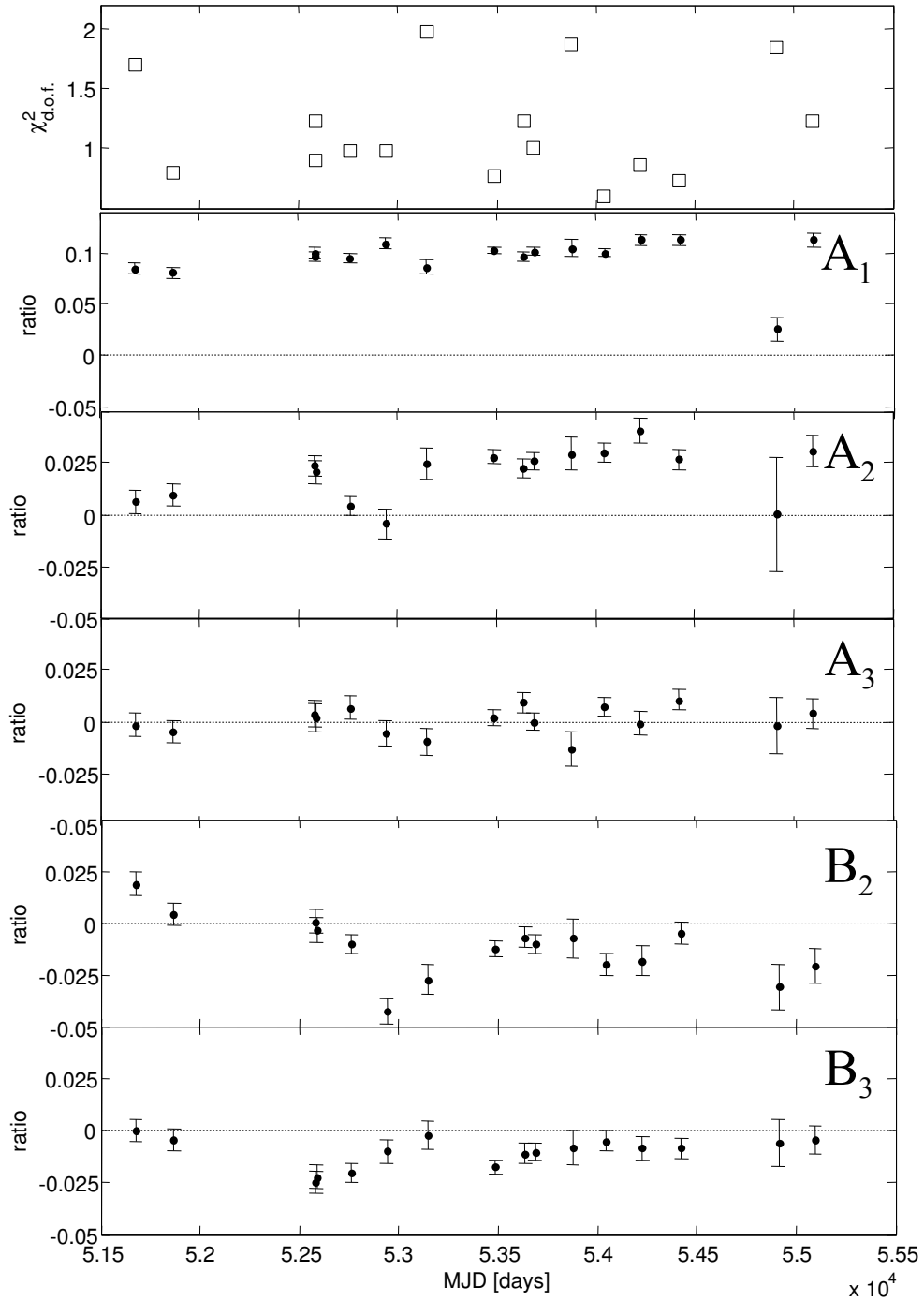


Figure 4.11: Fourier coefficients from the phase folded light curves of the 16 XMM-Newton EPIC-pn observations of RX J0720.4–3125. The designation of the coefficients follow that in equation 4.1.

sets out of 70) and the same reference time was chosen as before, the timing solution resulted in (again fitting the light curves with a combination of the first three Fourier harmonics) $P = 8.3911153310(22)$ s and $\dot{f} = -9.940(71) \times 10^{-16}$ Hz/s for 12 phase bins that corresponds to $\chi^2/d.o.f. = 47$ for the timing solution and for the light curve fits

4. RESULTS

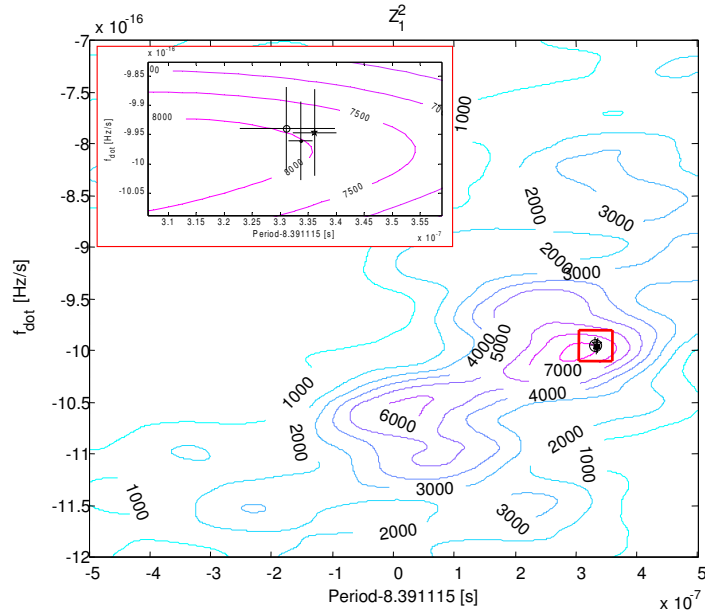


Figure 4.12: The Z_1^2 values in the $P - \dot{f}$ plane derived from the XMM-Newton, ROSAT and Chandra observations (excluding the HRC observation 7251) of RX J0720.4–3125 compared to the results of the phase coherent timing solutions in this work. The peak is located at $P = 8.391115309(14)$ s and $\dot{f} = -9.992(61) \times 10^{-16}$ Hz/s. The three different timing solutions derived without Chandra data (open circle), without ROSAT data (star) and using XMM-Newton, ROSAT and Chandra observations (dot) are not resolved on this scale (red box), but become visible enlarging the red box (shown in the upper left panel); the values are listed in table 4.4. The errors denote the formal 1σ uncertainty. All timing solutions are derived from the hard band (400 – 1000 eV).

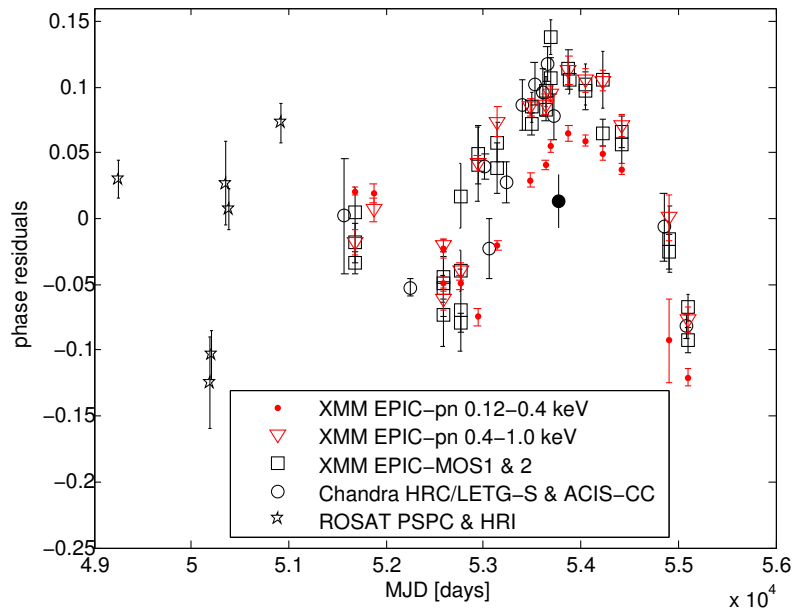


Figure 4.13: Phase residuals of RX J0720.4–3125 after applying the timing solution derived without the ROSAT observations and without the Chandra HRC observation 7251 (marked as a filled circle) applied to all observations.

$\chi^2/d.o.f. = 1.21$ was obtained on average.

To verify the correctness of the timing solutions, the Z_1^2 method was applied to the same combination of observations as for the phase coherent timing solutions. Using all 70 data sets, the maximum peak ($Z_1^2 = 8263$) is located at $P = 8.391115309(14)$ s and $\dot{f} = -9.992(61) \times 10^{-16}$ Hz/s, see figure 4.12. The errors of the period and \dot{f} are obtained from the equation in [110], where the values correspond to the maximum peak in the centre of the 1σ confidence region. In this region the peak is symmetric and the errors are scaled to $\sqrt{\chi^2/d.o.f.}$.

To show the difference of the timing solutions in the different bands, a phase coherent timing solution for the soft band (including all 70 data sets) was also performed. All results are listed in table 4.4.

After the new phase coherent timing solutions with constant spin-down were applied, the data of RX J0720.4–3125 still exhibit large phase residuals, see for example figure 4.13 in comparison to figure 1.6. Due to the Fourier series fitting, the errors of the phase residuals are smaller than previously (figure 1.6), since the light curves fit better. However, the smaller errors formally increase $\chi^2/d.o.f.$ of the timing solution. The trend of the phase residuals differs only slightly for the different timing solutions. Note the phase gap between the hard and the soft band of the XMM-Newton EPIC-pn data and the better accordance of the results from the hard band to the other instruments achieved by the band-cut at 400 eV, as shown in figure 4.13.

5

Discussion

In this chapter the results of this work are summarised and discussed to give an overview. The focus is put on the timing results. Two main explanations for the behaviour of RX J0720.4–3125 are competing: precession and the glitch hypothesis. However, in principle there are more explanations that appeared during the work and that will be discussed here as well. These further theories are examined for their advantages and disadvantages. For completeness and for comparison to previous works [41; 51], the results from phase resolved spectroscopy are discussed here as well.

5.1 Updated interpretation of the spectral and temporal variations of RX J0720.4–3125

5.1.1 Precession

Free precession of RX J0720.4–3125 was first proposed by [22] and more evidences were found with new data [41; 43] yielding a precession period of $P_{res} \approx 7$ yrs. If RX J0720.4–3125 precesses, it would cause an advanced (the NS precesses towards the observer) and a retarded (the NS precesses backwards with respect to the observer) signal, where the timing residuals would follow a sine [92], as discussed in section 1.4.2. For two hot spots on the surface of RX J0720.4–3125 the phase residuals qualitatively may have the shape of an abs(sine), having twice the period of the corresponding sine ($P_{res} \approx 14$ yrs), since the timing is not sensitive to which hot spot is causing the residuals and precessing towards/backwards the line of sight. There is evidence for such a longer period seen in the variable phase lags between hard and soft photons, see [41; 43; 51] and figure 4.13. However, it has to be shown whether this scenario can explain the spectral behaviour seen in figure 4.1 as well. Formally, also the spectral changes would then undergo a periodic behaviour having $P_{res} \approx 2 \times 7$ yrs. A long term period of $P_{res} \approx 14$ yrs could explain why

5. DISCUSSION

the spectral changes do not show a periodic trend (figure 4.1) yet, since the time span of the XMM-Newton observations would cover less than one cycle in this case.

Indeed, the phase residuals in figure 4.13 seem to follow a periodic pattern. If the phase residuals including the most recent data are fitted with an error weighted sine or $\text{abs}(\text{sine})$, the long term periods are 7 – 9 yrs or 14 – 18 yrs, respectively. The fit results are listed in table 5.1 and shown in figure 5.1 (for the timing solution without ROSAT data). In all cases, the fit yields formally unacceptable values for $\chi^2/d.o.f$. However, even reducing the systematic errors from the different instruments due to energy selection (hard photons), still some Chandra data points deviate from the phase residuals derived from XMM-Newton data close in time, suggesting that the systematic error is larger than the statistical errors. Thus, scaling the errors with a factor of two, the values for $\chi^2/d.o.f$ reach from 1.3 to 2.4. Moreover, if the two hot spots have slightly different properties, the two humps in the sine or $\text{abs}(\text{sine})$ are not equal, that also worsens the formal $\chi^2/d.o.f$ value (see chapter 6). The new turning point of the phase residuals would have been at $MJD = 55387_{-100}^{+107}$ days (first half of July 2010) or at $MJD = 55240_{-8}^{+8}$ days (first half of February 2010) for the sine or the $\text{abs}(\text{sine})$ fit, respectively (see figure 5.1).

Since the sine and the $\text{abs}(\text{sine})$ fits result in unacceptable values for $\chi^2/d.o.f$ and both assume a certain shape of the periodic pattern, the string length algorithm that makes no assumption for the shape and is predestined for sparse data was implemented to search for a long term period. The string length of the phase residuals reach a minimum for a long term period between 6 and 8 yrs with an absolute minimum at ≈ 6.8 yrs. Although this minimum is not sharp, a pure sine would also cause a broad minimum since the phase residuals are sparse with variable time gaps between the observations. If the phase residuals did not follow a periodic pattern, the string length periodogram would look different. The results are shown in figure 5.2.

Free precession may occur if the neutron star has an elliptic shape with ellipticity ϵ , precession period P_{res} and spin period P , which roughly follow the relation $P \sim P_{res} \times \epsilon$ [57] for a rigid body. This leads to $\epsilon \approx 10^{-8}$ for RX J0720.4–3125. Although deformation caused by centrifugal forces are highly dependent on the Equation of State (EoS), RX J0720.4–3125 has a far too large spin period, so that this possible source of deformation can certainly be excluded, see [57], equations 13 to 15 therein.

Motivated by the observation of glitches in radio pulsars, neutron stars are supposed to host a fluid interior under their crust. This interior would interact with the inner crust and would cause damping of free precession due to mutual friction [5]. In the case of RX J0720.4–3125, free precession would have been damped after 130 to 3500 yrs (again, strongly dependent on the EoS), at least a hundred times less than the neutron star's age [122].

Table 5.1: Fit results from fitting the phase residuals with a sine or abs(sine). Only those observations used for the current timing solutions are used for the fits of the long term periods. All errors denote 1σ .

long term fit	P_{res} [yrs]	rms [s]	$d.o.f$	$\chi^2/d.o.f$
“all data”				
sine	7.30 ± 0.37	0.29	70 – 5	7.8
abs(sine)	14.35 ± 0.31	0.31	70 – 5	8.6
without ROSAT				
sine	8.91 ± 0.21	0.19	64 – 5	5.3
abs(sine)	17.48 ± 0.24	0.21	64 – 5	6.5
without Chandra				
sine	7.26 ± 0.18	0.31	58 – 5	9.7
abs(sine)	14.41 ± 0.30	0.33	58 – 5	8.7

Precession caused by an unseen perturber is likely excluded: if r_p is the distance of the perturber (having the mass M_p) to the neutron star and θ_p is the inclination to the perturbers orbit, then the perturber mass required for bound precession would be (see also [80])

$$M_p = \frac{8\pi^2}{3GPP_{res}\epsilon\cos\theta_p} r_p^3. \quad (5.1)$$

Including the values of RX J0720.4–3125 ($P_{res} = 14$ yrs, $\epsilon = 10^{-8}$), the perturber mass would scale with $M_p \approx 5 \times 10^{-11} \times (r_p/1 \text{ km})^3 \times M_\odot$. Indeed, the required perturber mass would be around some M_\odot , if it was located at $\sim 3 \times 10^3$ km from the neutron star. However, at this distance the perturber could not be composed by ordinary matter, but has to be either another neutron star or a black hole. Moreover, a perturber of a few Jovian masses would be located even closer (at a few 10^2 km) to the neutron star.

If RX J0720.4–3125 shows precession (that is strongly supported by the variable phase shift between soft and hard photons), then something prevents damping (see e.g. section 5.1.3) or the precession was caused recently, i.e. within the last few thousand years. Certainly, RX J0720.4–3125 does not show bound precession.

5.1.2 The glitch hypothesis

Another hypothesis to explain the phase residuals is a glitch event that would change the spin period and the spin-down. Applying the “all data” glitch solution proposed in [129] with a glitch that occurred at $t_g = 52866$ days significantly reduces the phase residuals for the observations available at this time ($MJD = 53500$ days). However, including the most recent XMM-Newton and Chandra observations from this work, the residuals grow to larger values. Therefore, a new parameter was introduced by fitting a parabolic slope to

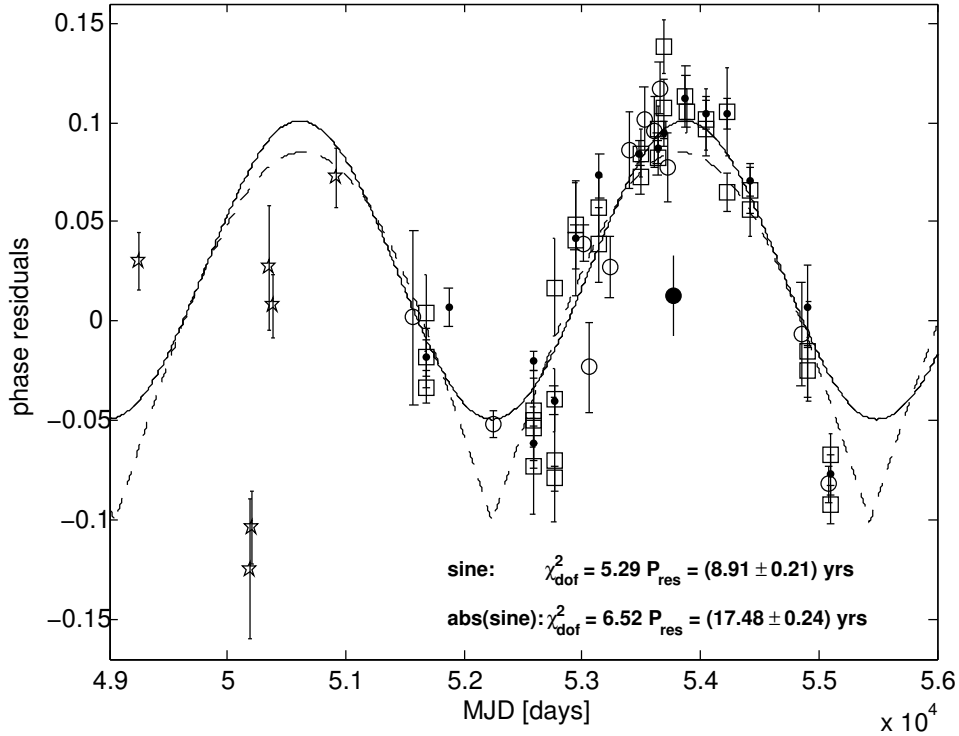


Figure 5.1: Phase residuals of RX J0720.4–3125 after applying the timing solution derived without the ROSAT observations and without the Chandra HRC observation 7251 (marked as a filled circle) to all observations. The best fits with a sine and an abs(sine) model (only the observations used in the current timing solution are used for the fits) are also shown (see table 5.1). Symbols follow those in figure 4.8 and figure 4.13, all error bars denote 1σ .

the glitch solution in [129] with the physical meaning of a post-glitch correction \dot{f}_c for the spin-down, while keeping the parameters, as valid before t_g , constant. The error weighted fit for the hard band using all data (and fitting the light curves with a pure sine to be consistent with [129]) yields $\dot{f}_c = -1.11 \pm 0.10 \times 10^{-17}$ Hz/s (errors indicate 1σ) that significantly reduces the phase residuals. In [129] the post-glitch spin-down was calculated to be $\dot{f}_{old} = -1.040 \pm 0.030 \times 10^{-15}$ Hz/s, i.e. the corrected value is $\dot{f}_{new} = \dot{f}_c + \dot{f}_{old}$. All other parameters (spin period and spin-down before t_g , spin period after t_g and t_g itself) are equal to those in [129]. Compared to the sine and abs(sine) fits, the new glitch solution formally fits better ($\chi^2/d.o.f = 2.8$, $rms = 0.31$ s), see figure 5.3.

A glitch would explain the sudden rise of the temperature around $MJD = 53000$ days, followed by a slow cool-down. However, the glitches known from radio pulsars (here, no temperatures can be measured) have relaxation times (in the timing) of some tens or a few hundred days, while RX J0720.4–3125 has not reached its initial temperature for seven years. Figure 4.1 indicates that the temperature rise already began one year before t_g ($MJD = 52500$ days) and just accelerated at t_g . While the hardness in the spectra changed, the total X-ray luminosity (120 – 1000 eV) stayed constant. Both facts would

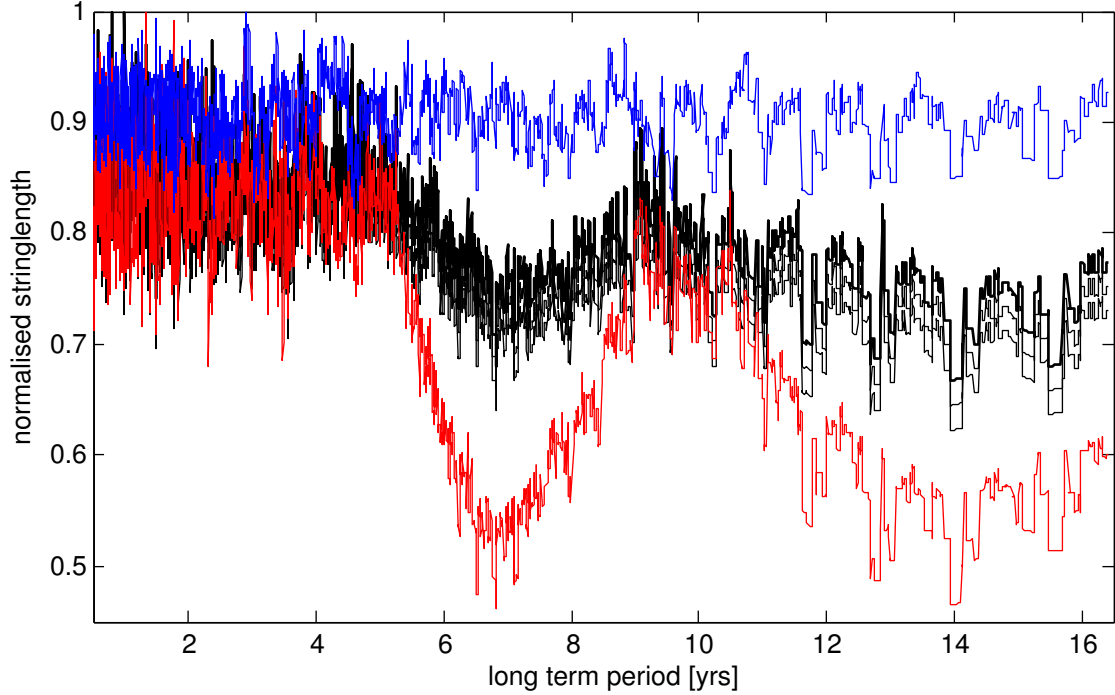


Figure 5.2: The string lengths derived from the phase residuals (taking all errors into account) shown in figure 5.1, represented by black lines, compared to the string lengths if the phase residuals would have been produced by a pure sine (red) and randomly (blue line).

not exclude a glitch, but the changing phase gap between hard and soft photons and the decrease of the size of the emitting area at the same time cannot easily be explained by the glitch model.

5.1.3 Tkachenko waves

Free precession in a neutron star is supposed to be damped [57; 79], but there might be a mechanism that prevents precession from being damped. In 1970, Tkachenko waves (that are standing sound waves propagating in the lattice of neutron vortices) were proposed to explain the long term periodic variations of the Crab pulsar [112]. Such phenomena are observed in superfluid helium under laboratory conditions [123]. Recently it was proposed [103] that a glitch generated Tkachenko waves in RX J0720.4–3125 that leads to precession with the precession period P_p ($P_p \sim P/\epsilon$) equal to the period of the standing Tkachenko wave P_T (i.e. the periods are in resonance). Since the Tkachenko wave propagates parallel to the neutron star’s spin axis and the neutron star’s moment of inertia is non-symmetric, i.e. $\epsilon > 0$, Tkachenko waves periodically change the spin frequency.

Assuming that the neutron star is composed of a crust with a negligible moment of inertia and a superfluid interior below it, only consisting of neutrons, the period of the Tkachenko

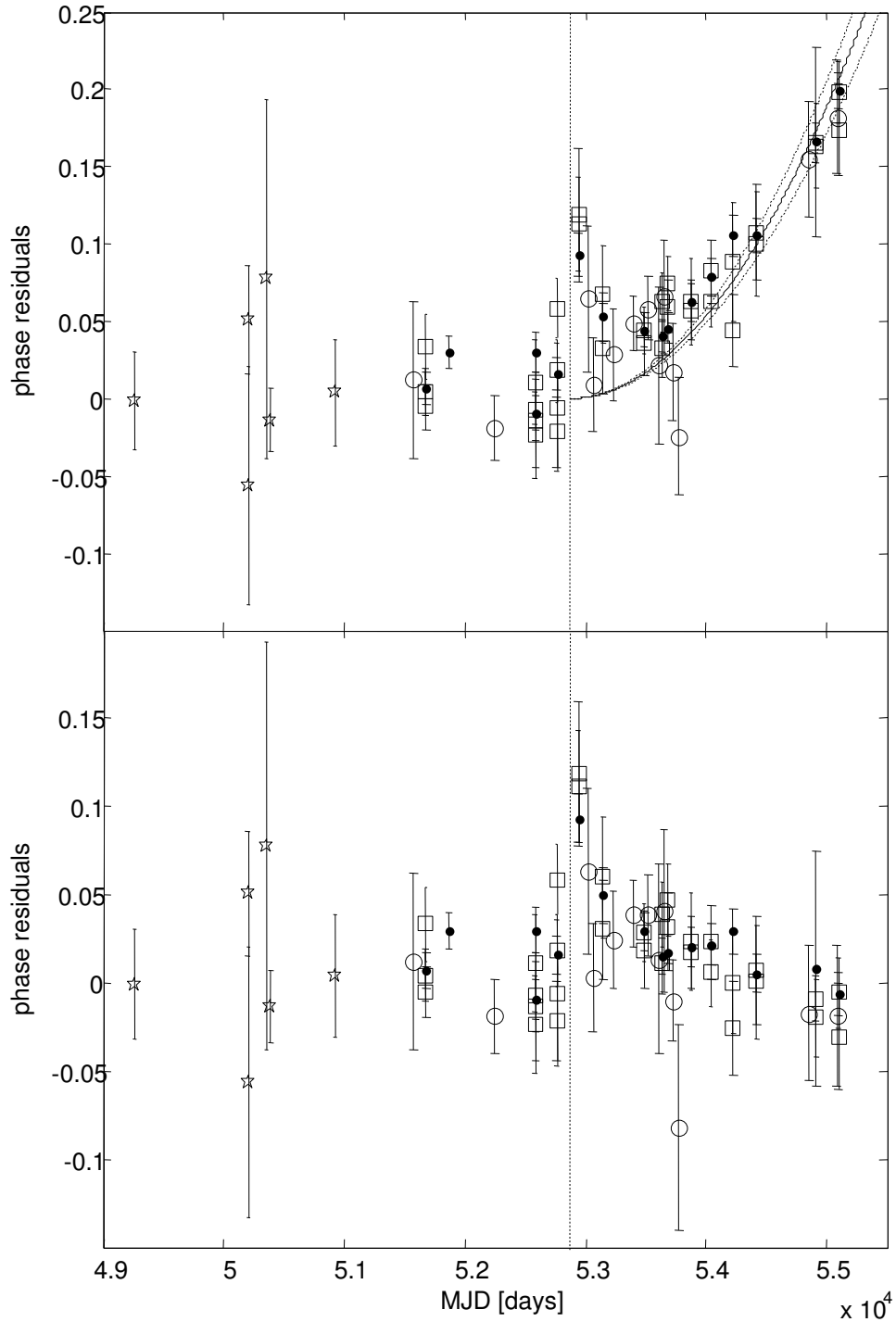


Figure 5.3: Upper panel: The phase residuals of RX J0720.4–3125 after applying the glitch solution (“all data”) in [129]. The glitch time $t_g = 52866$ days is marked as dotted vertical line. According to equation 3.4, the deviant points after t_g are fitted with an error weighted parabolic slope (solid line, dotted parabolic lines indicating the 1σ confidence range.) corresponding to a post-glitch correction of $\dot{f}_c = -1.11(10) \times 10^{-17}$ Hz/s.

Lower panel: The phase residuals after applying the post-glitch \dot{f} correction. Symbols follow those in figure 4.8.

wave in years would be

$$P_T \sim 1.77 \times \left(\frac{R}{10 \text{ km}} \right) \times \sqrt{\left(\frac{P}{1 \text{ s}} \right)}, \quad (5.2)$$

see [112]. In the case of RX J0720.4–3125, equation 5.2 yields a long term period of 5 – 7 yrs for reasonable radii. It should be mentioned that equation 5.2 only accounts for the fifth harmonic of the Tkachenko wave, following [112]. After the long term variations of the Crab pulsar could not be verified, Tkachenko waves did not play a role in astrophysics for a long time. Only recently, Tkachenko waves were investigated in more detail [93]. In contrast to a superfluid sphere, in [93] the modes are calculated for a shell of two superfluids for different shear viscosities of normal matter coupling to the superfluids. Generally, the periods derived for strong coupling are larger than predicted by equation 5.2 and the mutual friction may be too weak to damp the oscillation. Hence, even a long term period of 15 yrs for RX J0720.4–3125 could be explained in this way. Several radio pulsars show quasi-periodic structures in their timing behaviour. These “periods” are a factor of a few too large to obey equation 5.2, but could be explained by Tkachenko waves in principle – just with a strong coupling of the normal matter to the superfluid or for a lower harmonic than that used for equation 5.2.

The probability to observe a glitch causing precession via Tkachenko waves seems to be low [103]. In [145], a long term periodic oscillation with a period of approximately one year was observed in the glitching radio pulsar PSR B2334+61 after removing the (non phase coherent) glitch solution. Thus, Tkachenko waves merit more detailed investigations and a collaboration (with Sergei Popov and Armen Sedrakian) has already started.

5.1.4 Circumstellar and/or fallback disk

It is discussed in [3; 4] that some neutron stars may be surrounded by a fallback debris disk that is left over from the supernova event. Evidence for such a fallback disk was discovered around the neutron star 4U 0142+61 [138]. Since the discovery of a narrow absorption feature in the XMM-Newton RGS spectra of RX J0720.4–3125 [44] that likely originates from highly ionised oxygen (and the presence of maybe two further narrow absorption features found in the Chandra HRC-S/LETG spectra in this work) there is evidence for a fall back disk surrounding RX J0720.4–3125 as well.

The interpretation of such a feature is a priori not clear (see also the discussion in [44]): If the line originates from the neutron star atmosphere, it is red shifted by a factor of 1.11 ($M = 1M_{\odot}$, $R = 16 \text{ km}$) to 2.00 ($M = 2M_{\odot}$, $R = 8 \text{ km}$) and the ion itself is not known. Due to the Stark-effect, pressure and temperature, the lines should be broadened [96] to some tens of eV and splitted by the Zeeman-effect, depending on the atomic number Z .

5. DISCUSSION

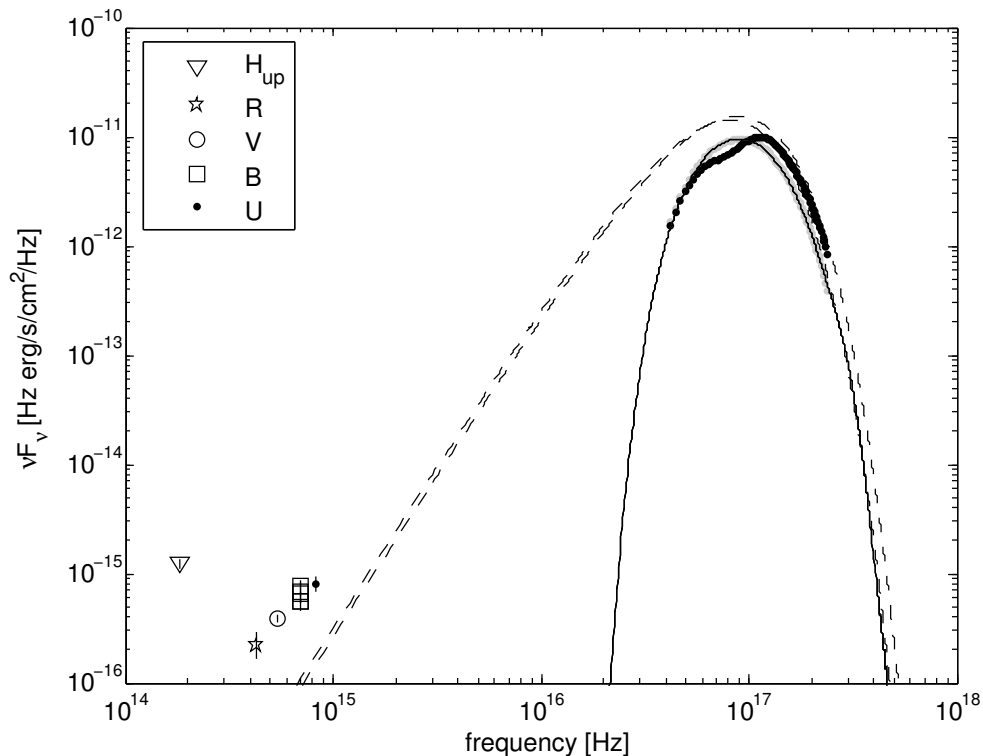


Figure 5.4: Spectral energy distribution of RX J0720.4–3125 from the near infrared to X-rays. The solid line represents the model spectra from XMM-Newton EPIC-pn fitted with the data points from the observations revolution 0078 (see also table 2.2). The black data points are obtained from the XMM-Newton EPIC-pn observation revolution 0815 with the broad absorption feature seen at 300 eV (7.25×10^{16} Hz). The dashed lines indicate the black body emission from both X-ray observations without any absorption for $T_{eff} = 86.5 \pm 0.4$ eV and 94.7 ± 0.5 eV, respectively. The U and B magnitudes are listed in [91], the V band magnitude is taken from [28], R from [74] and the H band magnitude gives the upper limit according to [105].

The π lines are shifted by $\Delta E_\pi \sim 0.1 \text{ keV} \times (B/10^{11} \text{ Gauss})^2 \times (26/Z)^2$ while the σ lines are shifted by $\Delta E_\sigma = (11/5) E_\pi$ and the centre is also shifted towards higher energies by $\Delta E \sim 0.17 \text{ keV} \times (B/10^{11} \text{ Gauss})^2 \times (26/Z)^2$. Moreover, the centre shift depends on the electron density, see [114].

The detected line energy of 0.57 keV fits to OVII or OVI [47] without gravitational redshift. Such lines are detected in some Galactic low-mass X-ray binaries [144]. Thus, the line likely originates from the interstellar or circumstellar medium. If highly ionised oxygen is present close to the neutron star surface, OVIII at 0.653 keV should appear at 0.57 keV with a reasonable redshift of 1.16 (or 1.17) and the corresponding OVII K_α resonance line should appear at 0.49 keV. In [44] it is argued, that such an absorption feature probably could be seen. While this absorption feature could not be detected in the RGS data in this work, an absorption line at the particular energy in the Chandra HRC-S/LETG data was found. In addition, a further absorption feature at 0.53 keV was found in the Chandra HRC-S/LETG

Table 5.2: Orbital elements after fitting the phase residuals of RX J0720.4–3125 in figure 5.1 with an orbital solution. All errors denote 1σ .

orbital element	value
period	2530 ± 130 days 6.93 ± 0.35 yrs
eccentricity	0.93 ± 0.10
long. of ascending node	-0.45 ± 0.32 rad
periastr. passage [<i>MJD</i>]	50220 ± 130 days
$a_{Comp} \times \sin(i)$	3.8 ± 2.3 AU
$a \times \sin(i)$	0.0026 ± 0.0016 AU
$\chi^2/d.o.f$	$640/(70 - 7) = 10.2$
mass function/ $\sin^3(i)$	$3.3 \pm 6.3 \times 10^{-7}$ M_J

data (see figure 4.6) that likely originates from the K-edge of neutral oxygen OI [60] at rest. This indicates an overabundance of neutral oxygen in the line of sight or might be a result of inexact modeling of the edge.

All M7 are dim in the optical bands (see table 1.2), but the measured optical fluxes are 5 to 10 times larger than expected by extrapolating the black body X-ray spectrum. For RBS 1774 the optical excess is even a factor of ≈ 30 , see [153]. It is shown in [44] that an ambient medium/cloud around RX J0720.4–3125 could explain the optical excess (figure 5.4) for a certain set of parameters (Note, that RX J1856.4–3754 also exhibits an optical excess, but no disk could be detected [108]. The optical excess can also be explained by a condensed hydrogen atmosphere, see [48; 155; 156], and not mandatory with a disk.). If this cloud or disk has a patchy structure and orbits around RX J0720.4–3125, it may account also for the spectral irregularities. A fall back disk could easily lead to an accretion event by the impact of an asteroid, as proposed by [129] for the glitch event. Eventually a disk may block radio emission, as shown in [29], unless RX J0720.4–3125 is an off-beam pulsar which is more likely.

Certainly a fall back disk does not explain all peculiarities of RX J0720.4–3125, e.g. (again) the variable phase shift between hard and soft photons, but a detection or non-detection would rule out some possibilities. A debris disk heated by the neutron star would have temperatures about 100 to 1250 K (last number refers to the limit for evaporation of dust) for a distance of 0.67 to 6.7 AU, respectively, hence would be detectable in the near infrared [6]. Therefore a Spitzer observation was proposed (and accepted) [106], but not executed yet.

5.1.5 Orbital motion

Neutron stars that host planets, or better host objects with planetary masses, are a rare configuration but are clearly detected in a few cases, see e.g. [9; 140]. If a planet orbited

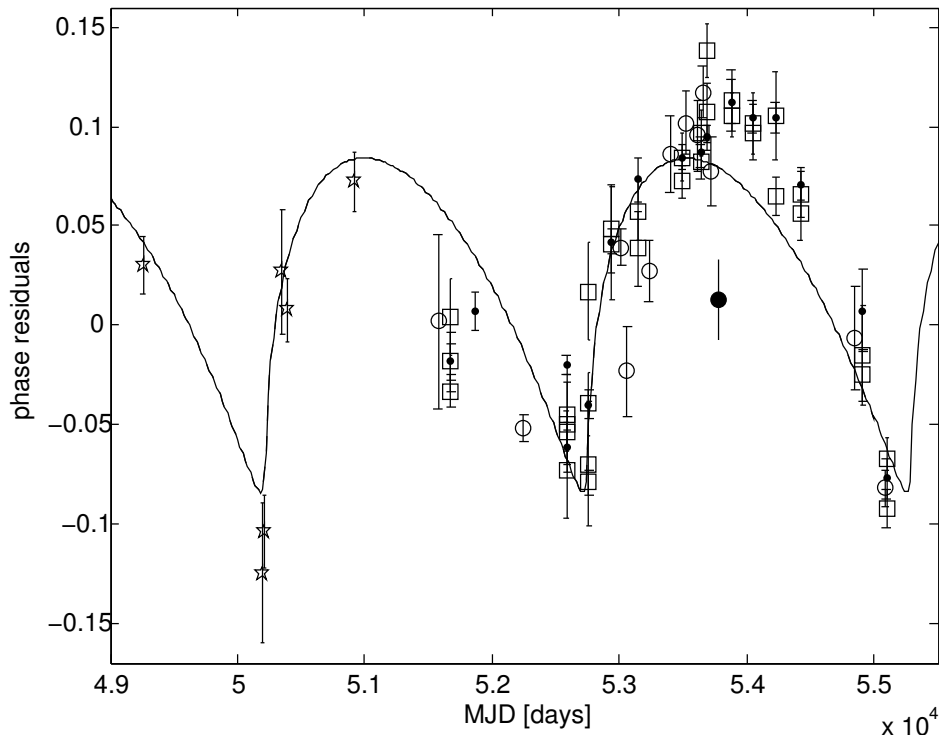


Figure 5.5: Error weighted orbital fit of the phase residuals of RX J0720.4–3125. The symbols follow those in figure 5.1 and figure 4.8.

around RX J0720.4–3125, it would cause orbital motion of the neutron star around the common barycenter. This wobbling would cause time delays in the arrival times of the pulses, since the light needs more time to travel the additional way from the projection of the semi major axis (having an inclination i of the orbital plane) with respect to a distant observer. Vice versa, the orbital motion causes an advanced signal for a different orbital phase. Depending on the orientation and the eccentricity of the orbit, the phase residuals do not necessarily follow a sinusoid.

Since the long term period of RX J0720.4–3125 is on a time scale of years and the neutron star mass should be comparable to a solar mass, the possible companion should have a mass, M_{Comp} , of about some Jovian masses. Non-detections in the H-band [105] down to 22.9 mag yield an upper limit of $M_{Comp} = 15 M_J$ for RX J0720.4–3125, if the companion formed together with the neutron star after the supernova 1 Myrs ago and still cools down. This limit for M_{Comp} is valid for a distance of 360 pc of RX J0720.4–3125 to the Sun.

Fitting the phase residuals shown in figure 5.1 with orbital motion yields $M_{Comp} \times \sin(i) = 0.93 M_J$ assuming a neutron star mass of $M = 1.4 M_\odot$. The inclination of the orbit is unknown, but assuming an uniform distribution, the probability is less than 4% that such a hypothetical companion would have a mass above $15 M_J$ (inclination less than 3.6°), i.e. could have been detected in [105]. Thus, a companion could still be undetected by direct

imaging.

The fit result is shown in figure 5.5 and the orbital parameters are listed in table 5.2. To obtain a reasonable fit, it is necessary to cover at least two cycles, i.e. the phase residuals obtained from the ROSAT data are included for the orbital fit.

The fitted orbit is highly eccentric, i.e. is hard to determine, thus the orbital elements have large errors and the fit corresponds to $\chi^2/d.o.f = 10.2$, that is even worse than the sine and abs(sine) fits listed in table 5.1. Since the orbital motion also does not explain the variable phase shift between hard and soft photons and the fit yields large errors, the companion hypothesis might be unlikely. Fortunately, when searching for a fallback disk with Spitzer [106], an object having a few Jovian masses can also be detected, if existing.

5.2 Phase resolved spectroscopy

The values of the spectral properties of RX J0720.4–3125 in table 4.2 are derived from the spin phase averaged spectra. While rotating, RX J0720.4–3125 exhibits different parts of its surface depending on the rotation phase. The spectral properties for a certain rotation phase might be different from the values listed in table 4.2. To derive a phase resolved evolution of the spectral properties, a certain timing solution has to be applied to assign the photon events with a phase value.

In [41], figure 4 therein, such an investigation was performed using the “all data” phase coherent timing solution in [63]. Within this thesis, an updated timing solution derived by including the most recent observations is now available, as well as a timing solution including a glitch event that occurred at $MJD = 52866$ days [129] but corrected, as discussed in section 5.1.2. The assignment of the events by a phase value depends on the applied timing solution and thus influences the trend of the phase resolved spectral values. Therefore, in addition to the other timing solutions, the phase was calculated using the periods of the individual observations (see table A.1, for the hard band, to be in accordance with the timing solution derived in this work and the corrected glitch solution discussed in section 5.1.2) with the reference point set to the time of maximum light closest to the middle of the individual observation. In this case, each observation is independent from the others (thus, no \dot{f} is required). This avoids that an pulse profile obtained from an observation, that is not well represented by a certain timing solution, is shifted and smeared out for the phase resolved spectral fitting (i.e. no change within a rotation cycle can be seen, although it exists).

According to [41] the XMM-Newton EPIC-pn observations performed in full frame mode with thin filter were used only (see table 2.2). The phase values for each photon arrival time were calculated from the four different timing solutions mentioned before. Like in [41],

5. DISCUSSION

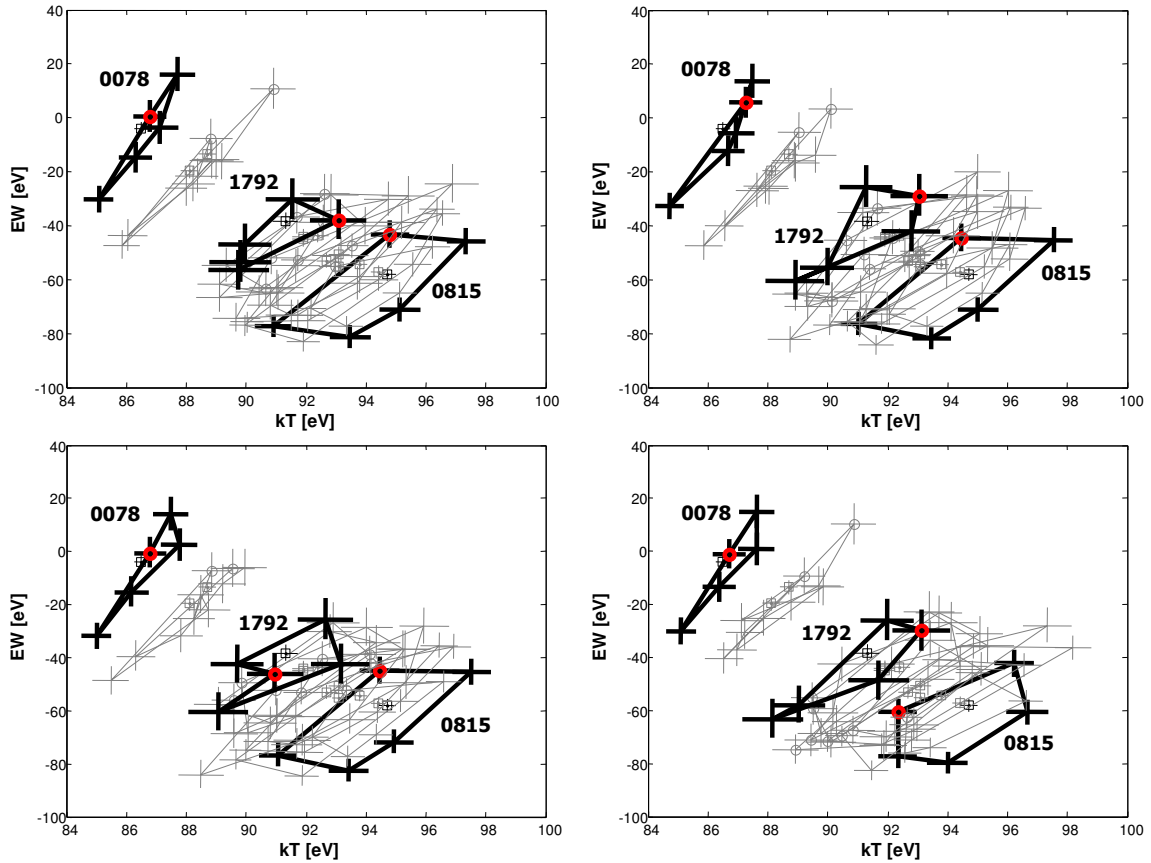


Figure 5.6: Phase resolved (five phase bins) evolution of temperature and equivalent width of RX J0720.4–3125 from the spectra derived with XMM-Newton EPIC-pn in full frame mode with thin filter for different timing solutions. The curves obtained from the data of revolution 0078 (first observation), 0815 (spectra with highest values of temperature and modulus of the equivalent width) and revolution 1792 (most recent data, see table 2.2) are shown with thick black lines. The squares indicate the average values according to table 4.2, the circles (marked red for revolution 0078, 0815 and 1792 for better visibility) mark phase 0.0 – 0.2, while the ellipsoidal tracks evolve counter-clockwise. All errors denote 1σ uncertainty, see also [41], figure 4 therein, and [51], figure 12 therein.

Upper left: After applying the timing solution from [63], “all data” solution therein.

Upper right: After applying the solution from this work (without ROSAT data), see section 4.2.2 and [52].

Lower left: After applying the corrected glitch solution discussed in section 5.1.2 and [52] for the phase calculation.

Lower right: The phase was derived from the individual observations where the maximum light is set to zero phase.

the photons were divided by phase in five bins (0.0 – 0.2, 0.2 – 0.4, 0.4 – 0.6, 0.6 – 0.8 and 0.8 – 1.0), i.e. 65 spectra were obtained (13 observations, each divided in five phase bins). These spectra were fitted simultaneously with the standard fit model (see table 4.1) with N_H , σ_{line} and E_{line} kept free, but fitted with the same values for all 65 spectra. All other parameters were allowed to vary for all 65 spectra, see section 4.1, [41] and [51].

Depending on the timing solution, the spectra fit with $\chi^2/d.o.f. = 1.13 - 1.14$. The evolution of the equivalent width versus temperature follows an ellipsoidal track that evolves counter-clockwise during a rotation cycle. The variations of equivalent width versus temperature for the different timing solutions are shown in figure 5.6.

Generally, the ellipsoidal tracks moved from low temperatures and lower negative values for the equivalent width (revolution 0078) to higher temperatures and larger negative values for the equivalent width and reached their maximum at revolution 0815 (this behaviour covers a time span of four years). Since then, the ellipsoidal tracks moved slowly, but steadily towards to their initial position, but have not reached it yet (for five years). During this evolution, the phase averaged values, as listed in table 4.2, moved along a straight line (from revolution 0078 to revolution 0815) and moved back on the same trajectory. While the ellipsoidal tracks exhibited a slim shape (revolution 0078, 0533 and 0534) at the beginning of the mission, they became broader (until revolution 0815) and now seem to become slim again. The exact shape of the track and the maximum values reached during a rotation cycle depend on the chosen timing solution (see figure 5.6), while the general trend is independent from the timing solution.

In the average spectrum of revolution 0078, the equivalent width is consistent with zero, but reaches extreme values in both directions, that are not consistent with zero for different phases, during the rotation cycle. The equivalent width even is formally in emission (an absolute offset could however be caused by calibration uncertainties), also during the revolutions 0533 and 0534, rather than absorption for some phases.

The ellipsoidal tracks seen in figure 5.6 show the presence of cooler and hotter parts of the neutron stars' surface, but from their evolution it is not possible to judge whether they show a long term cyclic behaviour or move back to the initial conditions, coming from an unique deviation.

6

Modelling a free precessing neutron star

Although there is no final conclusion about the origin of the spectral and temporal changes of RX J0720.4–3125 yet, for various reasons discussed in chapter 5, free precession seems more likely than the other hypotheses mentioned in this work. Here it is simulated whether all changes could be the product of free precession (of a sphere with two hot spots which may not lie exactly antipodal) with one set of geometrical parameters. These parameters are compactness, spot sizes and their angular shift with respect to each other, the temperature distribution and the viewing and precession angle. A precessing sphere with all these (then fixed) parameters should reproduce the changes in the temperature and observed size of the emission area, the pulsed fraction and the phase shift between soft and hard photons. Such a model was tested for RX J0720.4–3125 by Roberto Turolla in [154]. However, it was not possible to reproduce all properties with one single set of parameters at once and the parameter space is too large to be scanned systematically. The intention of the model presented here is to create a simplified but faster code to scan the parameter space. The aim of this modeling is to start from basic assumptions and to clarify whether the observable properties can be reproduced in principle (qualitatively), namely the non-sinusoidal variations in the spectral properties while a periodic pattern in the timing behaviour is seen. When such a geometric configuration is found, the model also should obey the pulsed fraction and the shape of the light curves. The results of this model then could be used for a more constrained investigation with the more detailed model in [154].

The software for the simulation in this work was written in *Matlab*. The details of the codes and the physical input are discussed here.

6.1 The model

6.1.1 The geometry of the problem

To model the emission geometry of a neutron star with two hot spots on its surface, the designation for the parameters given in [109] and illustrated in figure 6.1 is adopted. In contrast to [109], where the spot has an infinite small size, both hot spots are extended in this work, since it is known that the size of the emitting area of RX J0720.4–3125 corresponds to a few km radius.

If z is the spin axes of the neutron star, θ is the angle between the unit vector \vec{n} , that points from the centre of the neutron star to the centre of the hot spot, and the neutron star's spin axis. The spin axis is seen by a distant observer with an inclination i . When a photon leaves the hot spot with the angle α with respect to \vec{n} , i.e. has the initial direction \vec{k}_0 , it is influenced by gravity (leading to light bending), thus will have the angle $\psi \neq \alpha$ with respect to \vec{n} at infinity. The final direction of the light signal is expressed by the vector \vec{k} . By definition, $\cos(\psi) = \vec{k} \cdot \vec{n}$, that yields

$$\cos(\psi) = \cos(i) \cos(\theta) + \sin(i) \sin(\theta) \cos(\phi). \quad (6.1)$$

As seen from figure 6.1, the angle ϕ denotes the spin phase, i.e. $\phi = 2\pi t/P$ with $\phi = 0$ at $t = 0$ with the hot spot facing the observer. ψ accounts for the apparent inclination of the hot spot.

For the antipodal hot spot, only $\theta = \pi - \theta_{antipodal}$ and $\phi = \pi + \phi_{antipodal}$ has to be substituted, with the restriction that the flux equals zero, if $\cos(\alpha) < 0$. Usually, the hot spots are not exactly antipodal. Therefore the shift angles θ_{off} and ϕ_{off} that account to the offset of the second hot spot from the antipodal position are introduced.

6.1.2 Physical input

6.1.2.1 Light bending and light emission

To connect the observed light path to the emission from the surface, an expression leading from α to ψ has to be found. The approximation

$$\cos(\alpha) \approx \left(\frac{r_s}{R}\right) + \left[1 - \left(\frac{r_s}{R}\right)\right] \cos(\psi) \quad (6.2)$$

which was derived by [10] was adopted (using the Schwarzschild metric with r_s being the Schwarzschild radius and R is the radius of the neutron star). The error made by equation 6.2 depends on compactness and the emission angle α . For any emission angle, this error is less than 10% if the neutron star exceeds twice its Schwarzschild radius and

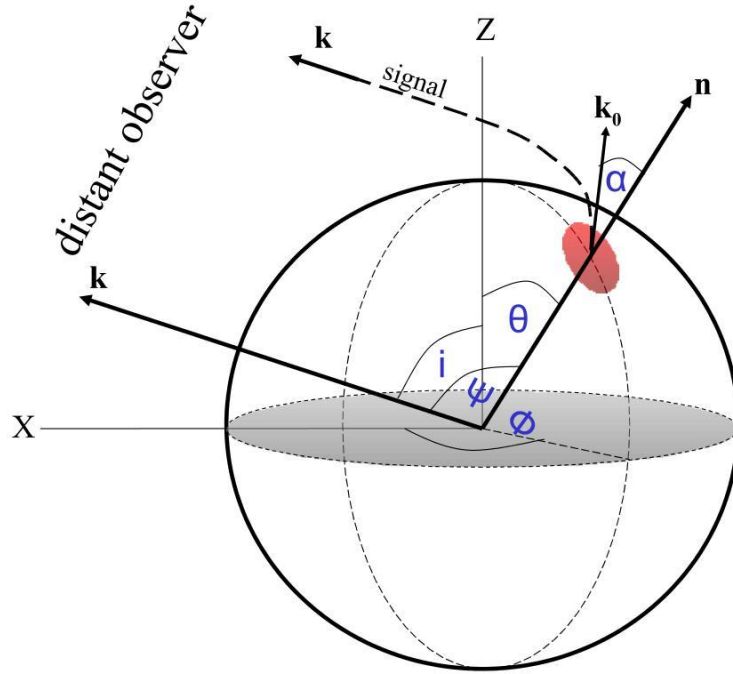


Figure 6.1: The geometry of a rotating sphere with light bending, see also figure 1 in [109].

less than 1%, if $R = 3r_s$, i.e. is fully sufficient for the purposes in this work, see figure 2 in [10].

A surface element is visible at infinity, if

$$\cos(\psi) \geq -\frac{r_s}{R - r_s}, \quad (6.3)$$

i.e. parts of the neutron star that are behind the plane of sight are visible. The surface elements that do not obey equation 6.3 were disregarded in the code. The contribution of each surface element dS varies with equation 6.1. Since RX J0720.4–3125 spins with a period of ≈ 8.4 s, the time delay from the photons originating from different regions of the neutron star and the (special) relativistic aberration are negligible. To calculate the final expression for the flux, an isotropic black body radiation with the emission E^1 was assumed. This assumption is probably the most sensitive regarding to the flux. The emission is completely different, if the radiation is non-isotropic, see [109]. According to these simplifications, the final contribution to the flux dF from a surface element $dS = R^2 d\mu d\phi$ is

¹A black body emits with the intensity $I \sim \nu^3 / (\exp[\frac{h\nu}{kT}] - 1)$, where k is the Boltzman constant and ν is the photon frequency. Then, $E = \int_{\nu_2}^{\nu_1} I d\nu$. The flux contributions from different energy bands were calculated by changing ν_1 and/or ν_2 . Note, that E is a function of α for non-isotropic light emission.

$$dF = N \left[1 - \left(\frac{r_s}{R} \right) \right] E \cos(\alpha) \frac{d\cos(\alpha)}{d\mu} dS, \quad (6.4)$$

where N is a normalisation constant (accounting for distance, number of photons and constant factors) and $\mu = \cos(\psi)$. With equation 6.2, equation 6.4 can be integrated (here: summed) according to the variables shown in figure 6.1.

Each surface element has a given temperature and emits like a black body and the light curve is obtained by summing up the contributions of each surface element at the different spin phases according to equation 6.1.

6.1.2.2 Temperature distributions

The temperature distribution on the surface of an isolated neutron star is affected by the local magnetic field and is currently not fully understood. Depending on the magnetic field geometry and different surface conditions, various models were proposed [1; 32; 33; 35; 101; 148]. Each temperature distribution itself includes free parameters and it is not exactly known which description is valid for RX J0720.4–3125. Thus in this work three different simple temperature distributions were implemented. They are a priori assumed and not derived from the magnetic field self-consistently. Since the radius of the neutron star is just a normalisation factor in this case, the radius of a circular hot spot is measured by the angle Ξ . The simplest temperature distribution is uniform: $T(\xi) = T_0$ if $\xi \leq \Xi$, with respect to the centre of the hot spot, and $T(\xi) = 0$ elsewhere. Another approach is a Gaussian distribution with $T(\xi) = T_0 \exp[-0.5(\xi/\Xi)^2]$. Probably the most realistic distribution according to [35] is $T(\xi) = T_0 |\cos(\xi)|^{0.5}$. Here the last temperature distribution is named “magnetic”, since it is an approximation derived from the magnetic dipole field geometry. Unlike the other two temperature distributions, this distribution has no size in the sense of Ξ and is valid for the entire surface. All temperature distributions are illustrated in figure 6.2. As it was shown in section 3.3, the phase residuals of RX J0720.4–3125 measured with different instruments are in best agreement, if only the hard band of 400 – 1000 eV is used. The broad absorption feature at 300 eV might be explained as a cyclotron line. However, the physical origin of this line is actually unclear, but the mechanism that causes this line has to be known to implement this line (and its variation) correctly. Therefore, the line was not included in the model and the investigations were mostly limited to the hard band (where the influence of the line is much less than in the soft band).

6.1.2.3 Free precession

Bound precession caused by a companion (like the Earth-Moon system) is probably an unlikely scenario for RX J0720.4–3125, as discussed in section 5.1.1, thus this work focuses

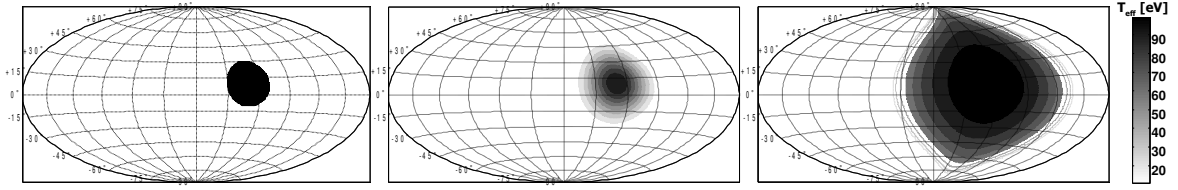


Figure 6.2: The different temperature distributions used in this work. From left to right: uniform, Gaussian, “magnetic”. In all three examples, the central temperature equals 100 eV, $\Xi = 20^\circ$, $\phi = 50^\circ$ and $\theta = 80^\circ$.

on free precession. From the spectral variations it is hard to distinguish between bound precession, free precession and nutation.

Free precession occurs, if the spin axis $\vec{\omega}$ of the neutron star does not coincide with the axis of symmetry, \vec{s} (here the notation in [77] is adopted). Let \vec{L} be the vector of the (total) conserved momentum, then, at any time $\vec{\omega}$, \vec{s} and \vec{L} span a plane. The angle between \vec{L} and $\vec{\omega}$ scales with the ellipticity ϵ , i.e. practically $\vec{\omega}$ and \vec{L} are the same axis.

In this regime two new angles were introduced, the constant wobble angle θ_w between \vec{L} and \vec{s} and χ that is spanned between \vec{s} and \vec{n} , see figure 6.3. An observer *on* the surface of the neutron star would observe a circular motion of $\vec{\omega}$ about \vec{s} with the precession period [77]. If the observer sat on the emitting pole he/she would see $\vec{\omega}$ moving around him/her if θ_w is larger than χ and he/she would sit outside of this circle, if θ_w is smaller than χ . Both cases would cause different phase residuals for a distant observer. Due to precession, the spin phase is measured to be $\phi + \Delta\phi$ with the phase shift $\Delta\phi$. Since the approach that θ_w is small is used in [77] but the contributions from two hot spots (and different surface elements) with different latitudes are needed, the more general equations derived in [92] were implemented to calculate the phase shift $\Delta\phi$:

$$\tan(\Delta\phi) = \frac{\cos(\chi)\sin(\theta_w) - [1 - \cos(\theta_w)]\sin(\chi)\sin(\omega_p t)}{\sin(\chi)\cos(\omega_p t) + [\cos(\chi)\sin(\theta_w) + \sin(\chi)\cos(\theta_w)\sin(\omega_p t)]\tan(\omega_p t)} \quad (6.5)$$

if $\chi > \theta_w$, and

$$\tan(\Delta\phi) = -\frac{\sin(\chi)\cos(\omega_p t)}{\cos(\chi)\sin(\theta_w) + \sin(\chi)\cos(\theta_w)\sin(\omega_p t)} \quad (6.6)$$

if $\chi < \theta_w$, where $\omega_p t$ is the precession phase.

For the code, this means that θ_{new} varies with the amplitude θ_w during the precession cycle, as it would be seen by a distant observer with $\theta_{new} = \theta_w + \chi$ (according to figure 6.1 and figure 6.3), where χ corresponds to the “old” θ in figure 6.1. In the case of bound precession, the inclination varies in time with the precession period, but θ is constant since the spin axis revolves in a cone along the precession axis.

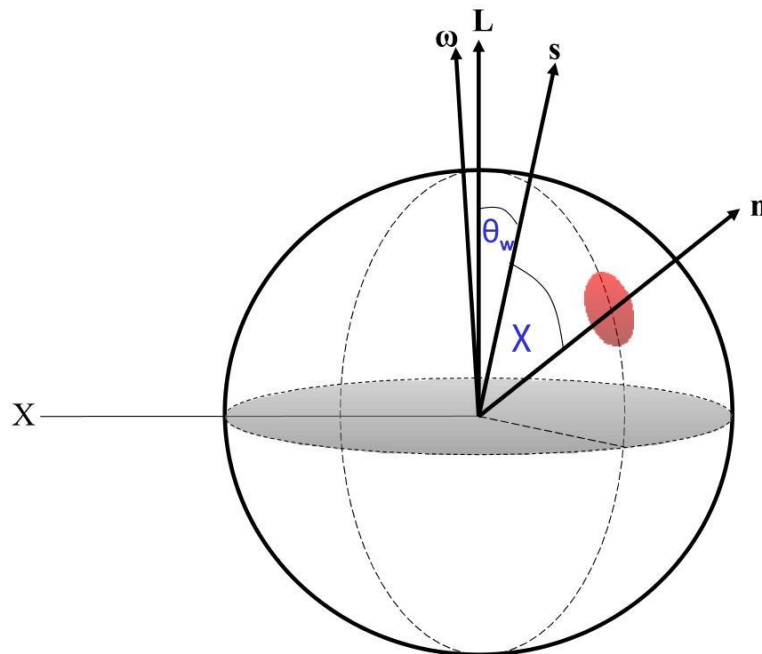


Figure 6.3: The problem of free precession applied to RX J0720.4–3125.

To calculate the total value of the phase residuals $\Delta\phi_{tot}$ contributed by all surface elements, the phase residuals calculated with equation 6.5 and equation 6.6 are weighted with the emitted flux $dF_{i,j}$ from each surface element, as seen by the observer, i.e.

$$\Delta\phi_{tot} = \frac{\sum_{i,j} dF_{i,j} \Delta\phi_{i,j}}{\sum_{i,j} dF_{i,j}}, \quad (6.7)$$

where i and j sum over all angles in longitude and latitude. If the variable phase shift between soft and hard energy band was investigated, $\Delta\phi_{tot}$ was calculated with $dF_{i,j}$ from 120 – 400 eV or 400 – 1000 eV, respectively.

In reality, the motion of RX J0720.4–3125 might be a result of a superposition of different effects. Equation 6.5 and equation 6.6 do not account for spin-down torques [2] and are only valid for a rigid, homogeneous body that rotates uniformly. The effects caused by the slight misalignment between $\vec{\omega}$ and \vec{L} are negligible, see [2], the appendix therein.

An interesting aspect is that for some precession parameters the timing residuals mimic orbital motion as caused by an unseen companion [92].

6.1.3 Test of the code and evaluation of different emission geometries

Certain configurations of the hot spots and the inclination should produce special features in the light curves. The examples in [12] and [10] were considered (here still without

precession) and the code was tested first with one, later with two hot spots.

Generally, light bending smooths the light curves, since parts of the neutron star are visible that would be invisible without relativistic effects. For some values of the compactness, the light curves undergo significant changes (see figure 6.4). If the hot spots have different properties that deviate much from each other (e.g. size and temperature), each hot spot will dominate the light curve in a different energy band. The cooler spot appears with a phase shift of 180° relative to the hotter spot. This leads to a phase gap of the residuals between two bands, as illustrated in figure 6.4. For RX J0720.4–3125 the properties of the hot spots might be less different as in the case of the modeled geometry producing the light curve seen in figure 6.4, but nevertheless will produce a phase gap between hard and soft photons. However, this phase gap will be constant in time and an additional motion (e.g. precession) needs to be superimposed on to the rotation to produce variable phase gaps as seen in the phase residuals of RX J0720.4–3125 (figure 4.13). The general influence of different geometries is shown in figure 6.5 and figure 6.6. From the light curves only, it is not possible to distinguish between free precession and bound precession (figure 6.5), since they qualitatively undergo the same changes.

The light curves of RX J0720.4–3125 are almost sinusoidal and the pulsed fraction has values around 11% (120 – 1000 eV) that limits possible configurations for the surface geometry. If the inclination has values around 90° , θ cannot be much larger than 20° , otherwise the pulsed fraction would be too large or the temperature profile on the edge of the spot has to be very smooth. On the other hand, the inclination cannot be far from 90° . If the inclination was close to zero, i.e. RX J0720.4–3125 would be seen pole on, no rotation (i.e. pulsations) would be visible for any values of θ . Moreover, the pulsed fraction is also influenced by the properties of the hot spots themselves, as illustrated in figure 6.7.

6.2 Procedure and fit results

If there is a combination of the geometrical properties of RX J0720.4–3125, that fits the first XMM-Newton observation revolution 0078, this combination should reproduce the observable changes of the other XMM-Newton observations, just by varying the observed latitude of the hot spots (but keeping size, temperature and temperature profile) according to the wobble angle.

The possible combinations that fit the observation revolution 0078 are explored using a Monte Carlo simulation for the inclination angles from $i = 20^\circ$ to $i = 135^\circ$ for each temperature profile. The inclination values are incremented with 10° step size. For each inclination and temperature distribution up to 10^5 runs were performed and those geometrical properties were stored, that fit the observed temperature (difference less than the measured

6. MODELLING A FREE PRECESSING NEUTRON STAR

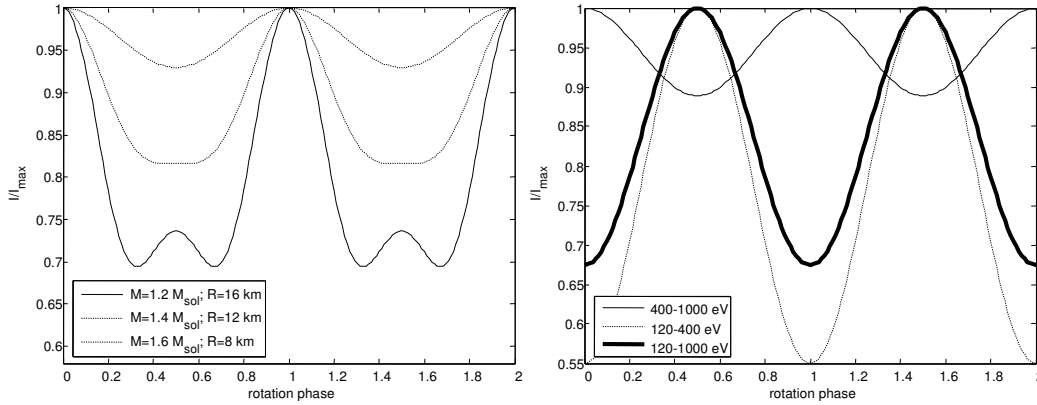


Figure 6.4: Left: Synthetic light curve of a rotating sphere with two antipodal hot spots for different values of the compactness. The rotation axis is seen under the inclination $i = 80^\circ$ and the angle between spot centre and rotation axis amounts $\theta = 20^\circ$. The temperature distribution is “magnetic” ($T_1 = 100 \text{ eV}$ and $T_2 = 90 \text{ eV}$). Note that for small values of the compactness the hump of the second hot spot can be seen explicitly.

Right: Synthetic light curve of a rotating sphere with two antipodal hot spots for different energy bands seen from 90° inclination. Here, $M = 1.4 M_{\odot}$, $R = 10 \text{ km}$ and $\theta = 20^\circ$. The properties of the two hot spots have extreme different values ($T_1 = 150 \text{ eV}$ and $T_2 = 80 \text{ eV}$, $\Xi_1 = 5^\circ$ and $\Xi_2 = 30^\circ$) and dominate the light curve in the three energy bands differently. The temperature profile is Gaussian.

error), pulsed fraction and Fourier coefficients ($\chi^2/d.o.f.$ less than the value of the observed light curves) of the hard band. Although a Monte Carlo simulation is not effective, it avoids to fit a local minimum and the code is fast enough to perform 10^5 runs within one or two days (single core CPU), depending on spot size and temperature distribution, on an ordinary machine. All runs were performed for a fixed compactness ($M = 1.4 M_{\odot}$ and $R = 10 \text{ km}$) with 40 time steps within a rotation cycle and a surface grid of $5^\circ \times 5^\circ$ size.

The number of combinations of the geometrical properties that fit revolution 0078 strongly depends on the inclination: out of 6.5×10^4 runs, 450 fit combinations are found for $i = 90^\circ$, but only 150 for $i = 50^\circ$. The system of suitable parameters is highly degenerated, e.g. a large spot size smooths the light curve and raises the temperature. This can be compensated for by a lower central temperature and a different spot location. A distribution of possible combinations of the geometrical properties of RX J0720.4–3125 (for $i = 80^\circ$) is shown in figure 6.8. If the inclination is significantly less than $i = 80^\circ$ and $\theta \approx 10^\circ - 20^\circ$, the properties of the second (cooler and larger) hot spot become less restricted because it is seen only partly, while the properties of the hotter spot become more fixed. Some combinations of the geometrical properties that fit e.g. $i = 80^\circ$ for revolution 0078 also fit values around $i = 75^\circ$ or $i = 85^\circ$ (even for a higher resolved surface grid, e.g. $1^\circ \times 1^\circ$) as well as the observations revolution 0533 and 0534, since the temperatures of these observations are not much different.

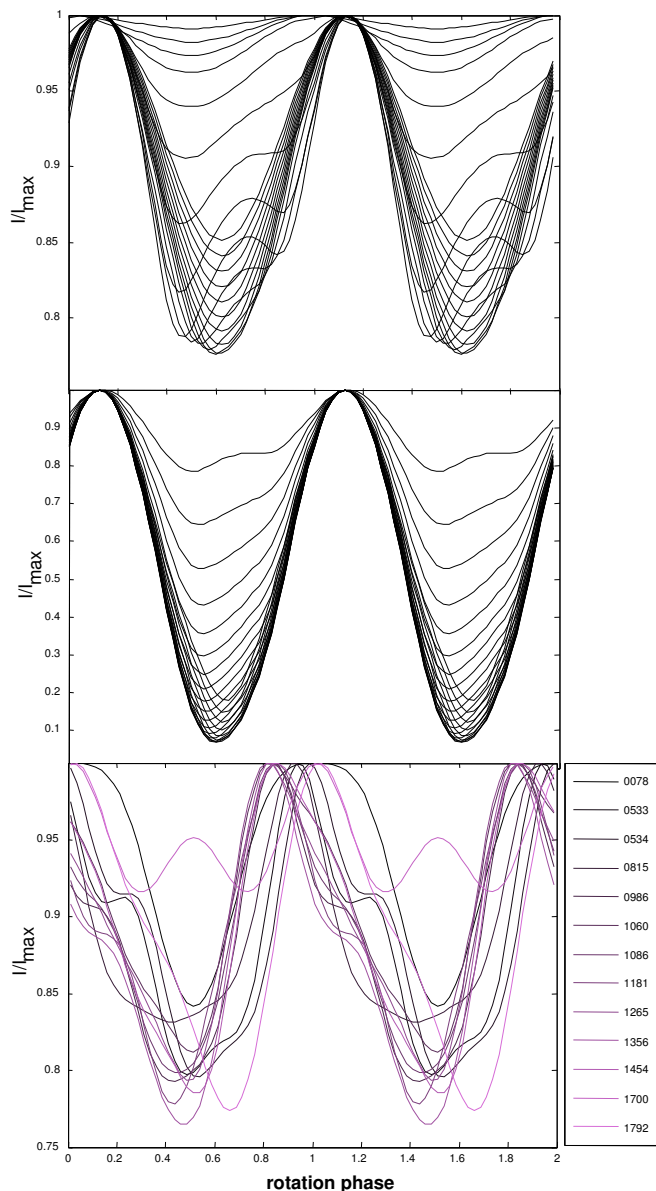


Figure 6.5: Synthetic light curves of a rotating sphere with two antipodal hot spots in the hard band (400 – 1000 eV) compared to the light curves of RX J0720.4–3125.

Upper panel: Light curves for variable inclination between 0° (light curve with highest pulsed fraction) and 110° (light curves with lowest pulsed fraction) that could be caused by bound precession. The light curves are obtained for $M = 1.4 M_\odot$, $R = 10$ km, $\theta = 5^\circ$, $T_1 = 120$ eV and $T_2 = 85$ eV, $\Xi_1 = 10^\circ$ and $\Xi_2 = 30^\circ$, $\phi_{off} = 120^\circ$ using an uniform temperature profile.

Middle panel: Light curves obtained for the same geometry as in the upper panel, but for constant inclination ($i = 50^\circ$) and variable “observed” $\theta = 5^\circ - 110^\circ$ as it would be the case of free precession (see figure 6.3) that would correspond to a wobble angle of 50° .

Lower panel: Observed light curves of RX J0720.4–3125 in the hard band for all XMM-Newton observations performed with EPIC-pn in full frame mode and thin filter (revolution numbers are listed in the legend).

6. MODELLING A FREE PRECESSING NEUTRON STAR

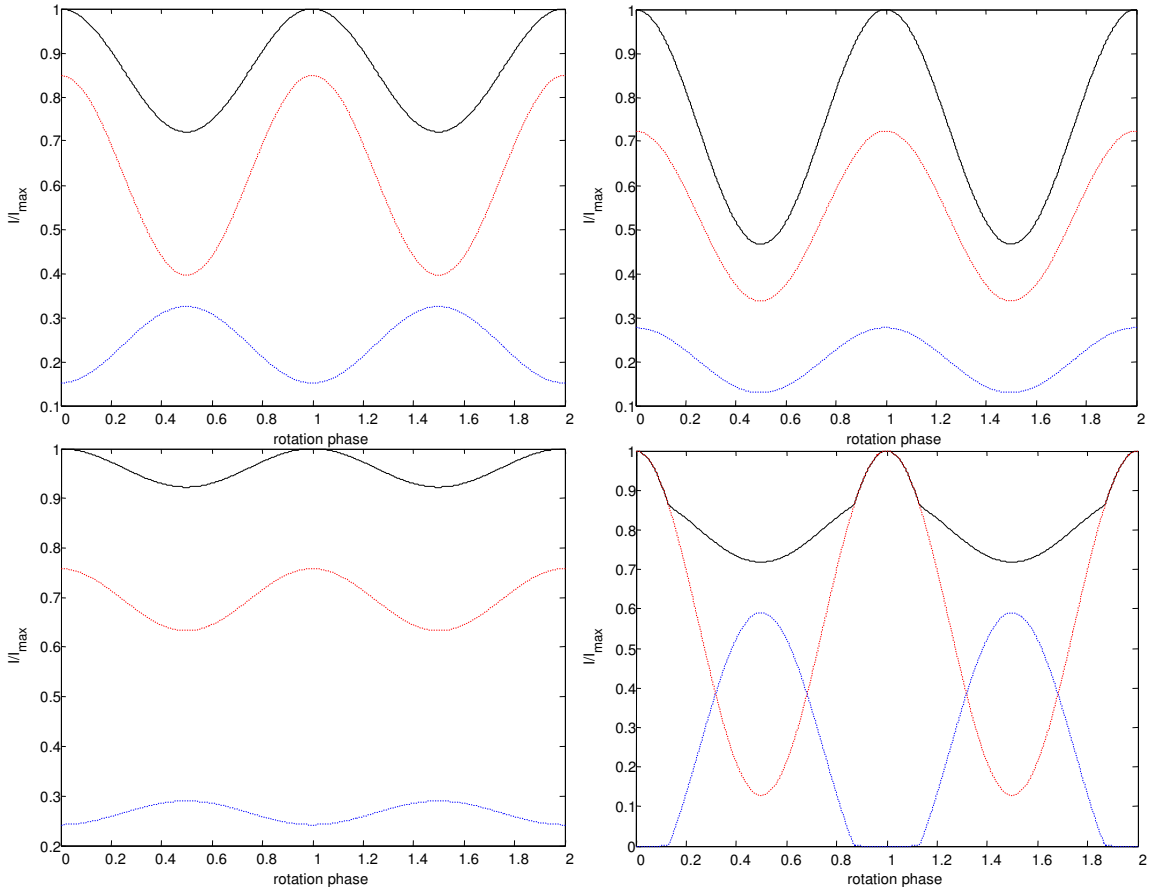


Figure 6.6: The synthetic light curves (black lines) of a rotating sphere with two different emitting hot spots (red accounts for the contribution of the hotter and smaller spot and blue from the larger and cooler spot) having a Gaussian temperature profile.

Top left: Two antipodal hot spots with the same size (radius of $\Xi = 5^\circ$), having $T_1 = 100$ eV and $T_2 = 80$ eV, respectively. The centre of the hotter spot is $\theta = 15^\circ$ inclined from the rotation axis and the view angle (inclination) is $i = 90^\circ$. The neutron star mass corresponds to $M = 1.4 M_\odot$ and the radius seen from the surface is $R = 10$ km.

Top right: The same as previously, but the cooler hot spot is shifted by $\phi_{off} = 180^\circ$ in longitude from its previous location.

Bottom left: The same as in the top left panel, but the neutron star mass corresponds to $M = 2.0 M_\odot$ and the radius seen from the surface is $R = 8$ km. Thus, due to light bending, a larger part of the surface is seen and the pulse height is lower.

Bottom right: The same as in the top left panel, but $T_1 = 100$ eV and $T_2 = 95$ eV, while the centre of the hotter spot is $\theta = 50^\circ$ inclined from the rotation axis and the inclination is $i = 70^\circ$. Note that this pulse profile significantly deviates from a pure sinusoid.

The next step was to find a wobble angle and precession period that fits all observations. This was investigated by fitting all combinations of the geometrical properties found for revolution 0078 to the other observations by fitting the changes in temperature, the light curves and calculating the phase residuals according to equation 6.5, equation 6.6 and equation 6.7. To avoid to miss one possible combination, a further Monte Carlo simulation was started simultaneously that was independent from the other combinations of the

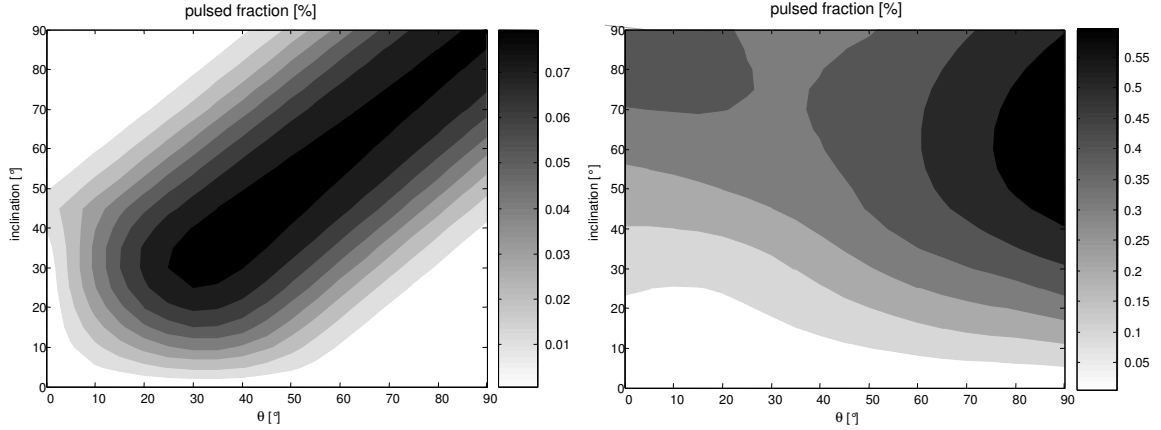


Figure 6.7: The pulsed fraction depending on the inclination and θ . The neutron star mass corresponds to $M = 1.4 M_{\odot}$ and the radius seen from the surface is $R = 10$ km.

Left: For two antipodal hot spots having both $T = 100$ eV and an angular size of $\Xi = 30^{\circ}$.

Right: For two hot spots with $T_1 = 120$ eV and $T_2 = 100$ eV. The hotter spot has an angular size of $\Xi = 15^{\circ}$ and the cooler hot spot has an angular size of $\Xi = 30^{\circ}$. The cooler hot spot is shifted by $\phi_{off} = 60^{\circ}$ in longitude and $\theta_{off} = 40^{\circ}$ in latitude from the antipodal position. In both Figures the Gaussian temperature distribution was used. See also figure 7 in [12] for comparison.

geometrical properties. The wobble angle θ_w is varied from $\theta_w = 10^{\circ}$ to $\theta_w = 65^{\circ}$, the precession period from either 5 to 10 yrs or 12 to 20 yrs.

No combination was found that fit the variable temperature, the light curves (with pulsed fraction and Fourier coefficients) and the phase residuals with one fixed set of parameters. Two main effects work contradictory: if the temperature has to change from 86 eV to 94 eV (see figure 4.4), the pulsed fraction does not stay around 11% but increases to values of about 30% and the phase residuals do not fit. If the phase residuals have fit, the temperature almost stays constant. While solutions with $i \approx 80^{\circ}$ are preferred for the best fit of the phase residuals, the temperature variations fit best with $i \approx 130^{\circ}$ for a comparable hot spot geometry and precession parameters. Generally, a smaller wobble angle is required for the Gaussian temperature profile with large differences in the central temperatures of the two hot spots and small spot sizes. However, this increases the pulsed fraction, while for an uniform temperature distribution the temperature gradient within the spots is too small (partly there is a gradient “seen” for a distant observer due to light bending) to generate large changes in the temperature without a large wobble angle (that does not obey the observed phase residuals). In the case of the magnetic temperature distribution, the temperature gradient is something in between that of the two other temperature profiles, but the additional freedom of the spot size is missing.

To account for these discrepancies, separate fits for the changes in the temperature and the phase residuals were performed. They are discussed in the following sections.

6. MODELLING A FREE PRECESSING NEUTRON STAR

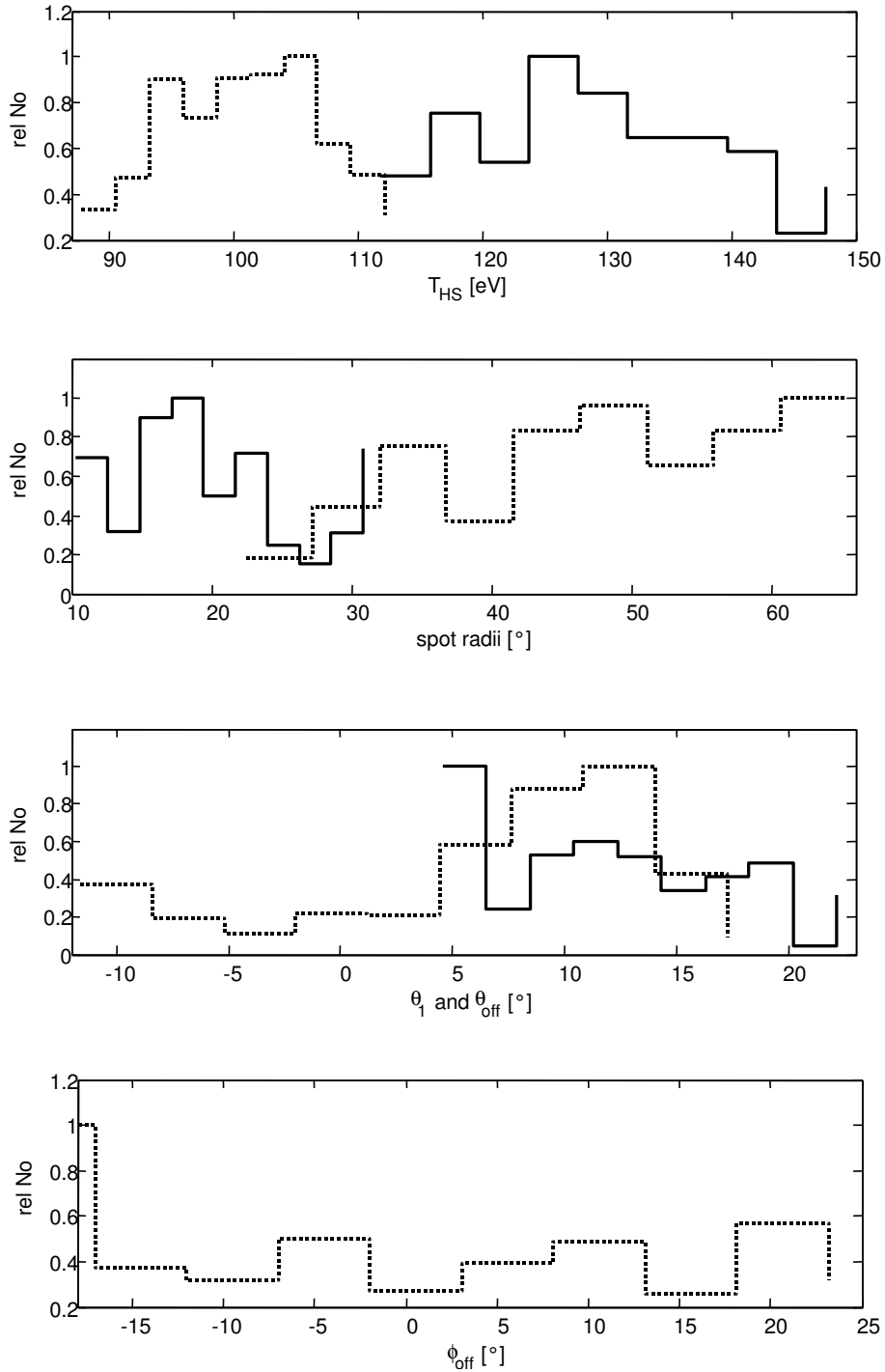


Figure 6.8: Relative number of possible geometric configurations of the hot spots on the surface of RX J0720.4–3125 that fit the observed pulse profile, pulsed fraction and temperature of the XMM-Newton observation revolution 0078 in the hard (400 – 1000 eV) band. In this case, a Gaussian temperature profile for the hot spots and an inclination of 80° was assumed. The solid line always refers to the properties of the hotter spot, while the dashed line refers to the cooler spot. The horizontal axis denotes (from top to bottom): T_{centre} ; angular size of the hot spots; angle between rotation axis and centre of the hotter spot (θ) and the angular shift (θ_{off}) in latitude from the antipodal position; angular shift (ϕ_{off}) in longitude from the antipodal position.

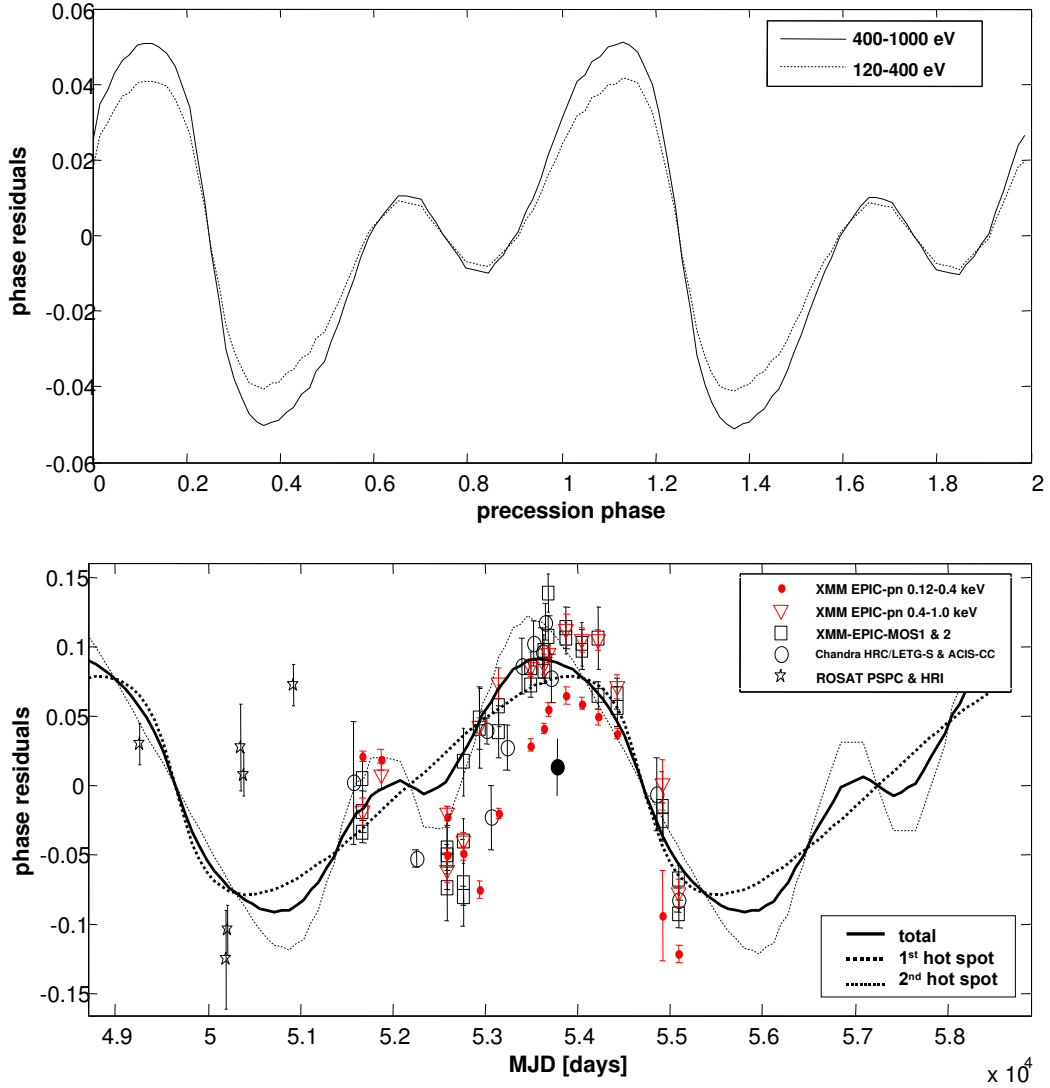


Figure 6.9: Upper panel: Phase residuals that exhibit a double hump with different size and a variable phase shift between hard and soft photons, like observed for RX J0720.4–3125. The phase residuals were obtained for the magnetic temperature profile with two antipodal hot spots, where $T_1 = 90$ eV and $T_2 = 82$ eV, $i = 90^\circ$, $\theta = 20^\circ$ and $\theta_w = 30^\circ$.

Lower panel: Best fit of the phase residuals for the XMM-Newton EPIC-pn observations (hard band) derived with $T_1 = 126$ eV and $T_2 = 101$ eV, $\Xi_1 = 17.3^\circ$ and $\Xi_2 = 34.5^\circ$, $i = 80^\circ$, $\theta = 14.9^\circ$ and $\theta_w = 27.4^\circ$. The two hot spots (Gaussian temperature profile) are not exactly antipodal, $\theta_{off} = 7.6^\circ$ and $\phi_{off} = -5.4^\circ$. The fitted precession period is 13.87 yrs. The phase residuals from figure 4.13 derived from other data are shown for orientation and were not used for the fit.

6.2.1 Fitting the phase residuals

It can be shown that various combinations of geometrical model parameters can produce a variable phase shift between hard and soft photons and two humps in the long-term trend of the phase residuals as seen from RX J0720.4–3125. Before reaching the local maximum, the hard photons lag the soft photons. Then, at the local maximum, the phase difference

6. MODELLING A FREE PRECESSING NEUTRON STAR

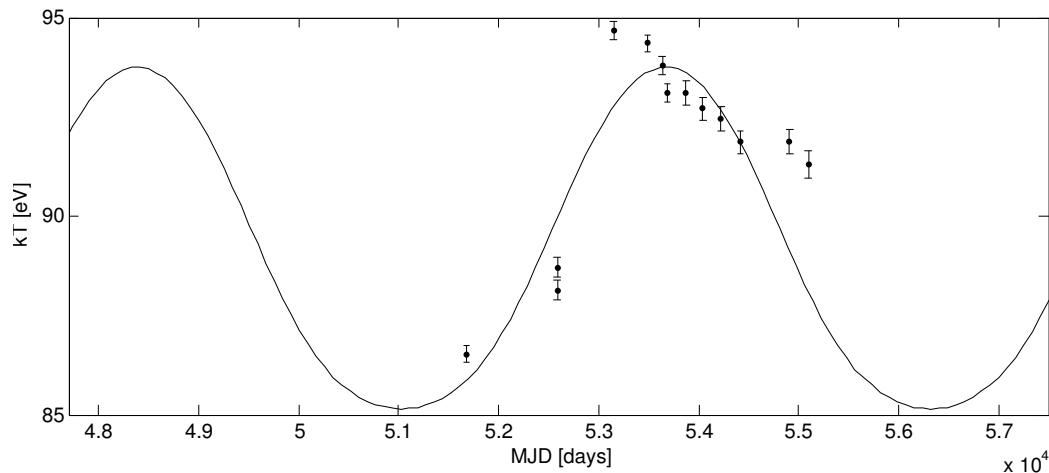


Figure 6.10: The best fit of the temperature variations of RX J0720.4–3125 using all XMM-Newton EPIC-pn data in full frame mode and thin filter, see also figure 4.1. The geometrical properties are $T_1 = 129$ eV and $T_2 = 95$ eV, $i = 136^\circ$, $\theta = 23.9^\circ$ and $\theta_w = 15.6^\circ$. The two hot spots (magnetic temperature profile) are not antipodal, $\theta_{off} = -81.4^\circ$ and $\phi_{off} = -20.1^\circ$. The precession period corresponds to 14.48 yrs.

between hard and soft photons is small. Subsequently, the soft photons lag the hard photons while the phase residuals reach their largest values (global maximum). Also the phase difference between hard and soft photons reaches the maximum at the global maximum. An example is shown in figure 6.9, upper panel. These phenomena are exactly observed from RX J0720.4–3125, when the XMM-Newton observations cover the two maxima. Only the XMM-Newton EPIC-pn instrument is sensitive enough that this variable phase shift can be observed, thus these data were used to perform a fit of the phase residuals.

The best fit yields a precession period of 13.87 yrs and is shown in figure 6.9, lower panel. Generally, all observed effects can be reproduced and the contributions of the two single hot spots vary with their visibility (i.e. precession cycle). Formally, the fit yields an unacceptable value of $\chi^2/d.o.f. = 9.2$, but equation 6.5 and equation 6.6 only account for the time delay and disregard geometrical effects in the light curve, like shown in figure 6.4 right panel, when a different view on the neutron star leads to different contributions of the two hot spots in the light curves that change the location of the light curve maximum. The contribution of this effect cannot exactly be evaluated for the case of RX J0720.4–3125 (since the true emission geometry is still unknown), but an estimate based on the geometrical properties used for the fit in figure 6.9 yields that $\chi^2/d.o.f.$ can be up to a factor of five smaller, if this effect is taken into account. Moreover, the presence of spin-down torques [2] degrades the fit. Thus, free precession easily explains the timing behaviour of RX J0720.4–3125. However, the geometrical properties used for the fit in figure 6.9 generate almost no variations in the temperature.

6.2.2 Fitting the temperature variations

No combinations of geometrical model parameters could be found that reproduce the observed temperature variations. In all simulated cases, the temperature variations are sinusoidal, except if the offset of the second hot spot from the antipodal position is large, a double sine variation with maxima of different heights can be created. If the two hot spots are almost at the same location and have different properties, if the inclination is larger than 100° and the wobble angle is twice the value of θ , the temperature does not vary sinusoidal, but still differs much from the observed variations. Even the best fits, using the temperatures obtained with XMM-Newton EPIC-pn data in full frame mode and thin filter, yield $\chi^2/d.o.f. \geq 30$, see figure 6.10. In each case, the temperature undergoes changes of a few eV, the pulsed fraction reaches too large values and the light curves cannot be fitted properly.

The temperature profiles discussed in section 6.1.2.2 allow minimum temperatures around $T(\xi) = 0$ eV (the X-ray data is not sensitive to temperatures below ≈ 30 eV), for the uniform temperature distribution outside the spot and for the other two distributions if the surface element is located far enough from the spot center. Likely, this is not the case for RX J0720.4–3125 and may account for the incoherency of the simulated temperature variations with the pulsed fraction and the phase residuals. Thus, the temperature profiles were modified. In the case of the uniform temperature distribution, the surface temperature was set to $T_{surf} > 0$ eV outside the spot (if $\xi > \Xi$). For the Gaussian temperature profile $T(\xi) = T_{surf}$ if $\xi > \Xi$ as well, but if $T(\xi) < T_{surf}$ within the spot (for large T_{surf} and small T_0), $T(\xi)$ was set to T_{surf} . This reduces the effective size of the spot, but avoids the appearance of a cold ring around the spot (that might be non-physical). For the magnetic temperature profile $T(\xi)$ was set to T_{surf} , if $T(\xi) < T_{surf}$.

In advance to start a new simulation, different values of T_{surf} up to 80 eV were tested. The surface area of the spots is at least one order of magnitude smaller than the rest of the surface, i.e. large surface temperatures significantly influence the spectrum. Only if roughly $T_{surf} < 25$ eV, the new simulations yield values of $\chi^2/d.o.f.$ not much larger than the values obtained from the previous simulations.

With the modified temperature profiles, some emission geometries were found that produce non-sinusoidal temperature variations (also with almost the required amplitude) while producing large phase residuals. The phase residuals reach their maximum when the temperature variation reaches its maximum, like observed for RX J0720.4–3125. However, the trend of the phase residuals is not double-humped and the trend of the simulated temperatures has a much different morphology than the observed one. The simulated light curves do not fit with the observed, but the pulsed fraction varies within 15 – 20% (8 – 12% for RX J0720.4–3125). These simulations again yield a precession period of 13–14 yrs. The

6. MODELLING A FREE PRECESSING NEUTRON STAR

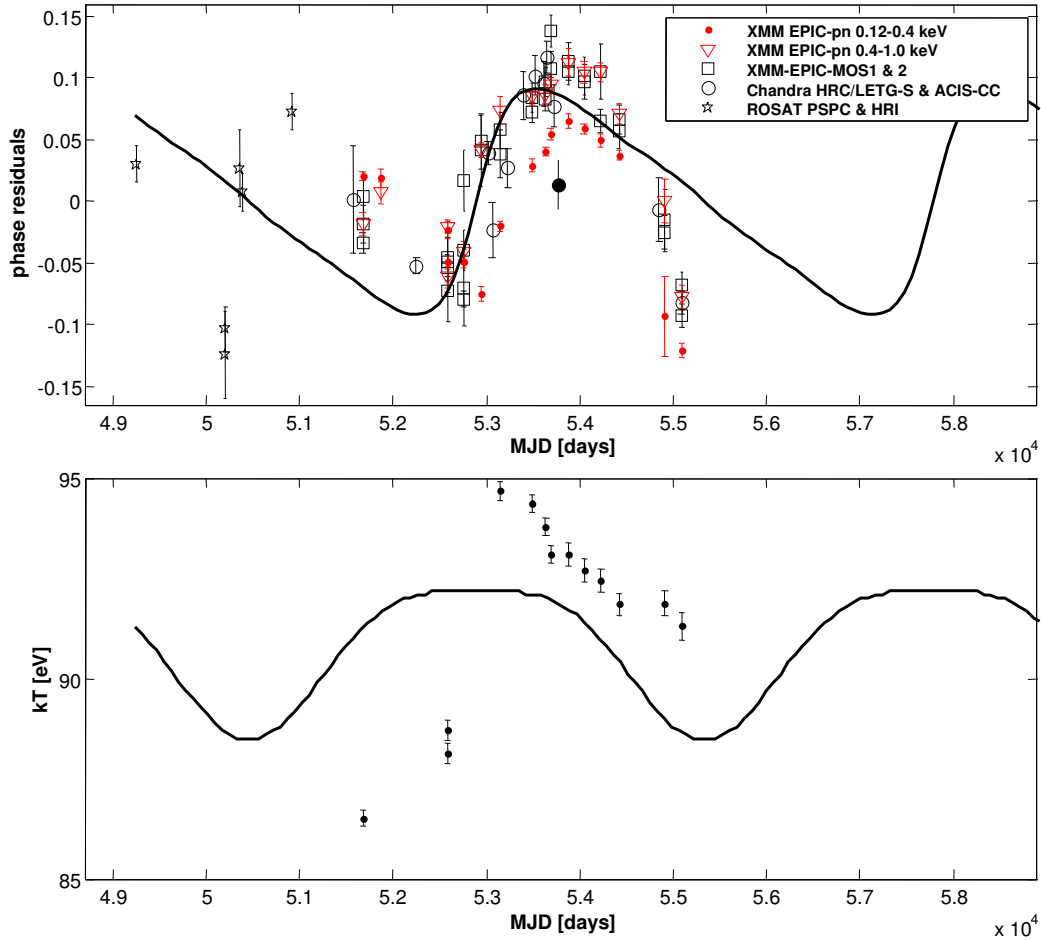


Figure 6.11: Simultaneously fitted temperature variations and phase residuals of RX J0720.4–3125 using all XMM-Newton EPIC-pn data in full frame mode and thin filter, see also figure 6.9 and figure 6.10. The geometrical properties are $T_1 = 120$ eV and $T_2 = 86$ eV, $i = 27.5^\circ$, $\theta = 45.5^\circ$ and $\theta_w = 18.3^\circ$. The two hot spots (Gaussian temperature profile) are not antipodal, $\theta_{off} = 24^\circ$ and $\phi_{off} = 26.6^\circ$. The precession period corresponds to 13.47 yrs. The surface temperature $T_{surf} = 10$ eV. This emission geometry does not fit the data, but shows qualitative trends observed for RX J0720.4–3125.

required wobble angles were $\theta_w \approx 20^\circ$, i.e. not much different from that in figure 6.9 and figure 6.10, but the inclination values were $\approx 30^\circ$. Although these emission geometries do not lead to acceptable fits ($\chi^2/d.o.f. \approx 30$, see figure 6.11), they roughly reproduce the qualitative variations of RX J0720.4–3125.

7

Summary

In this thesis, the most recent X-ray observations of RX J0720.4–3125 were included in the spectral and timing analysis and it could be shown that the spectral variations exhibited in the XMM-Newton EPIC-pn data do not continue the sinusoidal trend (figure 4.1) as seen in earlier work [41]. Independent of the applied timing solution, RX J0720.4–3125 exhibits a significant variable phase lag between hard (400 – 1000 eV) and soft (120 – 400 eV) photons. This can only be observed with XMM-Newton EPIC-pn, since this instrument has the required sensitivity and quality in the two energy bands. The results are published in [51].

Based on new XMM-Newton and Chandra observations and including archival data, a new phase coherent timing solution for RX J0720.4–3125 was derived. The phase residuals seem to follow a periodic pattern. Including ROSAT data, probably more than one cycle of this long term period is covered by observations. However, the ROSAT data are ambiguous, since they suffer from a low number of photons compared to the observations performed with Chandra and XMM-Newton. The phase residuals from the different telescopes, instruments and setups are in best agreement, when the hard band is used for the phase coherent timing solution. The results of the updated timing solution were confirmed with the Z_n^2 test and published in [52].

From co-added Chandra LETG and XMM-Newton RGS high resolution spectra, three narrow absorption features were identified. An absorption feature around 0.57 keV was found by [44]. This absorption feature could be confirmed including most recent RGS data. Two further absorption features were identified in the co-added Chandra HRC-S/LETG data, that are not detected in the co-added RGS spectra (the RGS1 detector has strong intrinsic features at these energies, see figure 4.3 and section 4.1).

A model of a precessing sphere with two hot spots on its surface dealing with three different temperature distributions was used to simulate the spectral and temporal variations of RX J0720.4–3125. While the trend of the phase residuals and the variable phase lag be-

7. SUMMARY

tween hard and soft photons can be reproduced with a 14 yrs long term period, the model did not reproduce the observed changes in the temperature. No combination of geometrical properties was found that fits the changes in the temperature, the timing behaviour and the variable shape of the light curves simultaneously. The reason might be that either the assumed temperature profiles are too simple and/or do not reflect the true distribution, or the emission is highly non-isotropic (see section 6.1.2.1). The shape of the spots is unknown, the variable equivalent width of the broad absorption feature (not modelled in this work) affects the shape of the light curves and the contribution of spin-down torques to the phase residuals may not be negligible. Since the current model explains most of the spectral and temporal properties observed for RX J0720.4–3125 (some qualitatively), a more advanced and detailed model is in progress and may deliver a final explanation.

8

Conclusions and outlook

From the hypotheses discussed in chapter 5, only precession (free or bound, or triggered by Tkachenko waves) is suitable to explain a variable phase gap between hard and soft photons (orbital motion leads to phase residuals, but not to variable phase gaps between two bands). Even if a glitch formally better fits the phase residuals (see section 5.1.2) than a sinusoid, an $\text{abs}(\text{sine})$ (figure 5.1) or the phase residuals generated from the model of a precessing neutron star (figure 6.9), the variable phase gap between hard and soft photons is a key issue that is clearly observed and has to be explained. The bad fit of a sine or an $\text{abs}(\text{sine})$ function to the phase residuals of RX J0720.4–3125 indicates that such an approximation is too simple. Indeed, the simulations show that a sinusoidal trend in the phase residuals is a special case and occurs exceptionally (see equation 6.5 and equation 6.6). Qualitatively, the trend in the phase residuals and the phase lag between hard and soft photons can be explained by the precession model, e.g. see figure 6.9.

However, the model of a free precessing neutron star does not sufficiently explain the spectral variations. It was not possible to generate a large change in the temperature of $\approx 8 \text{ eV}$, as it has been observed in the XMM-Newton EPIC-pn data, while keeping the pulsed fraction between 8% and 12%. There may be at least three reasons for this: First, the temperature profile of the neutron star surface is different to that assumed in the simulations (i.e. different from uniform, Gaussian or “magnetic”, see figure 6.2). Varying the temperature profile influences the pulsed fraction and the wobble angle required to produce the relatively large variations in the observed temperature. Since the true temperature profile of an X-ray pulsar is still speculative, see [1; 32; 33; 35; 101; 148], it might be likely that the temperature profile of RX J0720.4–3125 is very different from the assumed temperature profiles. Second, the hot spots may not have a circular shape, but they can be elliptic or they are composed of numerous smaller spots – like sometimes observed for Solar spots. Third, the hot spots change their location and move with respect to the surface while the neutron star is precessing (or the moving spots mimic precession).

8. CONCLUSIONS AND OUTLOOK

For the model of free precession, the data are best fitted with a long term period of ≈ 14 yrs that yields an ellipticity of the neutron star of $\epsilon \approx 2 \times 10^{-8}$. Elliptic neutron stars may contribute to the detectable gravitational wave background (i.e. fast spinning, non-spheric compact objects). The existence of a long term precessing neutron star imposes some limits on the superfluid interior, hence on the equation of state, see e.g. [5; 78; 79].

From observations, free precession and bound precession are hardly to distinguish. Bound precession requires another compact object orbiting around RX J0720.4–3125. Out of roughly 2000 known radio pulsars, only nine double neutron stars are known [118], i.e. the probability to observe a double neutron star (or neutron star/ black hole) among the M7 is only 0.03.¹

Precession (no matter how it is caused) or orbital motion leave periodic patterns in the spectral and temporal variation, i.e. can be confirmed only by continued observations. The monitoring with X-ray telescopes is still ongoing (thanks to Chandra GTO time of the MPE and own XMM-Newton observations), but does not cover a sufficiently long time interval. If the long term periodicity is confirmed, free precession is strongly favoured – if not, a glitch might be a likely explanation. The presence of a disk or a companion will be checked soon with the Spitzer telescope [106].

Since the spectral changes and the timing behaviour are incompatible in the model, introduced in chapter 6, there is still the possibility that the spectral variations and the timing behaviour of RX J0720.4–3125 have a different origin caused by other effects. The observations available for this thesis are still not numerous enough to draw a final conclusion, but free precession seems to be the most likely explanation.

The narrow absorption features detected in the co-added XMM-Newton RGS and Chandra HRC-S/LETG spectra point to an overabundance of oxygen in the line of sight to RX J0720.4–3125. This might be an evidence for the presence of a circumstellar disk. At least one of these lines exhibits a reasonable gravitational redshift. A circumstellar disk may account for some observed peculiarities of RX J0720.4–3125. Hence, the other M7 have to be investigated for the existence of a circumstellar disk and/or for narrow absorption features in their co-added XMM-Newton RGS and Chandra HRC-S/LETG spectra to derive useful conclusions about the interaction between the M7 and their environment. However, this is currently not possible for most of the M7 since they are observed not frequent and long enough to detect such weak lines.

¹nine double neutron stars/ 2000 radio pulsars = 4.5×10^{-3} , i.e. 0.03 such objects among the M7.

References

- [1] D. N. AGUILERA, J. A. PONS, AND J. A. MIRALLES. **The Impact of Magnetic Field on the Thermal Evolution of Neutron Stars.** *ApJ*, **673**:L167–L170, February 2008. 74, 89
- [2] T. ARGÜN, B. LINK, AND I. WASSERMAN. **Precession of the isolated neutron star PSR B1828-11.** *MNRAS*, **365**:653–672, January 2006. 76, 84
- [3] M. A. ALPAR. **On Disks and Magnetars: After the Discovery of a Fallback Disk.** In *ESA Special Publication*, **622** of *ESA Special Publication*, pages 541–+, 2007. 63
- [4] M. A. ALPAR, A. ANKAY, AND E. YAZGAN. **Pulsar Spin-down by a Fallback Disk and the P-P Diagram.** *ApJ*, **557**:L61–L65, August 2001. 63
- [5] M. A. ALPAR AND J. A. SAULS. **On the dynamical coupling between the superfluid interior and the crust of a neutron star.** *ApJ*, **327**:723–725, April 1988. 58, 90
- [6] D. E. BACKMAN AND F. PARESC. **Main-sequence stars with circumstellar solid material - The VEGA phenomenon.** In E. H. LEVY & J. I. LUNINE, editor, *Protostars and Planets III*, pages 1253–1304, 1993. 65
- [7] A. BAUSWEIN, H. - JANKA, R. OECHSLIN, G. PAGLIARA, I. SAGERT, J. SCHAFFNER-BIELICH, M. M. HOHLE, AND R. NEUHAEUSER. **Mass Ejection by Strange Star Mergers and Observational Implications.** *ArXiv e-prints*, December 2008. 6
- [8] A. BAUSWEIN, R. OECHSLIN, AND H.-T. JANKA. **Discriminating strange star mergers from neutron star mergers by gravitational-wave measurements.** *Phys. Rev. D*, **81**(2):024012–+, January 2010. 6
- [9] A. BAYKAL, M. J. STARK, AND J. SWANK. **Discovery of the Orbit of the Transient X-Ray Pulsar SAX J2103.5+4545.** *ApJ*, **544**:L129–L132, December 2000. 65
- [10] A. M. BELOBORODOV. **Gravitational Bending of Light Near Compact Objects.** *ApJ*, **566**:L85–L88, February 2002. 72, 73, 76
- [11] O. BLAES AND P. MADAU. **Can we observe accreting, isolated neutron stars?** *ApJ*, **403**:690–705, February 1993. 9
- [12] S. BOGDANOV, J. E. GRINDLAY, AND G. B. RYBICKI. **Thermal X-Rays from Millisecond Pulsars: Constraining the Fundamental Properties of Neutron Stars.** *ApJ*, **689**:407–415, December 2008. 76, 81
- [13] R. BUCCHERI, K. BENNETT, G. F. BIGNAMI, J. B. G. M. BLOEMEN, V. BORIAKOFF, P. A. CARAVEO, W. HERMSEN, G. KANBACH, R. N. MANCHESTER, J. L. MASNOU, H. A. MAYER-HASSELWANDER, M. E. OZEL, J. A. PAUL, B. SACCO, L. SCARSI, AND A. W. STRONG. **Search for pulsed gamma-ray emission from radio pulsars in the COS-B data.** *A&A*, **128**:245–251, November 1983. 31
- [14] E. W. BURKE, JR., W. W. ROLLAND, AND W. R. BOY. **A Photoelectric Study of Magnetic Variable Stars.** *JRASC*, **64**:353–+, December 1970. 32
- [15] V. BURWITZ, F. HABERL, R. NEUHÄUSER, P. PREDEHL, J. TRÜMPER, AND V. E. ZAVLIN. **The thermal radiation of the isolated neutron star RX J1856.5-3754 observed with Chandra and XMM-Newton.** *A&A*, **399**:1109–1114, March 2003. 10, 11, 45, 47
- [16] V. BURWITZ, V. E. ZAVLIN, R. NEUHÄUSER, P. PREDEHL, J. TRÜMPER, AND A. C. BRINKMAN. **The Chandra LETGS high resolution X-ray spectrum of the isolated neutron star RX J1856.5-3754.** *A&A*, **379**:L35–L38, November 2001. 9, 10, 45, 47
- [17] W. CASH. **Parameter estimation in astronomy through application of the likelihood ratio.** *ApJ*, **228**:939–947, March 1979. 31
- [18] J. COTTAM, F. PAERELS, AND M. MENDEZ. **Gravitationally redshifted absorption lines in the X-ray burst spectra of a neutron star.** *Nature*, **420**:51–54, November 2002. 9
- [19] M. CROPPER, F. HABERL, S. ZANE, AND V. E. ZAVLIN. **Timing analysis of the isolated neutron star RX J0720.4-3125 revisited.** *MNRAS*, **351**:1099–1108, July 2004. 10, 18, 32, 36, 52, 98
- [20] M. CROPPER, S. ZANE, G. RAMSAY, F. HABERL, AND C. MOTCH. **Modelling the spin pulse profile of the isolated neutron star RX J0720.4-3125 observed with XMM-Newton.** *A&A*, **365**:L302–L307, January 2001. 10, 12
- [21] L.P. DAVID, JR. F.R. HARNDEN, K.E. KEARNS, AND M.V. ZOMBECK. *The ROSAT High Resolution Imager (HRI), USRSDC/SAO Calibration Report, revised*, 1996. 17
- [22] C. P. DE VRIES, J. VINK, M. MÉNDEZ, AND F. VERBUNT. **Long-term variability in the X-ray emission of RX J0720.4-3125.** *A&A*, **415**:L31–L34, February 2004. 10, 12, 14, 33, 49, 57
- [23] J. W. DEN HERDER, A. C. BRINKMAN, S. M. KAHN, G. BRANDUARDI-RAYMONT, K. THOMSEN, H. AARTS, M. AUDARD, J. V. BIXLER, A. J. DEN BOGGENDE, J. COTTAM, T. DECKER, L. DUBBELDAM, C. ERD, H. GOULOZE, M. GÜDEL, P. GUTTRIDGE, C. J. HAILEY, K. A. JANABI, J. S. KAASTRA, P. A. J. DE KORTE, B. J. VAN LEEUWEN, C. MAUCHE, A. J. MCCALDEN, R. MEWE, A. NABER, F. B. PAERELS, J. R. PETERSON, A. P. RASMUSSEN, K. REES, I. SAKELIIOU, M. SAKO, J. SPODEK, M. STERN, T. TAMURA, J. TANDY, C. P. DE VRIES, S. WELCH, AND A. ZEHNDER. **The Reflection Grating Spectrometer on board XMM-Newton.** *A&A*, **365**:L7–L17, January 2001. 21, 41
- [24] D. DEWEY. **Subassembly Calibration: HETG.** *Chandra News*, **4**:11–+, September 1996. 25
- [25] D. DEWEY. **HETG Spectra.** *Chandra News*, **5**:18–+, December 1997. 25
- [26] J. J. DRAKE, H. L. MARSHALL, S. DREIZLER, P. E. FREEMAN, A. FRUSCIONE, M. JUDA, V. KASHYAP, F. NICASTRO, D. O. PEASE, B. J. WARGELIN, AND K. WERNER. **Is RX J1856.5-3754 a Quark Star?** *ApJ*, **572**:996–1001, June 2002. 9
- [27] M. M. DWORETSKY. **A period-finding method for sparse randomly spaced observations of 'How long is a piece of string?'** *MNRAS*, **203**:917–924, June 1983. 33, 34
- [28] T. EISENBEISS, C. GINSKI, M. M. HOHLE, V. V. HAMBARYAN, R. NEUHÄUSER, AND T. O. B. SCHMIDT. **New photometry and astrometry of the isolated neutron star RX J0720.4-3125 using recent VLT/FORS observations.** *Astronomische Nachrichten*, **331**:243–+, 2010. 10, 11, 64
- [29] K. Y. EKŞİ AND M. A. ALPAR. **Disks Surviving the Radiation Pressure of Radio Pulsars.** *ApJ*, **620**:390–397, February 2005. 65
- [30] N. R. EVANS. **LETG Order Separation.** *Chandra News*, **5**:16–+, December 1997. 25

REFERENCES

- [31] G. P. GARMIRE, M. W. BAUTZ, P. G. FORD, J. A. NOUSEK, AND G. R. RICKER, JR. **Advanced CCD imaging spectrometer (ACIS) instrument on the Chandra X-ray Observatory.** In J. E. TRUMPER & H. D. TANANBAUM, editor, *Society of Photo-Optical Instrumentation Engineers (SPIE) Conference Series*, 4851 of *Society of Photo-Optical Instrumentation Engineers (SPIE) Conference Series*, pages 28–44, March 2003. 25
- [32] U. GEPPERT, M. KÜKER, AND D. PAGE. **Temperature distribution in magnetized neutron star crusts.** *A&A*, 426:267–277, October 2004. 74, 89
- [33] U. GEPPERT, M. KÜKER, AND D. PAGE. **Temperature distribution in magnetized neutron star crusts. II. The effect of a strong toroidal component.** *A&A*, 457:937–947, October 2006. 74, 89
- [34] K. GLAMPEDAKIS, N. ANDERSSON, AND D. I. JONES. **Do superfluid instabilities prevent neutron star precession?** *MNRAS*, 394:1908–1924, April 2009. 16
- [35] G. GREENSTEIN AND G. J. HARTKE. **Pulselike character of blackbody radiation from neutron stars.** *ApJ*, 271:283–293, August 1983. 74, 89
- [36] H. GRIGORIAN, D. BLASCHKE, AND D. VOSKRESENSKY. **Cooling of neutron stars with color superconducting quark cores.** *Phys. Rev. C*, 71(4):045801–+, April 2005. 8
- [37] M. E. GUSAKOV, A. D. KAMINKER, D. G. YAKOVLEV, AND O. Y. GNEDIN. **The cooling of Akmal-Pandharipande-Ravenhall neutron star models.** *MNRAS*, 363:555–562, October 2005. 6, 8
- [38] F. HABERL. **The magnificent seven: magnetic fields and surface temperature distributions.** *Ap&SS*, 308:181–190, April 2007. 2, 10, 12, 14, 15, 17, 21, 34
- [39] F. HABERL, C. MOTCH, D. A. H. BUCKLEY, F.-J. ZICKGRAF, AND W. PIETSCH. **RXJ0720.4-3125: strong evidence for an isolated pulsating neutron star.** *A&A*, 326:662–668, October 1997. 10, 11
- [40] F. HABERL, C. MOTCH, V. E. ZAVLIN, K. REINSCH, B. T. GÄNSICKE, M. CROPPER, A. D. SCHWOPE, R. TUROLLO, AND S. ZANE. **The isolated neutron star X-ray pulsars RX J0420.0-5022 and RX J0806.4-4123: New X-ray and optical observations.** *ā*, 424:635–645, September 2004. 11
- [41] F. HABERL, R. TUROLLO, C. P. DE VRIES, S. ZANE, J. VINK, M. MÉNDEZ, AND F. VERBUNT. **Evidence for precession of the isolated neutron star $\dot{\iota}$ ASTROBJ $\dot{\iota}$ RX J0720.4-3125 $\dot{\iota}$ /ASTROBJ $\dot{\iota}$.** *A&A*, 451:L17–L21, May 2006. 10, 11, 12, 13, 14, 21, 24, 33, 36, 37, 38, 39, 41, 44, 45, 47, 49, 57, 67, 68, 87
- [42] F. HABERL AND V. E. ZAVLIN. **XMM-Newton observations of the isolated neutron star RX J0806.4-4123.** *A&A*, 391:571–576, August 2002. 11
- [43] F. HABERL, V. E. ZAVLIN, J. TRÜMPER, AND V. BURWITZ. **A phase-dependent absorption line in the spectrum of the X-ray pulsar RX J0720.4-3125.** *A&A*, 419:1077–1085, June 2004. 10, 11, 12, 13, 21, 24, 33, 36, 37, 39, 41, 44, 45, 47, 48, 57
- [44] V. HAMBARYAN, R. NEUHÄUSER, F. HABERL, M. M. HOHLE, AND A. D. SCHWOPE. **XMM-Newton RGS spectrum of RX J0720.4-3125: an absorption feature at 0.57 keV.** *A&A*, 497:L9–L12, April 2009. 41, 42, 44, 45, 46, 63, 64, 65, 87
- [45] C. O. HEINKE, G. B. RYBICKI, R. NARAYAN, AND J. E. GRINDLAY. **A Hydrogen Atmosphere Spectral Model Applied to the Neutron Star X7 in the Globular Cluster 47 Tucanae.** *ApJ*, 644:1090–1103, June 2006. 37
- [46] A. HEWISH, S. J. BELL, J. D. H. PILKINGTON, P. F. SCOTT, AND R. A. COLLINS. **Observation of a Rapidly Pulsating Radio Source.** *Nature*, 217:709–713, February 1968. 1
- [47] R. HIRATA AND T. HORAGUCHI. **Atomic spectral lines list.** *Department of Astronomy, Faculty of Science, Kyoto University and National Science Museum*, 1995. 64
- [48] W. C. G. HO. **Constraining the geometry of the neutron star RX J1856.5-3754.** *MNRAS*, 380:71–77, September 2007. 65
- [49] M. HOHLE. **RX J0720 evolution: precession, glitching, or the last flutterings of a magnetar.** In *XMM-Newton Proposal ID #06011701*, pages 26–+, October 2008. 24
- [50] M. HOHLE. **RX J0720.4-3125 - a free precessing X-ray pulsar?** In *XMM-Newton Proposal ID #06509201*, pages 28–+, October 2009. 24
- [51] M. M. HOHLE, F. HABERL, J. VINK, R. TUROLLO, V. HAMBARYAN, S. ZANE, C. P. DE VRIES, AND M. MÉNDEZ. **Spectral and temporal variations of the isolated neutron star RX J0720.4-3125: new XMM-Newton observations.** *A&A*, 498:811–820, May 2009. 10, 11, 33, 34, 36, 37, 39, 41, 44, 45, 47, 57, 68, 87
- [52] M. M. HOHLE, F. HABERL, J. VINK, R. TUROLLO, S. ZANE, C. P. DE VRIES, AND M. MÉNDEZ. **Updated phase coherent timing solution of the isolated neutron star RX J0720.4-3125 using recent XMM-Newton and Chandra observations.** *ArXiv e-prints*, July 2010. 49, 68, 87
- [53] R. A. HULSE AND J. H. TAYLOR. **Discovery of a pulsar in a binary system.** *ApJ*, 195:L51–L53, January 1975. 1
- [54] F. JANSEN, D. LUMB, B. ALTIERI, J. CLAVEL, M. EHLE, C. ERD, C. GABRIEL, M. GUAINAZZI, P. GONDOIN, R. MUCH, R. MUNOZ, M. SANTOS, N. SCHARTEL, D. TEXIER, AND G. VACANTI. **XMM-Newton observatory. I. The spacecraft and operations.** *A&A*, 365:L1–L6, January 2001. 18
- [55] G. H. JANSSEN AND B. W. STAPPERS. **30 glitches in slow pulsars.** *A&A*, 457:611–618, October 2006. 15
- [56] S. JOHNSTON. **Radio observations of two isolated neutron stars: RX J0720.4 - 3125 and RX J0806.4 - 4132.** *MNRAS*, 340:L43–L46, April 2003. 8
- [57] D. I. JONES AND N. ANDERSSON. **Gravitational waves from freely precessing neutron stars.** *MNRAS*, 331:203–220, March 2002. 58, 61
- [58] J. JUDA. **LETG Spectra.** *Chandra News*, 5:20–+, December 1997. 25
- [59] M. JUDA. **Subassembly Calibration: LETG.** *Chandra News*, 4:9–+, September 1996. 25
- [60] J. S. KAASTRA, C. P. DE VRIES, E. COSTANTINI, AND J. W. A. DEN HERDER. **Effective area calibration of the reflection grating spectrometers of XMM-Newton. I. X-ray spectroscopy of the Crab nebula.** *A&A*, 497:291–310, April 2009. 45, 65
- [61] D. L. KAPLAN, S. R. KULKARNI, AND M. H. VAN KERKWIJK. **A Probable Optical Counterpart to the Isolated Neutron Star RX J1308.6+2127.** *ApJ*, 579:L29–L32, November 2002. 11
- [62] D. L. KAPLAN, S. R. KULKARNI, AND M. H. VAN KERKWIJK. **The Optical Counterpart of the Isolated Neutron Star RX J1605.3+3249.** *ApJ*, 588:L33–L36, May 2003. 11
- [63] D. L. KAPLAN AND M. H. VAN KERKWIJK. **A Coherent Timing Solution for the Nearby Isolated Neutron Star RX J0720.4-3125.** *ApJ*, 628:L45–L48, July 2005. 10, 11, 15, 30, 31, 33, 36, 48, 49, 50, 67, 68, 98
- [64] D. L. KAPLAN AND M. H. VAN KERKWIJK. **A Coherent Timing Solution for the Nearby Isolated Neutron Star RX J1308.6+2127/RBS 1223.** *ApJ*, 635:L65–L68, December 2005. 11
- [65] D. L. KAPLAN AND M. H. VAN KERKWIJK. **Constraining the Spin-down of the Nearby Isolated Neutron Star RX J0806.4-4123, and Implications for the Population of Nearby Neutron Stars.** *ApJ*, 705:798–808, November 2009. 2, 11

- [66] D. L. KAPLAN AND M. H. VAN KERKWIJK. **Constraining the Spin-down of the Nearby Isolated Neutron Star RX J0806.4-4123, and Implications for the Population of Nearby Neutron Stars.** *ArXiv e-prints*, September 2009. 2
- [67] D. L. KAPLAN AND M. H. VAN KERKWIJK. **Constraining the Spin-Down of the Nearby Isolated Neutron Star RX J2143.0+0654.** *ApJ*, 692:L62–L66, February 2009. 2, 11
- [68] D. L. KAPLAN, M. H. VAN KERKWIJK, AND J. ANDERSON. **The Parallax and Proper Motion of RX J1856.5-3754 Revisited.** *ApJ*, 571:447–457, May 2002. 9, 11
- [69] D. L. KAPLAN, M. H. VAN KERKWIJK, AND J. ANDERSON. **The Distance to the Isolated Neutron Star RX J0720.4-3125.** *ApJ*, 660:1428–1443, May 2007. 9, 10, 11
- [70] D. L. KAPLAN, M. H. VAN KERKWIJK, H. L. MARSHALL, B. A. JACOBY, S. R. KULKARNI, AND D. A. FRAIL. **The Nearby Neutron Star RX J0720.4-3125 from Radio to X-Rays.** *ApJ*, 590:1008–1019, June 2003. 9, 10
- [71] V. I. KONDRATIEV, M. A. MCLAUGHLIN, D. R. LORIMER, M. BURGAY, A. POSSENTI, R. TUROLLA, S. B. POPOV, AND S. ZANE. **New Limits on Radio Emission from X-ray Dim Isolated Neutron Stars.** *ApJ*, 702:692–706, September 2009. 8
- [72] G. KOVACS. **Frequency shift in Fourier analysis.** *Ap&SS*, 78:175–188, August 1981. 30, 32, 49
- [73] R. P. KRAFT, J. H. CHAPPELL, A. T. KENTER, K. KOBAYASHI, G. R. MEEHAN, S. S. MURRAY, M. V. ZOMBECK, G. W. FRASER, J. F. PEARSON, J. E. LEES, A. N. BRUNTON, M. BARBERA, A. COLLURA, AND S. SERIO. **Performance and calibration of the AXAF High-Resolution Camera II: the spectroscopic detector.** In O. H. SIEGMUND & M. A. GUMMIN, editor, *Society of Photo-Optical Instrumentation Engineers (SPIE) Conference Series*, 3114 of *Society of Photo-Optical Instrumentation Engineers (SPIE) Conference Series*, pages 53–73, October 1997. 25
- [74] S. R. KULKARNI AND M. H. VAN KERKWIJK. **Optical Observations of the Isolated Neutron Star RX J0720.4-3125.** *ApJ*, 507:L49–L53, November 1998. 10, 64
- [75] J. M. LATTIMER. **Constraints on the Dense Matter Equation of State from Observations.** In S. KUBONO, W. AOKI, T. KAJINO, T. MOTOBAYASHI, & K. NOMOTO, editor, *Origin of Matter and Evolution of Galaxies*, 847 of *American Institute of Physics Conference Series*, pages 155–162, July 2006. 5
- [76] J. M. LATTIMER AND M. PRAKASH. **Neutron star observations: Prognosis for equation of state constraints.** *Phys. Rep.*, 442:109–165, April 2007. 6, 8
- [77] B. LINK. **Precession of Isolated Neutron Stars.** In M. BAILES, D. J. NICE, & S. E. THORSETT, editor, *Radio Pulsars*, 302 of *Astronomical Society of the Pacific Conference Series*, pages 241–+, 2003. 75
- [78] B. LINK. **Incompatibility of long-period neutron star precession with creeping neutron vortices.** *A&A*, 458:881–884, November 2006. 16, 90
- [79] B. LINK AND R. I. EPSTEIN. **Precession Interpretation of the Isolated Pulsar PSR B1828-11.** *ApJ*, 556:392–398, July 2001. 61, 90
- [80] K. LIU, Y. L. YUE, AND R. X. XU. **PSR B1828-11: a precession pulsar torqued by a quark planet?** *MNRAS*, 381:L1–L5, October 2007. 59
- [81] A. G. LYNE. **The magnetic fields of neutron stars.** In *Astronomy, physics and chemistry of H_3^+* , 358 of *Royal Society of London Philosophical Transactions Series A*, pages 831–840, February 2000. 4
- [82] W. W. MACY, JR. **Pulsar Magnetic Axis Alignment and Counteralignment.** *ApJ*, 190:153–164, May 1974. 4
- [83] V. M. MALOFEEV, O. I. MALOV, AND D. A. TEPLYKH. **Pulsed Radio Emission From Two XDINS.** In *IAU Joint Discussion*, 2 of *IAU Joint Discussion*, August 2006. 8
- [84] V. M. MALOFEEV, O. I. MALOV, D. A. TEPLYKH, S. V. LOGVINENKO, I. I. LITVINOV, AND S. B. POPOV. **Discovery of radio emission from X-ray pulsar XDINS 1RXS J214303.7 +065419+06.** *The Astronomer's Telegram*, 798:1–+, April 2006. 8
- [85] R. N. MANCHESTER, G. B. HOBBS, A. TEOH, AND M. HOBBS. **ATNF Pulsar Catalog (Manchester+, 2005).** *VizieR Online Data Catalog*, 7245:0–+, August 2005. 2
- [86] R. P. MIGNANI, C. MOTCH, F. HABERL, S. ZANE, R. TUROLLA, AND A. SCHWOPE. **VLT optical observations of the isolated neutron star RX J0420.0-5022.** *A&A*, 505:707–713, October 2009. 11
- [87] K. MORI AND W. C. G. HO. **Modelling mid-Z element atmospheres for strongly magnetized neutron stars.** *MNRAS*, 377:905–919, May 2007. 5, 10
- [88] C. MOTCH AND F. HABERL. **Constraints on optical emission from the isolated neutron star candidate RXJ0720.4-3125.** *A&A*, 333:L59–L62, May 1998. 10
- [89] C. MOTCH, A. M. PIRES, F. HABERL, A. SCHWOPE, AND V. E. ZAVLIN. **Proper motions of ROSAT discovered isolated neutron stars measured with Chandra: First X-ray measurement of the large proper motion of RX J1308.6+2127/RBS 1223.** In C. BASSA, Z. WANG, A. CUMMING, & V. M. KASPI, editor, *40 Years of Pulsars: Millisecond Pulsars, Magnetars and More*, 983 of *American Institute of Physics Conference Series*, pages 354–356, February 2008. 8, 9, 11
- [90] C. MOTCH, K. SEKIGUCHI, F. HABERL, V. E. ZAVLIN, A. SCHWOPE, AND M. W. PAKULL. **The proper motion of the isolated neutron star ι ASTROBJ ι RX J1605.3+3249/ ι ASTROBJ ι .** *A&A*, 429:257–265, January 2005. 11
- [91] C. MOTCH, V. E. ZAVLIN, AND F. HABERL. **The proper motion and energy distribution of the isolated neutron star RX J0720.4-3125.** *A&A*, 408:323–330, September 2003. 9, 64
- [92] R. W. NELSON, L. S. FINN, AND I. WASSERMAN. **Trompe L'Oeil 'binary' pulsars.** *ApJ*, 348:226–231, January 1990. 12, 57, 75, 76
- [93] J. NORONHA AND A. SEDRAKIAN. **Tkachenko modes as sources of quasiperiodic pulsar spin variations.** *Phys. Rev. D*, 77(2):023008–+, January 2008. 63
- [94] J. R. OPPENHEIMER AND G. M. VOLKOFF. **On Massive Neutron Cores.** *Physical Review*, 55:374–381, February 1939. 5
- [95] J. P. OSTRIKER AND J. E. GUNN. **On the Nature of Pulsars. I. Theory.** *ApJ*, 157:1395–+, September 1969. 3
- [96] F. PAERELS. **Pressure Broadening of Absorption Lines in Neutron Star Atmospheres and Prospects for Measuring Neutron Star Masses and Radii.** *ApJ*, 476:L47–+, February 1997. 63
- [97] C. PALOMBA. **Simulation of a population of isolated neutron stars evolving through the emission of gravitational waves.** *MNRAS*, 359:1150–1164, May 2005. 4
- [98] G. G. PAVLOV, Y. A. SHIBANOV, V. E. ZAVLIN, AND R. D. MEYER. **Neutron Star Atmospheres.** In M. A. ALPAR, U. KIZILOGLU, & J. VAN PARADJIS, editor, *The Lives of the Neutron Stars*, pages 71–+, 1995. 37
- [99] A. M. PIRES, C. MOTCH, R. TUROLLA, A. TREVES, AND S. B. POPOV. **The isolated neutron star candidate 2XMM J104608.7-594306.** *A&A*, 498:233–240, April 2009. 7
- [100] J. A. PONS AND U. GEPPERT. **Magnetic field dissipation in neutron star crusts: from magnetars to isolated neutron stars.** *A&A*, 470:303–315, July 2007. 4
- [101] J. A. PONS, J. A. MIRALLES, AND U. GEPPERT. **Magneto-thermal evolution of neutron stars.** *A&A*, 496:207–216, March 2009. 74, 89

REFERENCES

- [102] S. B. POPOV. **The Zoo of neutron stars.** *Physics of Particles and Nuclei*, **39**:1136–1142, December 2008. 2
- [103] S. B. POPOV. **Tkachenko waves, glitches and precession in neutron stars.** *Ap&SS*, **317**:175–179, October 2008. 61, 63
- [104] S. B. POPOV, M. COLPI, M. E. PROKHOROV, A. TREVES, AND R. TUROLLA. **Young isolated neutron stars from the Gould Belt.** *A&A*, **406**:111–117, July 2003. 7
- [105] B. POSSELT, R. NEUHÄUSER, AND F. HABERL. **Searching for substellar companions of young isolated neutron stars.** *A&A*, **496**:533–545, March 2009. 8, 64, 66
- [106] B. POSSELT, G. PAVLOV, AND M. HOHLE. **Is there a fallback disk around RX J0720.4-3125?** In *Spitzer Proposal ID #70045*, pages 70045–+, June 2010. 65, 67, 90
- [107] B. POSSELT, S. B. POPOV, F. HABERL, J. TRÜMPER, R. TUROLLA, AND R. NEUHÄUSER. **The Magnificent Seven in the dusty prairie.** *Ap&SS*, **308**:171–179, April 2007. 8, 11
- [108] B. POSSELT, K. SCHREYER, R. PERNA, M. W. SOMMER, B. KLEIN, AND P. SLANE. **Submillimetre observations of RXJ1856.5-3754.** *MNRAS*, **405**:1840–1844, July 2010. 65
- [109] J. POUTANEN AND A. M. BELOBORODOV. **Pulse profiles of millisecond pulsars and their Fourier amplitudes.** *MNRAS*, **373**:836–844, December 2006. 48, 49, 72, 73
- [110] S. M. RANSOM, S. S. EIKENBERRY, AND J. MIDDLEDITCH. **Fourier Techniques for Very Long Astrophysical Time-Series Analysis.** *AJ*, **124**:1788–1809, September 2002. 31, 32, 48, 49, 50, 55, 98
- [111] S. M. RANSOM, B. M. GAENSLER, AND P. O. SLANE. **A Deep Search for Pulsations from the Nearby Isolated Neutron Star RX J1856.5-3754.** *ApJ*, **570**:L75–L78, May 2002. 9
- [112] M. RUDERMAN. **Long Period Oscillations in Rotating Neutron Stars.** *Nature*, **225**:619–620, February 1970. 61, 63
- [113] R. E. RUTLEDGE, D. B. FOX, AND A. H. SHEVCHUK. **Discovery of an Isolated Compact Object at High Galactic Latitude.** *ApJ*, **672**:1137–1143, January 2008. 7
- [114] C. L. SARAZIN AND J. N. BAHCALL. **On the Zeeman splitting of X-ray lines by neutron-star magnetic fields.** *ApJ*, **216**:L67–L70, September 1977. 64
- [115] A. D. SCHWOPE, V. HAMBARYAN, F. HABERL, AND C. MOTCH. **The pulsed X-ray light curves of the isolated neutron star RBS1223.** *A&A*, **441**:597–604, October 2005. 11
- [116] A. D. SCHWOPE, V. HAMBARYAN, F. HABERL, AND C. MOTCH. **The complex X-ray spectrum of the isolated neutron star RBS1223.** *Ap&SS*, **308**:619–623, April 2007. 11
- [117] S. L. SHAPIRO AND S. A. TEUKOLSKY. *Black holes, white dwarfs, and neutron stars: The physics of compact objects.* 1983. 4, 5, 7
- [118] I. H. STAIRS. **Masses of radio pulsars.** *Journal of Physics G Nuclear Physics*, **32**:259–+, December 2006. 1, 4, 90
- [119] I. H. STAIRS. **Binary pulsars and tests of general relativity.** In S. A. KLONER, P. K. SEIDELMANN, & M. H. SOFFEL, editor, *IAU Symposium*, **261** of *IAU Symposium*, pages 218–227, January 2010. 1
- [120] L. STRÜDER, U. BRIEL, K. DENNERL, R. HARTMANN, E. KENDZIORRA, N. MEIDINGER, E. PFEFFERMANN, C. REPPIN, B. ASCHENBACH, W. BORNEMANN, H. BRÄUNINGER, W. BURKERT, M. ELENDER, M. FREYBERG, F. HABERL, G. HARTNER, F. HEUSCHMANN, H. HIPPMANN, E. KASTELIC, S. KEMMER, G. KETTENRING, W. KINK, N. KRAUSE, S. MÜLLER, A. OPPITZ, W. PIETSCH, M. POPP, P. PREDEHL, A. READ, K. H. STEPHAN, D. STÖTTER, J. TRÜMPER, P. HOLL, J. KEMMER, H. SOLTAU, R. STÖTTER, U. WEBER, U. WEICHERT, C. VON ZANTHIER, D. CARATHANASSIS, G. LUTZ, R. H. RICHTER, P. SOLC, H. BÖTTCHER, M. KUSTER, R. STAUBERT, A. ABBEY, A. HOLLAND, M. TURNER, M. BALASINI, G. F. BIGNAMI, N. LA PALOMBARA, G. VILLA, W. BUTTLER, F. GIANINI, R. LAINÉ, D. LUMB, AND P. DHEZ. **The European Photon Imaging Camera on XMM-Newton: The pn-CCD camera.** *A&A*, **365**:L18–L26, January 2001. 18, 24
- [121] N. TETZLAFF, R. NEUHÄUSER, AND M. M. HOHLE. **The origin of the Guitar pulsar.** *MNRAS*, **400**:L99–L102, November 2009. 4
- [122] N. TETZLAFF, R. NEUHÄUSER, M. M. HOHLE, AND G. MACIEJEWSKI. **Identifying birth places of young isolated neutron stars.** *MNRAS*, **402**:2369–2387, March 2010. 4, 8, 9, 11, 58
- [123] V. K. TKACHENKO. **Stability of Vortex Lattices.** *Soviet Journal of Experimental and Theoretical Physics*, **23**:1049–+, December 1966. 61
- [124] J. TRÜMPER. **The ROSAT mission.** *Adv. Space Res.*, **2**:241–249, 1982. 17
- [125] M. J. L. TURNER, A. ABBEY, M. ARNAUD, M. BALASINI, M. BARBERA, E. BELSOLE, P. J. BENNIE, J. P. BERNARD, G. F. BIGNAMI, M. BOER, U. BRIEL, I. BUTLER, C. CARA, C. CHABAUD, R. COLE, A. COLLURA, M. CONTE, A. CROS, M. DENBY, P. DHEZ, G. DI COCO, J. DOWSON, P. FERRANDO, S. GHIZZARDI, F. GIANOTTI, C. V. GOODALL, L. GRETTON, R. G. GRIFFITHS, O. HAINAUT, J. F. HOCHEDÉZ, A. D. HOLLAND, E. JOURDAIN, E. KENDZIORRA, A. LAGOSTINA, R. LAINÉ, N. LA PALOMBARA, M. LORTHOLARY, D. LUMB, P. MARTY, S. MOLENDI, C. PIGOT, E. POINDRON, K. A. POUNDS, J. N. REEVES, C. REPPIN, R. ROTHENFLUG, P. SALVETAT, J. L. SAUVAGEOT, D. SCHMITT, S. SEMBAY, A. D. T. SHORT, J. SPRAGG, J. STEPHEN, L. STRÜDER, A. TIENGO, M. TRIFOGLIO, J. TRÜMPER, S. VERCELLONE, L. VIGROUX, G. VILLA, M. J. WARD, S. WHITEHEAD, AND E. ZONCA. **The European Photon Imaging Camera on XMM-Newton: The MOS cameras: The MOS cameras.** *A&A*, **365**:L27–L35, January 2001. 18, 34, 39
- [126] R. TUROLLA, S. ZANE, AND J. J. DRAKE. **Bare Quark Stars or Naked Neutron Stars? The Case of RX J1856.5-3754.** *ApJ*, **603**:265–282, March 2004. 9
- [127] M. H. VAN KERKWIJK AND D. L. KAPLAN. **Timing the Nearby Isolated Neutron Star RX J1856.5-3754.** *ApJ*, **673**:L163–L166, February 2008. 2, 10, 11
- [128] M. H. VAN KERKWIJK, D. L. KAPLAN, M. DURANT, S. R. KULKARNI, AND F. PAERELS. **A Strong, Broad Absorption Feature in the X-Ray Spectrum of the Nearby Neutron Star RX J1605.3+3249.** *ApJ*, **608**:432–443, June 2004. 11
- [129] M. H. VAN KERKWIJK, D. L. KAPLAN, G. G. PAVLOV, AND K. MORI. **Spectral and Rotational Changes in the Isolated Neutron Star RX J0720.4-3125.** *ApJ*, **659**:L149–L152, April 2007. 10, 11, 12, 15, 30, 31, 33, 34, 36, 48, 49, 50, 59, 60, 62, 65, 67, 98
- [130] J. VINK. **RX J0720 evolution: precession, glitching, the last flutterings of a magnetar?** In *XMM-Newton Proposal ID #05545101*, pages 135–+, October 2007. 22
- [131] F. M. WALTER. **The Proper Motion, Parallax, and Origin of the Isolated Neutron Star RX J185635-3754.** *ApJ*, **549**:433–440, March 2001. 9
- [132] F. M. WALTER, T. EISENBEISS, J. M. LATTIMER, B. KIM, V. HAMBARYAN, AND R. NEUHAEUSER. **Revisiting the Parallax of the Isolated Neutron Star RX J185635-3754 Using HST/ACS Imaging.** *ArXiv e-prints*, August 2010. 9, 11
- [133] F. M. WALTER AND J. M. LATTIMER. **A Revised Parallax and Its Implications for RX J185635-3754.** *ApJ*, **576**:L145–L148, September 2002. 7, 9, 11
- [134] F. M. WALTER AND L. D. MATTHEWS. **The optical counterpart of the isolated neutron star RX J185635-3754.** *Nature*, **389**:358–360, September 1997. 7, 11

- [135] F. M. WALTER, S. J. WOLK, AND R. NEUHÄUSER. **Discovery of a nearby isolated neutron star.** *Nature*, **379**:233–235, January 1996. 7
- [136] J. C. L. WANG. **Evidence for Magnetic Field Decay in RX J0720.4-3125.** *ApJ*, **486**:L119+, September 1997. 9
- [137] N. WANG, R. N. MANCHESTER, R. T. PACE, M. BAILES, V. M. KASPI, B. W. STAPPERS, AND A. G. LYNE. **Glitches in southern pulsars.** *MNRAS*, **317**:843–860, October 2000. 15
- [138] Z. WANG, D. CHAKRABARTY, AND D. L. KAPLAN. **A debris disk around an isolated young neutron star.** *Nature*, **440**:772–775, April 2006. 63
- [139] K. WETTE, B. J. OWEN, B. ALLEN, M. ASHLEY, J. BETZWIESER, N. CHRISTENSEN, T. D. CREIGHTON, V. DERGACHEV, I. GHOLAMI, E. GOETZ, R. GUSTAFSON, D. HAMMER, D. I. JONES, B. KRISHNAN, M. LANDRY, B. MACHENSCHALK, D. E. MCCLELLAND, G. MENDELL, C. J. MESSENGER, M. A. PAPA, P. PATEL, M. PITKIN, H. J. PLETSCH, R. PRIX, K. RILES, L. SANCHO DE LA JORDANA, S. M. SCOTT, A. M. SINTES, M. TRIAS, J. T. WHELAN, AND G. WOAN. **Searching for gravitational waves from Cassiopeia A with LIGO.** *Classical and Quantum Gravity*, **25**(23):235011+, December 2008. 4
- [140] A. WOLSCZCAN AND D. A. FRAIL. **A planetary system around the millisecond pulsar PSR1257 + 12.** *Nature*, **355**:145–147, January 1992. 1, 65
- [141] F. WU, R. X. XU, AND J. GIL. **The braking indices in pulsar emission models.** *A&A*, **409**:641–645, October 2003. 4
- [142] R. X. XU. **A Thermal Featureless Spectrum: Evidence for Bare Strange Stars?** *ApJ*, **570**:L65–L68, May 2002. 9
- [143] R. X. XU AND G. J. QIAO. **Pulsar Braking Index: A Test of Emission Models?** *ApJ*, **561**:L85–L88, November 2001. 4
- [144] Y. YAO AND Q. D. WANG. **X-Ray Absorption Line Spectroscopy of the Galactic Hot Interstellar Medium.** *ApJ*, **624**:751–764, May 2005. 64
- [145] J. P. YUAN, R. N. MANCHESTER, N. WANG, X. ZHOU, Z. Y. LIU, AND Z. F. GAO. **A very large glitch in PSR B2334+61.** *ArXiv e-prints*, July 2010. 63
- [146] J. P. YUAN, N. WANG, R. N. MANCHESTER, AND Z. Y. LIU. **29 glitches detected at Urumqi Observatory.** *MNRAS*, **404**:289–304, May 2010. 15
- [147] L. ZAMPIERI, S. CAMPANA, R. TUROLLO, M. CHEREGATO, R. FALOMO, D. FUGAZZA, A. MORETTI, AND A. TREVES. **1RXS J214303.7+065419/RBS 1774: A new Isolated Neutron Star candidate.** *A&A*, **378**:L5–L9, October 2001. 7, 11
- [148] S. ZANE. **Neutron star surface emission: Beyond the dipole model.** *Ap&SS*, **308**:259–265, April 2007. 74, 89
- [149] S. ZANE, M. CROPPER, R. TUROLLO, L. ZAMPIERI, M. CHEREGATO, J. J. DRAKE, AND A. TREVES. **XMM-Newton Detection of Pulsations and a Spectral Feature in the X-Ray Emission of the Isolated Neutron Star 1RXS J214303.7+065419/RBS 1774.** *ApJ*, **627**:397–403, July 2005. 11
- [150] S. ZANE, A. DE LUCA, R. P. MIGNANI, AND R. TUROLLO. **The proper motion of the isolated neutron star RX J1605.3+3249.** *A&A*, **457**:619–622, October 2006. 11
- [151] S. ZANE, F. HABERL, M. CROPPER, V. E. ZAVLIN, D. LUMB, S. SEMBAY, AND C. MOTCH. **Timing analysis of the isolated neutron star RX J0720.4-3125.** *MNRAS*, **334**:345–354, August 2002. 10, 32, 36, 52
- [152] S. ZANE, F. HABERL, G. L. ISRAEL, A. PELLIZZONI, M. BURGAY, R. P. MIGNANI, R. TUROLLO, A. POSSENTI, P. ESPOSITO, D. CHAMPION, R. P. EATOUGH, E. BARR, AND M. KRAMER. **Discovery of 59ms Pulsations from 1RXS J141256.0+792204 (Calvera).** *ArXiv e-prints*, September 2010. 7
- [153] S. ZANE, R. P. MIGNANI, R. TUROLLO, A. TREVES, F. HABERL, C. MOTCH, L. ZAMPIERI, AND M. CROPPER. **An Optical Counterpart Candidate for the Isolated Neutron Star RBS 1774.** *ApJ*, **682**:487–491, July 2008. 11, 65
- [154] S. ZANE AND R. TUROLLO. **Unveiling the thermal and magnetic map of neutron star surfaces through their X-ray emission: method and light-curve analysis.** *MNRAS*, **366**:727–738, March 2006. 71
- [155] S. ZANE, R. TUROLLO, AND J. J. DRAKE. **Is RX J1856.5-3754 a naked neutron star?** *Advances in Space Research*, **33**:531–536, 2004. 65
- [156] S. ZANE, R. TUROLLO, AND D. PAGE, editors. *Isolated Neutron Stars: from the Surface to the Interior*, 2007. 65
- [157] V. E. ZAVLIN, G. G. PAVLOV, AND Y. A. SHIBANOV. **Model neutron star atmospheres with low magnetic fields. I. Atmospheres in radiative equilibrium.** *A&A*, **315**:141–152, November 1996. 37

REFERENCES

Appendix A

Time of arrivals (TOAs) of the final timing solution and individual Periods

A. TIME OF ARRIVALS (TOAs) OF THE FINAL TIMING SOLUTION AND INDIVIDUAL PERIODS

Table A.1: The individual periods of RX J0720.4–3125 for the soft (120 – 400 eV) and hard (400 – 1000 eV) band (except for ROSAT and Chandra HRC, i.e. the periods derived from all counts are listed). The tags mark the merged Chandra observations (see also table 2.3). Note that the periods of the ROSAT data with a low count number (see table 2.1) deviate significantly from those listed in [19] and are highly uncertain. The TOAs of the soft band (for the “all data” solution of the soft band, see table 4.4) and of the hard band (for the “all data” solution of the hard band, see table 4.4) follow the definition in [63; 129]. The errors of the periods [110] and the TOAs (derived from the fitted light curves) are given in parenthesis and denote 1σ confidence level.

Obs. Id.	Instrument/setup	period (120 – 400 eV) [s]	period (400 – 1000 eV) [s]	TOA (120 – 400 eV) [days]	TOA (400 – 1000 eV) [days]
rp300338n00	PSPC		8.39120(44)	49, 257.2547153(16)	49, 257.2547298(21)
rh300508n00	HRI		8.3852(63)	50, 198.6873383(25)	50, 198.6873509(35)
rh180100n00	HRI		8.3443(11)	50, 210.5562791(18)	50, 210.5562812(17)
rh300508n01	HRI		8.4902(98)	50, 353.9975633(27)	50, 353.9975702(20)
rh400884n00	HRI		8.391130(50)	50, 391.3004644(14)	50, 391.3004729(18)
h400944n00	HRI		8.3921(10)	50, 925.6878393(11)	50, 925.6878472(21)
368 ¹	HRC-S/LETG		8.39063(49)	51, 577.0395641(21)	51, 577.0395693(16)
745 ¹	HRC-S/LETG				
369 ¹	HRC-S/LETG				
0078 S3	EPIC-pn/FF thin	8.391113(18)	8.391085(35)	51, 677.44324000(30)	51, 677.44323979(69)
S1	EPIC-MOS1/FF thin	8.391090(45)	8.391090(55)	51, 677.47179274(83)	51, 677.47179286(78)
S2	EPIC-MOS2/SW thin	8.391113(23)	8.391033(53)	51, 677.47179234(54)	51, 677.4717923(13)
0175 S3	EPIC-pn/FF med	8.391268(58)	8.39124(12)	51, 869.95710586(60)	51, 869.95710803(84)
S7	EPIC-MOS1/LW med	8.39122(22)	8.39107(32)	51, 869.9949836(13)	51, 869.9949874(27)
2774 ²	ACIS-CC	8.391093(13)	8.391133(13)	52, 248.6767290(15)	52, 248.67672069(69)
2773 ²	ACIS-CC				

Table A.1: – Continued. –

Obs. Id.	Instrument/setup	period (120 – 400 eV) [s]	period (400 – 1000 eV) [s]	TOA (120 – 400 eV) [days]	TOA (400 – 1000 eV) [days]
2771 ²	ACIS-CC				
2772 ²	ACIS-CC				
0533 S3	EPIC-pn/FF thin	8.391143(43)	8.391098(73)	52, 584.92605120(69)	52, 584.9260530(10)
S1	EPIC-MOS1/FF thin	8.39136(12)	8.39088(16)	52, 584.91993465(11)	52, 584.9200294(15)
S2	EPIC-MOS2/FF thin	8.39122(12)	8.39104(20)	52, 584.91993465(95)	52, 584.9199325(16)
0534 S3	EPIC-pn/FF thin	8.391225(40)	8.391317(63)	52, 587.00129529(39)	52, 587.00129506(97)
S1	EPIC-MOS1/FF thin	8.39119(11)	8.39116(18)	52, 586.9952779(18)	52, 586.9952766(29)
S2	EPIC-MOS2/FF thin	8.39137(13)	8.39137(23)	52, 586.99527264(93)	52, 586.9952735(14)
0622 U2	EPIC-pn/SW thick	8.391133(18)	8.391138(23)	52, 761.99514720(82)	52, 761.99514812(64)
S5	EPIC-MOS1/FF med	8.39130(16)	8.39100(20)	52, 762.2413478(13)	52, 762.2413532(20)
S3	EPIC-MOS1/FF thin	8.39101(13)	8.39100(17)	52, 761.8668566(19)	52, 761.8668516(28)
S6	EPIC-MOS2/FF med	8.39100(15)	8.39126(15)	52, 762.2413439(17)	52, 762.24144068(14)
S4	EPIC-MOS2/FF thin	8.390950(95)	8.39118(21)	52, 761.8669520(11)	52, 761.8669491(20)
0711 S8	EPIC-pn/SW med	8.391082(48)	8.391188(82)	52, 940.11635982(97)	52, 940.11627407(69)
S3	EPIC-MOS1/FF thin	8.39125(31)	8.39077(52)	52, 939.99012307(84)	52, 939.9900211(20)
S5	EPIC-MOS1/LW thin	8.39087(24)	8.39059(41)	52, 940.1679353(12)	52, 940.1679433(29)
S4	EPIC-MOS2/FF thin	8.39169(32)	8.39051(49)	52, 939.9900070(17)	52, 939.9900222(24)
S6	EPIC-MOS2/LW thin	8.39091(22)	8.39147(26)	52, 940.1679318(13)	52, 940.1679407(14)
4666 ³	ACIS-CC	8.3911142(23)	8.3911216(28)	53, 016.68131016(91)	53, 016.6813159(12)
4667 ³	ACIS-CC				

A. TIME OF ARRIVALS (TOAs) OF THE FINAL TIMING SOLUTION AND INDIVIDUAL PERIODS

Table A.1: – Continued. –

Obs. Id.	Instrument/setup	period (120 – 400 eV) [s]	period (400 – 1000 eV) [s]	TOA (120 – 400 eV) [days]	TOA (400 – 1000 eV) [days]
4668 ³	ACIS-CC				
4669 ³	ACIS-CC				
5305 ⁴	HRC-S/LETG		8.39109(25)	53, 062.4157092(15)	53, 062.4157091(15)
0815 S1	EPIC-pn/FF thin	8.391105(35)	8.391143(58)	53, 147.68119387(43)	53, 147.6812041(15)
S2	EPIC-MOS1/FF thin	8.391108(68)	8.39111(15)	53, 147.6883801(11)	53, 147.6883883(31)
S3	EPIC-MOS2/FF thin	8.391150(60)	8.39120(13)	53, 147.68838022(93)	53, 147.6883911(21)
4670 ⁵	ACIS-CC	8.3911146(15)	8.3911165(16)	53, 230.5756209(11)	53, 230.5756243(19)
4671 ⁵	ACIS-CC				
4672 ⁵	ACIS-CC				
4673 ⁵	ACIS-CC				
5581 ⁶	HRC-S/LETG		8.391010(95)	53, 393.6674769(19)	53, 393.6674775(23)
0986 S3	EPIC-pn/FF thin	8.391138(23)	8.391140(30)	53, 488.67561302(44)	53, 488.67561797(84)
S1	EPIC-MOS1/SW thin	8.391095(45)	8.391008(48)	53, 488.6695937(14)	53, 488.6695969(13)
S2	EPIC-MOS2/SW thin	8.391183(38)	8.391018(53)	53, 488.6696892(13)	53, 488.6696931(14)
5582 ⁷	HRC-S/LETG		8.391138(63)	53, 522.9398395(35)	53, 522.9398385(29)
6364 ⁸	HRC-S/LETG		8.39129(25)	53, 610.0881154(30)	53, 610.0881131(20)
1060 S3	EPIC-pn/FF thin	8.391120(20)	8.391082(33)	53, 636.30015746(23)	53, 636.3001616(10)
S1	EPIC-MOS1/SW thin	8.391095(40)	8.391130(50)	53, 636.29413571(70)	53, 636.2941416(13)
S2	EPIC-MOS2/SW thin	8.391103(38)	8.391163(58)	53, 636.29413754(96)	53, 636.29413962(83)
6369 ⁹	HRC-S/LETG		8.39110(11)	53, 652.2601916(17)	53, 652.2601885(15)

Table A.1: – Continued. –

Obs. Id.	Instrument/setup	period (120 – 400 eV) [s]	period (400 – 1000 eV) [s]	TOA (120 – 400 eV) [days]	TOA (400 – 1000 eV) [days]
7177 ⁹	HRC-S/LETG				
1086 S3	EPIC-pn/FF thin	8.391125(25)	8.391072(38)	53, 687.17180535(53)	53, 687.17180817(92)
S1	EPIC-MOS1/SW thin	8.391003(63)	8.391085(80)	53, 687.1657835(12)	53, 687.16588680(52)
S2	EPIC-MOS2/SW thin	8.391200(55)	8.390998(78)	53, 687.1658825(10)	53, 687.1658857(12)
7243 ¹⁰	HRC-S/LETG		8.391115(10)	53, 720.0243035(13)	53, 720.0243020(12)
7244 ¹⁰	HRC-S/LETG				
7245 ¹⁰	HRC-S/LETG				
5584 ¹⁰	HRC-S/LETG				
7251	HRC-S/LETG		8.39212(88)		
1181 S1	EPIC-pn/FF thin	8.391090(70)	8.39120(11)	53, 775.3509131(17)	53, 775.35091144(12)
S2	EPIC-MOS1/SW thin	8.39137(17)	8.39101(20)	53, 877.32857154(71)	53, 877.3285752(11)
S3	EPIC-MOS2/SW thin	8.39131(13)	8.39116(18)	53, 877.3225489(15)	53, 877.32255272(65)
1265 S1	EPIC-pn/FF thin	8.391075(65)	8.39104(11)	53, 877.3225491(11)	53, 877.3225524(16)
S2	EPIC-MOS1/FF thin	8.39117(16)	8.39074(17)	54, 044.60537610(44)	54, 044.6053791(11)
S3	EPIC-MOS2/FF thin	8.39099(13)	8.39096(19)	54, 044.5990605(12)	54, 044.5990664(13)
1356 S1	EPIC-pn/FF thin	8.391150(65)	8.391113(98)	54, 044.59906220(62)	54, 044.5990665(18)
S2	EPIC-MOS1/FF thin	8.39107(21)	8.39066(27)	54, 225.84098865(82)	54, 225.84099190(98)
S3	EPIC-MOS2/FF thin	8.39103(23)	8.39096(22)	54, 225.8345794(18)	54, 225.83457862(99)
1454 S1	EPIC-pn/FF thin	8.391130(50)	8.391085(85)	54, 225.8346806(13)	54, 225.8346782(22)
S2	EPIC-MOS1/FF thin	8.39090(16)	8.39109(17)	54, 421.36989356(53)	54, 421.36989479(60)
				54, 421.3635797(17)	54, 421.3635840(15)

A. TIME OF ARRIVALS (TOAs) OF THE FINAL TIMING SOLUTION AND INDIVIDUAL PERIODS

Table A.1: – Continued. –

Obs. Id.	Instrument/setup	period (120 – 400 eV) [s]	period (400 – 1000 eV) [s]	TOA (120 – 400 eV) [days]	TOA (400 – 1000 eV) [days]
S3	EPIC-MOS2/FF thin	8.39131(22)	8.39127(22)	54, 421.3635875(20)	54, 421.3635849(18)
10861 ¹¹	HRC-S/LETG		8.39129(20)	54, 863.7916775(17)	54, 863.7916751(12)
10700 ¹¹	HRC-S/LETG				
1700 S3	EPIC-pn/FF thin	8.39108(99)	8.3912(12)	54, 911.7856154(16)	54, 911.78046975(81)
U2	EPIC-MOS1/FF thin	8.39097(26)	8.39136(29)	54, 911.7440458(30)	54, 911.7440479(17)
U2	EPIC-MOS2/FF thin	8.39103(25)	8.39118(35)	54, 911.7440524(13)	54, 911.7440483(15)
10701 ¹²	HRC-S/LETG		8.39119(20)	55, 085.6684206(14)	55, 085.6684187(15)
1792 S3	EPIC-pn/FF thin	8.39102(12)	8.39101(15)	55, 096.30446151(69)	55, 096.3044632(11)
S1	EPIC-MOS1/SW thin	8.39097(20)	8.39120(20)	55, 096.29666932(13)	55, 096.29666943(13)
S2	EPIC-MOS2/SW thin	8.39104(15)	8.39102(24)	55, 096.2967896(14)	55, 096.2967885(11)

Appendix B

Publications during PhD

B.1 Scientific papers

- *A catalogue of young runaway stars within 3 kpc from Hipparcos;*
Tetzlaff, N.; Neuhäuser, R.; **Hohle, M. M.**; MNRAS; 2010; in press
- *Updated phase coherent timing solution of the isolated neutron star RX J0720.4–3125 using recent XMM-Newton and Chandra observations;*
Hohle, M. M.; Haberl, F.; Vink, J.; Turolla, R.; Zane, S.; de Vries, C. P.; Méndez, M.; A&A; 2010; in press
- *O, B-type & red supergiant masses and luminosities;*
Hohle, M. M.; Neuhäuser, R.; Schutz, B. F.; Cat; 2010
- *Kinematics of young associations/clusters;*
Tetzlaff, N.; Neuhäuser, R.; **Hohle, M. M.**; Maciejewski, G.; Cat; 2010
- *Identifying birth places of young isolated neutron stars;*
Tetzlaff, N.; Neuhäuser, R.; **Hohle, M. M.**; Maciejewski, G.; MNRAS; 2010; 402, 2369
- *Masses and luminosities of O- and B-type stars and red supergiants;*
Hohle, M. M.; Neuhäuser, R.; Schutz, B. F.; AN; 2010; 331, 349
- *New photometry and astrometry of the isolated neutron star RX J0720.4–3125 using recent VLT/FORS observations;*
Eisenbeiss, T.; Ginski, C.; **Hohle, M. M.**; Hambaryan, V. V.; Neuhäuser, R.; Schmidt, T. O. B; AN; 2010; 331, 243
- *The origin of the Guitar pulsar;*
Tetzlaff, N.; Neuhäuser, R.; **Hohle, M. M.**; MNRAS; 2009; 400, 99

B. PUBLICATIONS DURING PHD

- *Photometric study of the OB star clusters NGC 1502 and NGC 2169 and mass estimation of their members at the University Observatory Jena;*
Hohle, M. M.; Eisenbeiss, T.; Mugrauer, M.; Freistetter, F.; Moualla, M.; Neuhäuser, R.; Raetz, St.; Schmidt, T. O. B.; Tetzlaff, N.; Vaňko, M.; AN; 2009; 330, 511
- *Photometric analysis of the eclipsing binary 2MASS 19090585+4911585;*
Raetz, St.; Vaňko, M.; Mugrauer, M.; Schmidt, T. O. B.; Roell, T.; Eisenbeiss, T.; **Hohle, M. M.**; Koeltzsch, A.; Ginski, Ch.; Marka, C.; and 4 coauthors; AN; 2009; 330, 504
- *Photometric monitoring of the young star Par 1724 in Orion;*
Neuhäuser, R.; Koeltzsch, A.; Raetz, St.; Schmidt, T. O. B.; Mugrauer, M.; Young, N.; Bertoldi, F.; Roell, T.; Eisenbeiss, T.; **Hohle, M. M.**; and 5 coauthors; AN; 2009; 330, 493
- *Variability of young stars: Determination of rotational periods of weak-line T Tauri stars in the Cepheus-Cassiopeia star-forming region;*
Koeltzsch, A.; Mugrauer, M.; Raetz, St.; Schmidt, T. O. B.; Roell, T.; Eisenbeiss, T.; **Hohle, M. M.**; Vaňko, M.; Ginski, Ch.; Marka, C.; and 4 coauthors; AN; 2009; 330, 482
- *Planetary transit observations at the University Observatory Jena: XO-1b and TrES-1;*
Raetz, St.; Mugrauer, M.; Schmidt, T. O. B.; Roell, T.; Eisenbeiss, T.; **Hohle, M. M.**; Tetzlaff, N.; Vaňko, M.; Seifahrt, A.; Broeg, Ch.; and 2 coauthors; AN; 2009; 330, 475
- *Planetary transit observations at the University Observatory Jena: TrES-2;*
Raetz, St.; Mugrauer, M.; Schmidt, T. O. B.; Roell, T.; Eisenbeiss, T.; **Hohle, M. M.**; Koeltzsch, A.; Vaňko, M.; Ginski, Ch.; Marka, C.; and 7 coauthors; AN; 2009; 330, 459
- *New brown dwarf candidates in the Pleiades;*
Eisenbeiss, T.; Moualla, M.; Mugrauer, M.; Schmidt, T. O. B.; Raetz, St.; Neuhäuser, R.; Ginski, Ch.; **Hohle, M. M.**; Koeltzsch, A.; Marka, C.; and 4 coauthors; AN; 2009; 330, 439
- *Follow-up observations of Comet 17P/Holmes after its extreme outburst in brightness end of October 2007;*

Mugrauer, M.; **Hohle, M. M.**; Ginski, C.; Vanko, M.; Freistetter, F.; AN; 2009; 330, 425

- *Spectral and temporal variations of the isolated neutron star RX J0720.4–3125: new XMM-Newton observations;*
Hohle, M. M.; Haberl, F.; Vink, J.; Turolla, R.; Hambaryan, V.; Zane, S.; de Vries, C. P.; Méndez, M.; A&A; 2009; 498, 811
- *XMM-Newton RGS spectrum of RX J0720.4–3125: an absorption feature at 0.57 keV;*
Hambaryan, V.; Neuhäuser, R.; Haberl, F.; **Hohle, M. M.**; Schwobe, A. D.; A&A; 2009; 497, 9
- *Mass Ejection by Strange Star Mergers and Observational Implications;*
Bauswein, A.; Janka, H. -Th.; Oechslin, R.; Pagliara, G.; Sagert, I.; Schaffner-Bielich, J.; **Hohle, M. M.**; Neuhäuser, R.; Phys. Rev. Lett.; 2009; 103, 011101

B.2 Accepted proposals for observations listed in the ADS

- *Is there a fallback disk around RX J0720.4–3125?;*
Posselt, Bettina; Pavlov, George; **Hohle, Markus**; Spitzer prop.; 2010; 70045
- *RX J0720.4–3125 - a free precessing X-ray pulsar?;*
Hohle, M. M.; Haberl, F.; Vink, J.; Turolla, R.; Zane, S.; de Vries, C. P.; Méndez, M.; XMM-Newton prop; 2009; 28
- *RX J0720 evolution: precession, glitching, or the last flutterings of a magnetar;*
Hohle, M. M.; Haberl, F.; Vink, J.; Turolla, R.; Zane, S.; de Vries, C. P.; Méndez, M.; XMM-Newton prop; 2008; 26

B.3 Conference contributions and proceedings listed in the ADS

- *Variable spectrum of the X-Ray pulsar RX J0720.4–3125;*
Hohle, M.; Haberl, F.; 2009; hrxs.confE..21H

B. PUBLICATIONS DURING PHD

- *XMM-Newton RGS spectrum of RX J0720.4–3125: Absorption feature at 0.57 keV;* Hambaryan, V.; Neuhäuser, R.; Haberl, F.; **Hohle, M. M.**; Schwobe, A. D.; 2009; hrxs.confE..20H
- *RX J0720.4–3125 - a precessing X-ray pulsar?;* **Hohle, M.**; Haberl, F.; 2009; epsc.conf....4H
- *Transit observation at the observatory in Grossschwabhausen: XO–1b and TrES–1;* Vaňko, M.; Raetz, S.; Mugrauer, M.; Schmidt, T. O. B.; Roell, T.; Eisenbeiss, T.; **Hohle, M.**; Seifahrt, A.; Koeltzsch, A.; Broeg, C.; and 2 coauthors; 2009; IAUS..253..440V
- *Observations of the transiting planet TrES-2 with the AIU Jena telescope in Grossschwabhausen;* Raetz, S.; Mugrauer, M.; Schmidt, T. O. B.; Roell, T.; Eisenbeiss, T.; **Hohle, M.**; Seifahrt, A.; Koeltzsch, A.; Vaňko, M.; Broeg, Ch.; and 2 coauthors; 2009; IAUS..253..436R
- *Using radioactivities to improve the search for nearby radio-quiet neutron stars;* **Hohle, Markus M.**; Neuhäuser, Ralph; Tetzlaff, Nina; NewAR; 2008; 52, 405
- *New luminosities for O and B stars;* **Hohle, Markus M.**; Neuhäuser, Ralph; AN; 2007; 328, 713
- *First planetary transit observations with the AIU Jena telescope in Grossschwabhausen;* Raetz, Stefanie; Mugrauer, Markus; Schmidt, Tobias; Roell, Tristan; Eisenbeiss, Thomas; **Hohle, Markus**; Seifahrt, Andreas; Koeltzsch, Alexandra; Vaňko, Martin; Neuhäuser, Ralph; AN; 2007; 328, 710

Appendix C

Talks

C.1 Scientific talks

- Annual Meeting and General Assembly of the Astronomische Gesellschaft, Bonn, Germany, 16.09.2010
“RX J0720 – an X-ray pulsar in dusty environment?”
- Semi-annual meeting of the SFB/TR-7 Gravitational Wave Astronomy, Garching, Germany, 25.02.2010
“Population synthesis of massive stars, project C7 – Previous and planned work for C7 and planned work for C8 (new project)”
- Workshop on dense QCD phases in Heavy Ion Collisions and Supernovae, Prerow, Germany, 12.10.2009
“RX J0720.4 -31.25: a precessing X-ray pulsar? Spectral and temporal variations/ phase coherent timing” (invited)
- EuroPlanet Conference, Potsdam, Germany, 18.9.2009
“RX J0720.4–3125 – a precessing neutron star? (invited)”
- International Summer School on Nuclear Theory and Astrophysical Applications, Dubna, Russia, July 2008
“Spectral behaviour of the M7 like neutron star RX J0720.4-3125”
- DPG Frühjahrstagung in Freiburg/Breisg., Germany, 05.03.2008
“Neutron star population synthesis – predictions for GW detection”
- Semi-annual meeting of the SFB/TR-7 Gravitational Wave Astronomy, Potsdam/Golm, Germany, 26.02.2008
“Neutron star population synthesis – predictions for GW detection (?)”

- International Workshop of Astronomy with Radioactivities at Ringberg Castle of the Max-Planck-Gesellschaft in Kreuth, Germany, 7–10 January 2008
“Using radioactivities to improve the search for nearby radio-quiet neutron stars”

C.2 Public talks

- Vortrag für eine Besuchergruppe (talk for visitors), Jena, Germany, 19.09.2010
“Eine kurze Reise durch unser Sonnensystem” (A brief voyage through our Solar system)
- Lange Nacht der Wissenschaften (long night of science), Jena, Germany, 13.11.2009
“Neutronensterne – unheimliche Sterne” (Neutron stars – spooky stars)
- Einsteintag (Einstein day, workshop), Jena, Germany, 16.09.2009
“Koordinatensysteme in der Astronomie, Bewegungen am Himmel” (coordinate systems in astronomy and motions on the sky)
- Lehrerfortbildung (teachers workshop), Jena, Germany, 26.06.2009
“Neutronensterne, Quarksterne und Schwarze Löcher” (neutron stars, quark stars and black holes)
- Vortrag für Kinder der NAJU (talk for children of the German Society for the Protection of Nature), Jena, Germany, 06.12.2008
“Eine kurze Reise durch unser Sonnensystem” (A brief voyage through our Solar system)
- Vortrag für eine Slowakische Schulklasse (talk for a slowakian school class), Jena, Germany, 08.09.2008
“Übersicht über unser Institut” (Overview of our institute)
- Tag der offenen Tür (open day), Jena, Germany, 18.01.2008
“Unheimliche Sterne – Neutronensterne und Schwarze Löcher” (spooky stars – neutron stars and black holes)

Appendix D

Teaching and supervising

- contributed to the supervising of the current diploma thesis “Populationsynthese von massenreichen Sternen innerhalb 5 kpc” (Population synthesis of massive stars within 5 kpc) of János Schmidt, Jena, Germany, 2010
- contributed to the supervising of the diploma thesis “Kinematische Untersuchungen zu jungen isolierten Neutronensternen: Die Suche nach den Orten potentieller Supernovae.” (Kinematic investigations of young isolated neutron stars: The search for likely sites of supernovae), by Nina Tetzlaff, Jena, Germany, 2008/2009
- supervising the practical basic courses of the faculty of physics, Jena, Germany, 01.10.2007–31.12.2007
- supervising the practical courses for biophysics of the faculty of biology, Jena, Germany, 01.03.2007–31.07.2007
- supervising the practical courses for biophysics of the faculty of biology, Jena, Germany, 01.11.2006–31.12.2006
- student assistant of the faculty of physics and astronomy, Jena, Germany, 16.10.2006–03.02.2007
- supervising the practical basic courses of the faculty of physics, Jena, Germany, 15.05.2006–21.07.2006
- supervising the practical courses for biophysics of the faculty of biology, Jena, Germany, 01.03.2006–30.04.2006
- student assistant of the faculty of physics and astronomy, Jena, Germany, 07.11.2005–21.12.2006

D. TEACHING AND SUPERVISING

- student assistant of the faculty of physics and astronomy, Jena, Germany,
18.04.2005–17.07.2005

Appendix E

Curriculum vitae

Hohle, Markus Matthias

12.11.1982	birth, Pöbneck/Thuringia, Germany
1989–1993	primary school at Alfred Brehm Grundschule in Renthendorf/Thuringia, Germany
1993–2001	high school at Johann Heinrich Pestalozzi Gymnasium Stadtroda/Thuringia, Germany
2001	Abitur
2001–2002	German Airforce in Bayreuth and Fürstenfeldbruck/Bavaria, Germany
Oct 2002–2007	physics studies at Friedrich Schiller Universität Jena/Thuringia, Germany
Aug 2007	diploma in physics and astrophysics “Populationssynthese zur Abschätzung der Supernovaratte des Gould Belts: Suche nach jungen Neutronensternen” (Population synthesis to estimate the supernova rate of the Gould Belt: Search for young neutron stars)

E. CURRICULUM VITAE

Aug 2007–Dec 2007 working for SFB/TR-7
Gravitational Wave Astronomy, project C7
at Friedrich Schiller Universität Jena/Thuringia, Germany

2008–2010 PhD thesis in astrophysics and general relativity,
“The spectral and temporal variability of the
isolated X-ray pulsar RX J0720.4-3125”,
at the Max-Planck-Institut für extraterrestrische Physik
Garching/Bavaria, Germany
and Friedrich Schiller Universität Jena/Thuringia, Germany

Jena,

signature

Declaration

I herewith declare that I have produced this paper without the prohibited assistance of third parties and without making use of aids other than those specified; notions taken over directly or indirectly from other sources have been identified as such. This paper has not previously been presented in identical or similar form to any other German or foreign examination board.

The thesis work was conducted from January 1st 2008 to December 31st 2010 under the supervision of Frank Haberl at the Max-Planck-Institut für extraterrestrische Physik.

Jena,

Ich erkläre hiermit ehrenwörtlich, dass ich die vorliegende Arbeit selbständig, ohne unzulässige Hilfe Dritter und ohne Benutzung anderer als der angegebenen Hilfsmittel und Literatur angefertigt habe. Die aus anderen Quellen direkt oder indirekt bernommenen Daten und Konzepte sind unter Angabe der Quelle gekennzeichnet.

Bei der Auswahl und Auswertung folgenden Materials haben mir die nachstehend aufgeführten Personen in der jeweils beschriebenen Weise unentgeltlich geholfen:

- 1. Frank Haberl hat mir seine Programme zum analysieren der XMM-Newton EPIC-pn Daten zur Verfügung gestellt
- 2. Theodor Pribulla hat die Phasenresiduen mit der Orbitlösung mit Hilfe seines Programms gefittet.

Weitere Personen waren an der inhaltlich-materiellen Erstellung der vorliegenden Arbeit nicht beteiligt. Insbesondere habe ich hierfür nicht die entgeltliche Hilfe von Vermittlungs- bzw. Beratungsdiensten (Promotionsberater oder andere Personen) in Anspruch genommen. Niemand hat von mir unmittelbar oder mittelbar geldwerte Leistungen für Arbeiten erhalten, die im Zusammenhang mit dem Inhalt der vorgelegten Dissertation stehen.

Die Arbeit wurde bisher weder im In- noch im Ausland in gleicher oder ähnlicher Form einer anderen Prüfungsbehörde vorgelegt.

Die geltende Promotionsordnung der Physikalisch- Astronomischen Fakultät ist mir bekannt.

Ich versichere ehrenwörtlich, dass ich nach bestem Wissen die reine Wahrheit gesagt und nichts verschwiegen habe.

Ort, Datum

Unterschrift d. Verfassers